

University of Windsor

Scholarship at UWindor

Electronic Theses and Dissertations

Theses, Dissertations, and Major Papers

2005

Load/displacement and energy absorption performances and improvements of structural members under tensile and compressive loading conditions.

Qingwu Cheng
University of Windsor

Follow this and additional works at: <https://scholar.uwindsor.ca/etd>

Recommended Citation

Cheng, Qingwu, "Load/displacement and energy absorption performances and improvements of structural members under tensile and compressive loading conditions." (2005). *Electronic Theses and Dissertations*. 2630.

<https://scholar.uwindsor.ca/etd/2630>

This online database contains the full-text of PhD dissertations and Masters' theses of University of Windsor students from 1954 forward. These documents are made available for personal study and research purposes only, in accordance with the Canadian Copyright Act and the Creative Commons license—CC BY-NC-ND (Attribution, Non-Commercial, No Derivative Works). Under this license, works must always be attributed to the copyright holder (original author), cannot be used for any commercial purposes, and may not be altered. Any other use would require the permission of the copyright holder. Students may inquire about withdrawing their dissertation and/or thesis from this database. For additional inquiries, please contact the repository administrator via email (scholarship@uwindsor.ca) or by telephone at 519-253-3000ext. 3208.

LOAD/DISPLACEMENT AND ENERGY ABSORPTION
PERFORMANCES AND IMPROVEMENTS OF STRUCTURAL
MEMBERS UNDER TENSILE AND COMPRESSIVE LOADING
CONDITIONS

by

Qingwu Cheng

A Thesis

Submitted to the Faculty of Graduate Studies and Research
through Mechanical Engineering
in Partial Fulfillment of the Requirements for
the Degree of Master of Applied Science at the
University of Windsor

Windsor, Ontario, Canada

2005

© 2005 Qingwu Cheng



Library and
Archives Canada

Bibliothèque et
Archives Canada

Published Heritage
Branch

Direction du
Patrimoine de l'édition

395 Wellington Street
Ottawa ON K1A 0N4
Canada

395, rue Wellington
Ottawa ON K1A 0N4
Canada

Your file *Votre référence*

ISBN: 0-494-09730-2

Our file *Notre référence*

ISBN: 0-494-09730-2

NOTICE:

The author has granted a non-exclusive license allowing Library and Archives Canada to reproduce, publish, archive, preserve, conserve, communicate to the public by telecommunication or on the Internet, loan, distribute and sell theses worldwide, for commercial or non-commercial purposes, in microform, paper, electronic and/or any other formats.

The author retains copyright ownership and moral rights in this thesis. Neither the thesis nor substantial extracts from it may be printed or otherwise reproduced without the author's permission.

AVIS:

L'auteur a accordé une licence non exclusive permettant à la Bibliothèque et Archives Canada de reproduire, publier, archiver, sauvegarder, conserver, transmettre au public par télécommunication ou par l'Internet, prêter, distribuer et vendre des thèses partout dans le monde, à des fins commerciales ou autres, sur support microforme, papier, électronique et/ou autres formats.

L'auteur conserve la propriété du droit d'auteur et des droits moraux qui protègent cette thèse. Ni la thèse ni des extraits substantiels de celle-ci ne doivent être imprimés ou autrement reproduits sans son autorisation.

In compliance with the Canadian Privacy Act some supporting forms may have been removed from this thesis.

Conformément à la loi canadienne sur la protection de la vie privée, quelques formulaires secondaires ont été enlevés de cette thèse.

While these forms may be included in the document page count, their removal does not represent any loss of content from the thesis.

Bien que ces formulaires aient inclus dans la pagination, il n'y aura aucun contenu manquant.


Canada

ABSTRACT

The research programs detailed in this thesis focus on the load/displacement and energy absorption performances and improvements of structural members under tensile and compressive loading conditions.

A theoretical model for the prediction of energy absorption capabilities of aluminum foam filled braided stainless steel tubes under tensile loading conditions has been developed based upon the unit cell concept. Comparisons between the energy absorption predictions of the analytical model and experimental observations were found to be in good agreement for assembly lengths of approximately 400 mm.

Experimental investigations were also completed for energy absorbers which function under axial compressive loading conditions. The crush characteristics and energy absorption capacity of AA6061-T6 extrusions with centrally located through-hole discontinuities were investigated and analyzed. Three different types of geometrical discontinuities, namely, circular, slotted and elliptical holes were fabricated into AA6061-T6 extrusions which had a length of 200 mm, nominal side width of 38.1 mm and wall thickness of 3.15 mm. It was found that by introducing crush initiators into the structural members, a splitting and cutting deformation mode was generated rather than global bending deformation. The peak crush load was reduced and total energy absorption was increased by incorporating the through-hole crush initiators.

Also investigated in this research for the improvement of energy absorption capacity was a new cutting deformation mode of extrusions. The four corners of square cross section AA6061-T6 extrusions were cut by a specially designed cutting tool. Tube lengths of 200 mm and 300 mm with a wall thickness of 3.15 mm and nominal side width of 38.1 mm were used in this research. Results from the experimental tests showed that the cutting deformation mode had high crush force efficiency and energy absorption capacity. An almost constant force/displacement response was observed for the tubes in the cutting deformation mode and two energy absorbing mechanisms were identified for this deformation process.

DEDICATION

To my wife Carol and my daughter Amy for your support, love and inspiration

ACKNOWLEDGEMENTS

I would like to express my sincere gratitude and profound appreciation to my supervisor, Dr. William Altenhof, for his patience, invaluable supervision, guidance, and thoughtful insights and so generously taking his time to discuss all aspects of this research. Without his guidance this project would have been impossible. My thanks also go to Mr. Bob Tattersall for his technical assistance in operating the experimental testing equipment used in this research.

TABLE OF CONTENTS

ABSTRACT	iii
DEDICATION	iv
ACKNOWLEDGEMENTS	v
LIST OF TABLES	ix
LIST OF FIGURES	x
LIST OF APPENDICES	xix
NOMENCLATURE	xx
ABBREVIATIONS	xxii
CHAPTER	
1. INTRODUCTION	1
2. LITERATURE REVIEW	4
2.1 Deformation modes of axially loaded tubular structure	5
2.1.1 Axial buckling	7
2.1.2 External inversion	13
2.1.3 Axial splitting	15
2.1.4 Interactive modes of deformation	21
2.1.5 Deformation mode of aluminum foam filled braided tube under tensile loading conditions	22
2.2 Factors that influence collapse mode	27
2.2.1 Cross section geometry	27
2.2.2 Extrusion Materials	29
2.2.3 Geometrical dimensions	34
2.3 Crash initiators	37
2.4 Analytical developments on the axial crushing of square tubes	47
2.5 Finite element modeling of the axial crushing of square tubes	51
3. FOCUS OF RESEARCH	56
4. EXPERIMENTAL TESTING METHOD	57
4.1 Overview of tensile testing of empty braided stainless steel tubes	57
4.2 Overview of tensile testing of aluminum foam filled braided tubes	59

4.3	Overview of tensile testing of aluminum extrusion material properties	62
4.4	Quasi-static axial crush testing	62
4.4.1	Quasi-static axial crush testing method	66
4.5	Quasi-static axial cutting testing	67
4.5.1	Cutting tool design and manufacture	68
4.5.2	Quasi-static axial cutting testing method	70
5.	PARAMETERS USED IN EVALUATING ENERGY ABSORPTION STRUCTURES	74
5.1	Peak buckling load	74
5.2	Total energy absorption	74
5.3	Mean crush force	75
5.4	Crush force efficiency	75
5.5	Specific energy absorption	75
6.	ANALYTICAL MODEL DEVELOPMENT AND COMPARISON WITH EXPERIMENTAL FINDINGS FOR ALUMINUM FOAM FILLED BRAIDED STAINLESS STEEL TUBE	77
6.1	Braided tube kinematic relationship between elongation and diameter	77
6.2	Energy absorbed by the aluminum foam filled braided tube	80
6.3	Energy absorbed by the aluminum foam core	80
6.4	Energy absorbed by the braided tube	83
6.5	Results and discussion	86
7.	EXPERIMENTAL RESULTS AND DISCUSSION FOR QUASI-STATIC AXIAL COMPRESSIVE CRUSHING AND CUTTING TESTS	88
7.1	Material property tensile testing results	88
7.2	Quasi-static axial compressive crush testing results and discussion	90
7.2.1	Crush test results for specimens in group 1 and group 2	90
7.2.2	Crush test results for specimens in group 3	95
7.2.3	Crush test results for specimens in group 4	97
7.2.4	Relationships between force/displacement profiles and Deformation	99
7.2.4.1	Specimens without any discontinuities (Group 1)	99
7.2.4.2	Specimens in sub-group C3	101
7.2.4.3	Specimens in sub-group S3-2	103
7.2.4.4	Specimens in sub-group E3-3	105
7.2.5	Energy absorption performance comparison between Specimens	107
7.2.5.1	Total energy absorption and crush force efficiency	107
7.2.5.2	Peak crush load and mean crush load	110

	7.2.5.3 Specific energy absorption	113
7.3	Quasi-static axial compressive cut testing results and discussion	115
	7.3.1 Cutting test results for specimen in group 1	116
	7.3.2 Cutting test results for specimen in group 2	119
	7.3.3 Cutting test results for specimen in group 3 and group 4	120
	7.3.4 Crush test results for specimen in group 5 and group 6	122
	7.3.5 Comparison of testing results amongst all specimens	124
	7.3.6 Crush performance parameter comparison amongst all specimens	125
	7.3.6.1 Peak load and mean crush force	125
	7.3.6.2 Crush force efficiency and total energy absorption	129
8.	CRUSH PERFORMANCE PARAMETERS COMPARISON BETWEEN DIFFERENT ENERGY ABSORBERS	133
9.	CONCLUSIONS	137
	9.1 Conclusions for aluminum foam filled braided stainless steel tube	137
	9.2 Conclusions for geometrical imperfections incorporated extrusions	138
	9.3 Conclusions for extrusions under cutting deformation mode	139
	9.4 Future work	140
	REFERENCES	141
	APPENDIX A: Experimental testing results of tensile testing of empty braided stainless steel tubes and tensile tests of aluminum foam filled braided tubes	146
	APPENDIX B: Copyright permission	154
	VITA AUCTORIS	162

LIST OF TABLES

Table		Page
2.1	Summary of the axial compression tests [6].	6
2.2	Empirical relationship between η and \varnothing for the collapse of various structures [51].	48
4.1	Mechanical characteristics of the AISI 304 stainless steel braid wire [62].	57
4.2	Specimen geometries in Group 2.	65
4.3	Specimen geometries in Group 3.	65
4.4	Specimen geometries in Group 4.	66
4.5	Hardness measurements of the cutter after heat treatment.	69
4.6	Blade tip width dimensions (in mm) of cutter on sides A and B.	70
4.7	Specimen grouping information and geometry.	72
7.1	Material properties from extrusion tensile tests [12].	88
7.2	Experimental testing results.	92
7.3	Experimental testing results.	115
8.1	Experimental cutting test results for displacement up to 100 mm.	134
8.2	Representative specimens for the performance measures comparison.	135
A.1	Energy absorption of the foam filled braided tubes.	149

LIST OF FIGURES

Figure		Page
1.1	Passenger vehicles deformed under both compressive and tensile loading conditions. (a) Compressive loading condition. (b) Tensile loading condition [4].	3
2.1	Various deformation modes of circular tubes as energy absorbers [6].	5
2.2	Axial force versus displacement curve for progressive buckling of circular tube under compression load [7].	7
2.3	Examples of various collapse modes for thin-walled circular 6060-T5 aluminium tubes under axial loading. (a) axi-symmetric mode ($D = 97.9$ mm; $t = 1.9$ mm; $L = 196$ mm); (b) non-symmetric mode ($D = 96.5$ mm; $t = 0.54$ mm; $L = 386$ mm); (c) mixed mode ($D = 97.5$ mm; $t = 1.5$ mm; $L = 350$ mm) [7].	8
2.4	Stress versus strain curves of extrusion materials considered by Langseth et al [11].	9
2.5	Deformation patterns of AA6061-T4 Aluminum extrusions with length of 200 mm, wall thickness of 3.15 mm, and nominal side width of 38.1 mm [12].	11
2.6	Experimentally obtained deformation pattern of AA6061-T6 Aluminum extrusion with circular hole discontinuity of 14.2 mm in diameter ($L=200$ mm, $D=14.2$ mm, $t=3.15$ mm) [12].	12
2.7	Experimentally obtained deformation pattern of AA6061-T6 Aluminum extrusion with circular hole discontinuity of 7.1 mm in diameter ($L=200$ mm, $D=14.2$ mm, $t=3.15$ mm) [12].	12
2.8	Schematic representation of the external inversion of tubes using a die [16].	13
2.9	Load versus displacement curves for copper tubes under quasi-static inversion process. Letters refer to Figure 2.10 [15].	14
2.10	Various stages of the inversion of a copper tube in quasi-static method [15].	15
2.11	Sketch of the experimental set-up, with 8 evenly spaced 5 mm initial saw-cuts around lower circumference [19].	16

Figure	Page
2.12 Typical force-displacement curves for mild steel tubes with $D=74.0$ mm; $t=1.8$ mm against dies with semi-angle $\alpha = 45^\circ, 60^\circ,$ and 75° respectively [19].	17
2.13 Photographs of typical mild steel specimens ($D=74.0$ mm; $t=1.8$ mm) after tests: from left to right $\alpha=45^\circ, \alpha=60^\circ, \alpha=75^\circ$ [19].	17
2.14 Typical force-displacement curves for aluminum tubes with $D=77.9$ mm; $t=1.9$ mm against dies with semi-angle $\alpha=45^\circ, \alpha=60^\circ, \alpha=75^\circ,$ respectively [19].	18
2.15 Photographs of typical aluminum specimens (with $D =77.9$ mm; $t =1.9$ mm) after tests: from left to right $\alpha=45^\circ, \alpha=60^\circ$ and $\alpha=75^\circ$ [19].	19
2.16 Typical force–displacement traces for mild steel square tubes with $t = 2.5$ mm against dies with semi-angle $\alpha = 45^\circ, 60^\circ$ and $75^\circ,$ respectively [20].	20
2.17 Photographs of typical specimens after tests [20].	20
2.18 Non-filled and filled square tubes under quasi-static compression [30].	21
2.19 Force versus displacement curve for compression of tube and foam [30].	22
2.20 Geometry of a braided tube in reference [34].	23
2.21 Tensile stress versus strain curve for three braids with polyurethane foam cores in reference [34].	24
2.22 (a) Geometry of a standard chain link (a racetrack link). (b) Contracted chain configuration used in composites [35].	25
2.23 Stress strain record for small-link chain-polycarbonate composite [36].	25
2.24 Aluminum foam filled braided tube secured into the tensile testing machine prior to loading [5].	26
2.25 Proposed cross-sections in reference [39].	27
2.26 Deformed shapes in reference [39].	28
2.27 Crushing forces displacement curve in reference [39].	28

Figure	Page
2.28 Experimental test set-up and controls: (a) test machine set-up; (b) collapse initiator geometry and (c) grooved end cap set for tube end constraints [40].	30
2.29 Experimental tests results: (a) fold formations and (b) load–displacement curves [40].	31
2.30 Strength-Elongation relationships for low strength, conventional HSS, and Advanced HSS steels [2].	32
2.31 Mercedes A-Class body structure [2].	33
2.32 Force displacement relationship of TRIP 590 Steel tube during drop tower crash test: diameter: 70 mm, wall thickness $t=1.61$ mm [41].	33
2.33 Force displacement curve of specimens made from different materials [41].	34
2.34 Experimental results from Abramowicz and Jones [14].	35
2.35 Empirical and theoretical transition lines found by Abramowicz et al [14].	36
2.36 Initiator geometry configurations studied by Krauss [46].	38
2.37 Numerically calculated force versus deflection curves for specimens with each size of circular crush initiator studied by Krauss [46].	39
2.38 Geometry and configurations of dents considered by Lee [47]. All dimensions are in millimetres.	40
2.39 The initial box is to the left. The drawn line indicates the location of the thermal trigger. On the right side the box is shown after approximately 130 mm of axial compression [48]. Reprinted with permission from SAE paper number 2003-01-2794 (c) 2003 Society of Automotive Engineers,	41
2.40 Yield stress values across a thermal trigger. The base material yield stress is about 220 MPa while yield stress within the 20 mm wide region representing the trigger is reduced to about 100-125 MPa [48]. Reprinted with permission from SAE paper number 2003-01-2794 (c) 2003 Society of Automotive Engineers,	41

Figure	Page
2.41 Fat line shows force displacement from a box having thermal triggers while thin lines show results from three boxes without triggers. The absorbed energy i.e. the integral under the curves is about the same in both experiments [48]. Reprinted with permission from SAE paper number 2003-01-2794 (c) 2003 Society of Automotive Engineers,	42
2.42 Front rail tip with rectangular trigger holes at the corners [49]. Reprinted with permission from SAE paper number 2005-01-0355 (c) 2005 Society of Automotive Engineers, Inc.	43
2.43 Trigger hole shapes and size [49]. Reprinted with permission from SAE paper number 2005-01-0355 (c) 2005 Society of Automotive Engineers, Inc.	43
2.44 Peak buckling load [49]. Reprinted with permission from SAE paper number 2005-01-0355 (c) 2005 Society of Automotive Engineers, Inc.	44
2.45 Crash column geometry and trigger hole locations [49]. Reprinted with permission from SAE paper number 2005-01-0355 (c) 2005 Society of Automotive Engineers, Inc.	45
2.46 Test specimens used in reference [12].	46
2.47 Mean total energy absorption for each crush test specimen group in reference [12].	46
2.48 Folding pattern of thin-walled box with very small thickness/width ratio [53]. Reprinted with permission from SAE paper number 811302 (c) 1981 Society of Automotive Engineers, Inc.	50
2.49 Folding pattern of thin-walled box with large thickness/width ratios [53]. Reprinted with permission from SAE paper number 811302 (c) 1981 Society of Automotive Engineers, Inc.	50
2.50 One quarter "finite element model including trigger position in reference [58].	52
2.51 Discretization of group B, G, and L specimens (L=200 mm, D=14.2 mm, t=3.15 mm) [13]. Reprinted with permission from SAE paper number 2005-01-0703 (c) 2005 Society of Automotive Engineers, Inc.	54
2.52 Experimental and numerical crushing process for T6 specimen [13]. Reprinted with permission from SAE paper number 2005-01-0703 (c) 2005 Society of Automotive Engineers, Inc.	55

Figure	Page
2.53 Experimental and numerical crushing process for T5 specimen [13]. Reprinted with permission from SAE paper number 2005-01-0703 (c) 2005 Society of Automotive Engineers, Inc.	55
4.1 Stainless steel braided tube geometry and tow profile	58
4.2 Circular clamping device.	59
4.3 Assembly process of the aluminum foam filled braided tubes.	60
4.4 Aluminum foam filled braided tube secured into the tensile testing machine prior to loading.	61
4.5 Geometries of the aluminum extrusion and discontinuities under consideration. L is the tube length, C is the width of the sidewalls and t is the wall thickness of the tube specimens.	64
4.6 Geometry of aluminum extrusion considered in this research. L is the tube length, C is the width of side walls and t is the nominal wall thickness.	67
4.7 Cutting tool shape and dimensions (all dimensions are in mm).	69
4.8 Cutting blade positions after manufacturing and heat treatment (side B facing upwards).	70
4.9 Cutting test setup. (a) Setup of the test prior to axial crushing, (b) penetration of blades of cutter into aluminum extrusion commencing on specimen SA2, (c) cutting in progression.	73
6.1 Unit cell geometry for theoretical model.	79
6.2 (a) Assumed initial cross sectional shape of the foam filled tube, (b) Assumed cross sectional shape of the foam filled tube at tow lockup, and (c) Theoretical model illustrating deformation of one quarter of the foam core.	83
6.3 Force/displacement behaviour of an empty braided tube with linear approximations in Region 1 and Region 2.	86
6.4 Energy/displacement behaviour of from experimental observations and the theoretical model.	87

Figure	Page
7.1 Engineering stress-strain curve of AA6061-T6 obtained from tensile testing [12].	89
7.2 Experimental obtained load/displacement profiles for specimens with circular discontinuities and specimen without discontinuity.	93
7.3 Experimental obtained load/displacement profiles for specimens with large slotted discontinuities and specimen without discontinuity.	93
7.4 Experimental obtained load/displacement profiles for specimens with large elliptical discontinuities and specimen without discontinuity.	94
7.5 Deformation modes observed for specimens in Group 1 and Group 2, W0 in global bending, C2, S2-2, S2-1, E2-2 and E2-1 in SMI, S2-3 and E2-3 in SMII.	94
7.6 Experimental obtained load/displacement profiles for specimens with medium slotted discontinuities and specimen without discontinuity.	95
7.7 Experimental obtained load/displacement profiles for specimens with medium elliptical discontinuities and specimen without discontinuity.	96
7.8 Deformation modes of specimens in Group 3. All specimens deformed in SMII mode.	96
7.9 Experimental obtained load/displacement profiles for specimens with small slotted discontinuities and specimen without discontinuity.	97
7.10 Experimental obtained load/displacement profiles for specimens with small elliptical discontinuities and specimen without discontinuity.	98
7.11 Deformation modes of specimens in Group 4. All specimens deformed in SMII mode.	98
7.12 Experimentally obtained load versus displacement profile for a specimen without any discontinuity.	100
7.13 Photographs illustrating the crushing process for a specimen without any discontinuity.	101
7.14 Experimentally obtained load versus displacement profile for a representative specimen from sub-group C3.	102

Figure	Page
7.15 Photographs illustrating the crushing process for a representative specimen from sub-group C3.	103
7.16 Experimentally obtained load versus displacement profile for a representative specimen from sub-group S3-2.	104
7.17 Photographs illustrating the crushing process for a representative specimen from sub-group S3-2.	105
7.18 Experimentally obtained load versus displacement profile for a representative specimen from sub-group E3-3.	106
7.19 Photographs illustrating the crushing process for a representative specimen from sub-group E3-3.	106
7.20 Total energy absorption and <i>CFE</i> for specimens in Group 2 (observations from specimen in Group 1 are included for comparison).	109
7.21 Total energy absorption and <i>CFE</i> for specimens in Group 3 (observations from specimen in Group 1 are included for comparison).	109
7.22 Total energy absorption and <i>CFE</i> for specimens in Group 4 (observations from specimen in Group 1 are included for comparison).	110
7.23 Peak and mean crush loads for specimens in Group 2 (observations from specimen in Group 1 are included for comparison).	111
7.24 Peak and mean crush loads for specimens in Group 3 (observations from specimen in Group 1 are included for comparison).	112
7.25 Peak and mean crush loads for specimens in Group 4 (observations from specimen in Group 1 are included for comparison).	112
7.26 Specific energy absorption for specimens in Group 2 (observations from specimen in Group 1 are included for comparison).	113
7.27 Specific energy absorption for specimens in Group 3 (observations from specimen in Group 1 are included for comparison).	114
7.28 Specific energy absorption for specimens in Group 4 (observations from specimen in Group 1 are included for comparison).	114

Figure	Page
7.29 Photographs of the cutting process for specimen SA1. (a) Cutting setup using side A of the cutter, (b) splitting of the four corners of the specimen, (c) petalled side wall bending outwards, (d) and (e) progression of cutting, and (f) specimen after testing.	117
7.30 Experimentally obtained load versus displacement curves for specimens in group 1; positions b, c, d and e correspond to photographs in Figure 7.29.	118
7.31 Chip formation and petalled side wall bending for specimen SA4. (a) During cutting (side view), (b) after testing (rear view), (c) after testing (front view).	119
7.32 Experimentally obtained load versus displacement curves for specimens in group 2.	120
7.33 Experimentally obtained load versus displacement curves for specimens in group 3.	121
7.34 Experimentally obtained load versus displacement curves for specimens in group 4.	122
7.35 Experimentally obtained load versus displacement curves for specimens in group 5.	123
7.36 Experimentally obtained load versus displacement curves for specimens in group 6.	124
7.37 Force/displacement profile comparisons for representative specimens from each group.	125
7.38 Peak load and mean crush force comparison for specimens in groups 1 and 2.	127
7.39 Peak load and mean crush force comparison for specimens in groups 3 and 4.	128
7.40 Peak load and mean crush force comparison amongst representative specimens from each group.	129
7.41 Crush force efficiency and total energy absorption comparison for specimens in groups 1 and 2.	130

Figure	Page
7.42 Crush force efficiency and total energy absorption comparison for specimens in groups 3 and 4.	131
7.43 Crush force efficiency and total energy absorption comparison amongst representative specimens from each group.	132
8.1 Experimentally obtained load/displacement profiles comparison.	135
8.2 Peak crush load and mean crush load comparison.	136
8.3 Total energy absorption and crush force efficiency comparison.	136
A.1 Force versus displacement characteristics for the empty braided tubes of 185 mm and 330 mm lengths.	147
A.2 Force/displacement and energy/displacement curves of the foam filled braided tube for specimen 1 with $\rho_f = 248.2 \text{ kg/m}^3$.	150
A.3 Force/displacement and energy/displacement curves of the foam filled braided tube for specimen 3 with $\rho_f = 288.2 \text{ kg/m}^3$.	151
A.4 Force/displacement and energy/displacement curves of the foam filled braided tube for specimen 4 with $\rho_f = 298.2 \text{ kg/m}^3$.	152
A.5 Force/displacement and energy/displacement curves of the foam filled braided tube for specimen 5 with $\rho_f = 373.4 \text{ kg/m}^3$.	153

LIST OF APPENDICES

Appendix		Page
A	Experimental testing results of tensile testing of empty braided stainless steel tubes and tensile tests of aluminum foam filled braided tubes	146
B	Copyright permission	154

NOMENCLATURE

C	Side width of a square tube extrusion
D	Perpendicular distance between the tows
E	Young's modulus
$E_{absorbed}$	Energy absorbed
E_{foam}	Energy absorbed by aluminum foam
E_{total}	Total energy absorbed by the structure
E_{tube}	Energy absorbed by braided tube
F	Radial force acting on the surfaces of the aluminum foam core
F_z	Force in z-axis direction
i	Index for the i^{th} data point
k_1	Empty braided tube stiffness in Region 1
k_2	Empty braided tube stiffness in Region 2
L	Length of energy absorber
L_0	Initial length of braided tube
L_{crit}	Intersection point of the assumed linear force/displacement relationship for Region 1 and Region 2
L_{foam}	Length of aluminum foam core
L_{lockup}	Tube length at lockup
l	Unit cell length
l_x	Unit cell length along x direction
l_y	Unit cell length along y direction
m	Mass of energy absorber
N	Number of data points
P	Axial crushing force
P_m	Mean axial crushing load
P_{max}	Maximum load observed during axial crushing
R	Current radius of aluminum foam filled braided tube during deformation
R_0	Radius of braided tube after assembly of the aluminum foam filled braided tube

R_{lockup}	Radius of braided tube after lockup
t	Wall thickness of a square tube extrusion
U_{foam}	External work done on the aluminum foam
W	Width of tow
W_0	Initial width of aluminum foam cross section
W_{lockup}	Width of aluminum foam cross section after braided tube lockup
z	Tube length after elongation in z axis direction
δ	Crosshead displacement in the axial direction
δ_t	Total crosshead displacement in the axial direction
σ_{pl}	Plateau stress of aluminum foam
θ_0	Initial angle between tows after assembly of the aluminum foam filled braided tube
θ	Current angle between tows in the unit cell of the braided tube
θ_L	Lockup angle between tows in the unit cell of the braided tube
σ_u	Ultimate stress
σ_y	Yield stress

ABBREVIATIONS

<i>IIHS</i>	Insurance Institute for Highway Safety
<i>FE</i>	Finite Element
<i>AA</i>	Aluminum Alloy
<i>AISI</i>	American Iron and Steel Institute
<i>ASTM</i>	American Society for Testing and Materials
<i>CFE</i>	Crush force efficiency
<i>CNC</i>	Computer numeric control
<i>LVDT</i>	Linear voltage differential transformer
<i>NHTSA</i>	National highway traffic safety administration
<i>SEA</i>	Specific energy absorption
<i>SMI</i>	Splitting collapse mode I
<i>SMII</i>	Splitting collapse mode II

1. INTRODUCTION

During the past decade, passenger vehicle occupant safety features have become a leading marketing characteristic of motor vehicles. Vehicle crashworthiness rating as provided by testing organizations, such as NHTSA (National Highway Traffic Safety Administration) and IIHS (Insurance Institute for Highway Safety), is currently ranked at a level comparable to quality, styling, ride and handling, and fuel economy [1]. Automotive manufacturers, government agencies, insurance underwriters, and the news media provide consumers with significant amounts of safety information about each model of new cars. Vehicle engineers design safety features such as energy absorbing front and side structures, air bags, seats with integrated seat belts, and various crash avoidance devices, such as anti-lock braking systems, traction control devices and daytime running lamps, to satisfy a number of regulatory requirements and consumer information programs. The research on vehicle safety, meaning structural crashworthiness and reduction in occupant fatalities and harm, will undoubtedly continue to increase during the next decades in response to consumer demands, increasing government regulation and globalization of the industry.

The contents of this research focused on component structural crashworthiness, deformation mode and energy absorption improvements. During a crash event, the majority of vehicle's kinetic energy is absorbed through the plastic deformation of the side walls of the main energy absorbing structural members. The frontal rails in the automotive supporting frame generally act as the main structural members for absorbing crash energy in a frontal impact, and the crushable length of these components defines the distance over which the crash energy can be absorbed. Bumpers are designed to protect car bodies from damage in low-speed collisions (8 km/h). Bumper-to-frame rail attachments are designed to transfer the impact force directly to the front rails.

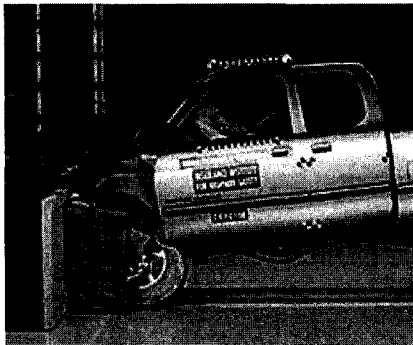
Progressive buckling is the most preferred mode of collapse during front and rear end crashes as it results in a more stable and predictable energy absorption behaviour. Researchers are trying to control the deformation mode and energy absorption capacity of a structure to achieve a uniform deceleration, for example 20-25 g's when measured in a fixed barrier, frontal crash at 48 km/h.

To achieve the goal of high structure crashworthiness, material selection is critical. The basic requirements for automobile structure materials include good formability, corrosion resistance, and recyclability. Structural materials should also possess sufficient strength and controlled deformations under load to absorb crash energy, yet maintain sufficient survivable space for adequate occupant protection should a crash occur. Furthermore, the structure should be lightweight to reduce fuel consumption. Carbon steel and advanced high strength steels (AASS), such as dual phase (DP) and transformational induced plasticity (TRIP) steels have been extensively used in the automotive industry [2]. In the meantime, light weight materials especially aluminum has been increasingly used in automobiles. Since 1990, the use of aluminum has doubled in cars and has tripled in SUVs and pick-ups [3]. The use of aluminum material for car structures can provide the following advantages:

- The high strength-to-weight ratio of aluminum allows strong, yet lightweight body structures to be built.
- Aluminum structural members can be engineered to collapse in a predictable manner in severe impacts and, as a result, can be readily designed to provide the desired amount of crash energy absorption.
- The superior corrosion resistance of aluminum minimizes deterioration of the crash energy absorption capabilities over the life of the vehicle.
- Aluminum absorbs twice as much crash energy as typical automotive steel so that as vehicle weight reduction becomes inevitable, substituting aluminum for steel will provide simultaneous improvement in fuel economy, performance and safety; a truly compelling combination for vehicle manufacturers and their customers [3].

Figure 1.1 (a) and (b) indicate that during frontal impact and side impact, vehicle structure would deform under compressive and tensile loading conditions separately. Requirements exist for passenger vehicles to absorb crash energy and protect occupant compartment under both conditions. The research done for this thesis involves the study of energy absorbing structural components under different loading conditions. The objective of this research is to examine the effect of different geometrical imperfections, in the form of circular, elliptical, and slotted holes, and deformation modes on the

crashworthiness characteristics of axially loaded extruded aluminum tubes. Experimental quasi-static crush tests will be used to determine the collapse mode, load/displacement characteristics, and energy absorption ability of aluminum extrusions. Aluminum foam filled braided stainless steel tube as a new energy absorbing device under tensile loading conditions was experimentally investigated by Altenhof et al. as reported in reference [5]. A theoretical mode will be developed in this research to predict its energy absorption capacity according to experimental observations and analysis of deformation process.



(a)



(b)

Figure 1.1. Passenger vehicles deformed under both compressive and tensile loading conditions. (a) Compressive loading condition. (b) Tensile loading condition [4].

2. LITERATURE REVIEW

With the establishment of the National Highway Traffic Safety Administration (NHTSA) in 1970, many mandatory safety standards, known as Federal Motor Vehicle Safety Standards (FMVSS) were introduced [1]. These standards regulate many aspects of vehicle crashworthiness and crash avoidance performance. As a consequence of these regulations and consumer requirements, researchers in different areas have published a large number of papers to address structural crashworthiness, restraint systems, and injury biomechanics. As related to the research of this thesis, the literature review discusses the experimental testing, theoretical analysis and numerical simulation of tubular structural collapse behaviour and crash energy absorption under quasi-static and dynamic axial loading conditions. Section 2.1 discusses the collapse modes of axially loaded tubes under quasi-static and dynamic loading conditions. Experimental testing and results from other researchers are discussed in this part. Section 2.2 discusses factors that influence the collapse mode of axially loaded square tubes. These factors include material properties, cross section shapes and geometrical dimensions. Section 2.3 details some of the research done with crush initiators, which include inherent imperfections introduced by the manufacturing process and intentionally created geometrical discontinuities for the purpose of altering energy absorption characteristics. Section 2.4 discusses the theoretical analyses regarding the prediction of peak buckling load and mean crush load for square tubes developed by various researchers. Section 2.5 discusses the use of finite element methods in the analysis of the axial crushing process.

2.1 Deformation Modes of Axially Loaded Tubular Structures

The majority of research dealing with impact energy absorption has focused on the behaviour of metal structures and components for which the main energy absorbing mechanisms are plastic deformation and fracture [6]. Reid [6] investigated three primary axial deformation modes of metal components proposed as impact energy absorbers. Seamless mild steel tubes, of 50.8 mm outside diameter and 1.6 mm wall thickness, were used in the experimental tests. The deformation modes investigated included axial buckling, inversion and axial splitting. The first deformation mode was achieved through compression of steel tube between two parallel plates. The last two deformation modes required the use of a profiled die onto which the tubes were compressed. The three deformation modes and different tools used in the crushing process are illustrated in Figure 2.1.

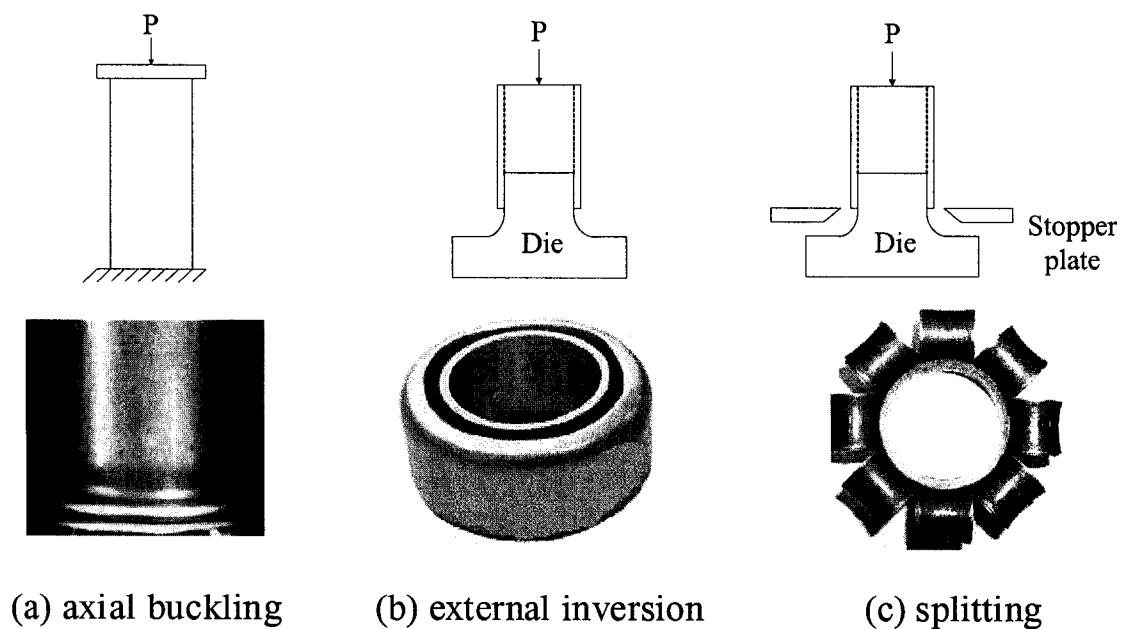


Figure 2.1. Various deformation modes of circular tubes as energy absorbers [6].

A summary of the principal features of the test results is provided in Table 2.1. The first two modes which did not involve fracture possessed a high mean load reflecting the efficient mechanisms consisting principally of circumferential stretching and axial bending about circumferential hinges. The stroke or effective crushing length is of the order of 70% of the tube length. For the splitting mechanism, the lower mean loads were offset by the increased stroke of 95%, resulting in comparable energy absorbing capacities. Particular benefits for external inversion mode and axial splitting mode were the almost constant force in the deformation processes.

Table 2.1. Summary of the axial compression tests [6].

Deformation mode	Mean load (kN)	Compression (=stroke %)	Energy absorption (J/mm)
Axial buckling	80.0	70	56.0
Inversion (Radium of Die = 4 mm)	85.0	66	56.1
Inversion (Radium of Die = 6 mm)	80.0	70	56.0
Splitting (Radium of Die = 4 mm)	60.0	95	57.0
Splitting (Radium of Die = 6 mm)	42.5	95	40.4
Splitting (Radium of Die = 10 mm)	30.0	95	28.5

For each of the above mentioned three primary deformation modes, there exist different deformation patterns, which will be discuss further in the following paragraphs.

2.1.1 Axial Buckling

Axial buckling deformation mode occurs when thin walled tubes are compressed between two parallel flat plates. For a circular tube, depending on geometrical parameters such as the ratios of D/t (diameter/thickness) and L/D (length/diameter) and also on material properties, there are a variety of possible patterns of collapse. Generally, deformation pattern includes progressive buckling, the formation of progressive folds whether axi-symmetrically or non-symmetrically, and global bending. In progressive buckling mode, the formation of folds causes the characteristic fluctuation in the axial force shown in Figure 2.2 [7].

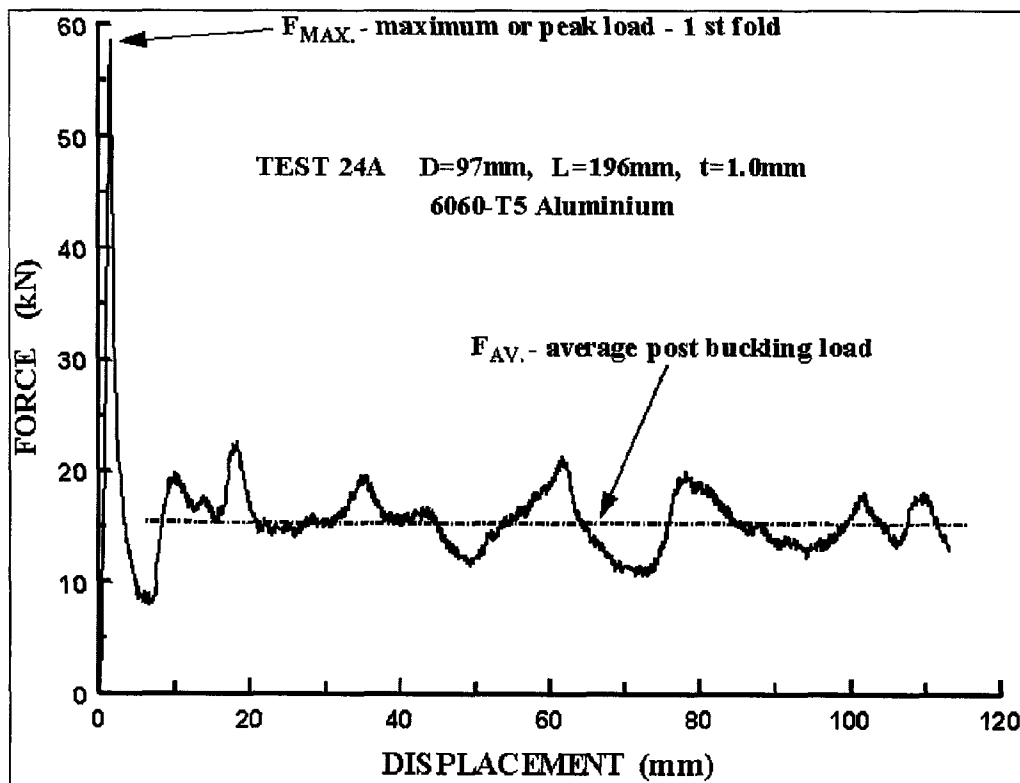


Figure 2.2. Axial force versus displacement curve for progressive buckling of circular tube under compression load [7].

Guillow et al. [7] have experimentally investigated the axial compression of thin-walled circular tubes. A total of 70 quasi-static tests were conducted on circular 6060 aluminum tubes in the T5 temper. The range of D/t was between 10 to 450 and $L/D \leq 10$

in the testing. The following modes of collapse have been identified and Figure 2.3 shows some typical examples: (i) axi-symmetric concertina buckling, (ii) non-symmetric buckling (also known as diamond or Yoshimura mode), with a variable number of circumferential lobes or corners (refer to Figure 2.3), (iii) mixed mode (combination of the two previous modes), (iv) Euler or global buckling; and (v) other (simple compression, single folds, etc.).

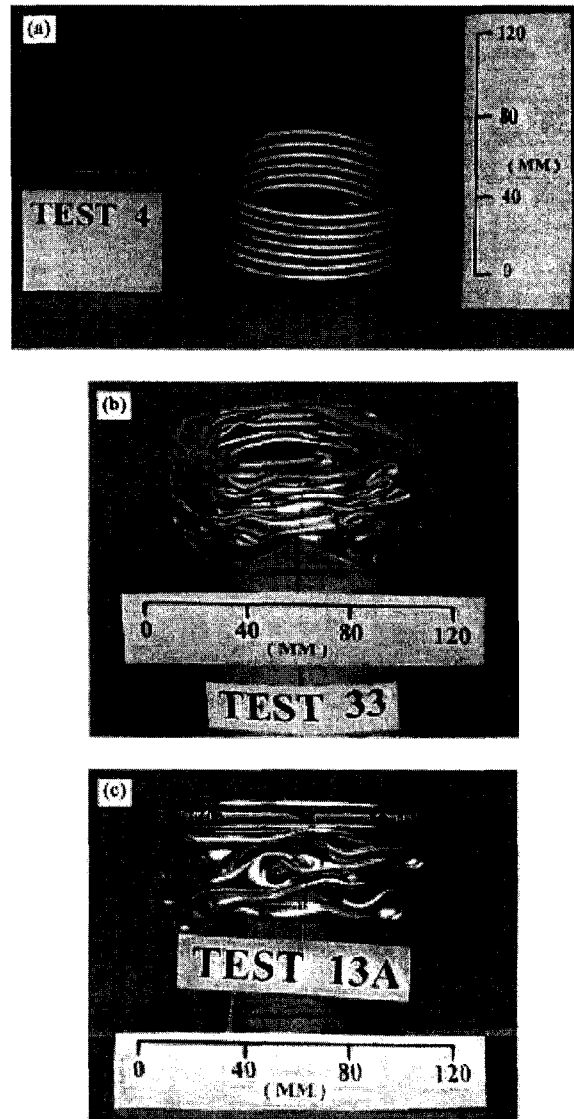


Figure 2.3. Examples of various collapse modes for thin-walled circular 6060-T5 aluminium tubes under axial loading. (a) axi-symmetric mode ($D = 97.9$ mm; $t = 1.9$ mm; $L = 196$ mm); (b) non-symmetric mode ($D = 96.5$ mm; $t = 0.54$ mm; $L = 386$ mm); (c) mixed mode ($D = 97.5$ mm; $t = 1.5$ mm; $L = 350$ mm) [7].

Abramowicz and Jones [8-10] have done extensive experimental crush testing and theoretical analyses on tubular structures under quasi-static and dynamic loading conditions. Tubes with a wide range of lengths, widths and wall thickness have been considered in their research. In reference [8], quasi-static crush tests were performed on a DARTEC 250 kN hydraulic testing machine at a crushing rate in the range of 0.1-1.0 mm/s. The crushing load was applied using two steel plates, a moving crosshead plate and a stationary base plate. The collapse modes observed in this experimental study were the global bending mode, the progressive symmetric mode, and the progressive extensional mode.

Langseth and Hopperstad [11] experimentally investigated the crush behaviour of axially loaded aluminum extrusions with square cross-sections. Tubes made of the aluminum alloy AA6060 with the T6 and T4 heat treatments, as well as a modified T4 heat treatment were studied. The stress-strain curves for these materials are illustrated in Figure 2.4. All tubes had a length of 310 mm and a width of 80 mm, while wall thickness values of 1.8, 2.0, and 2.5 mm were considered. The tests were conducted at a constant crosshead speed of 0.15 mm/s using a DARTEC 500 kN testing machine.

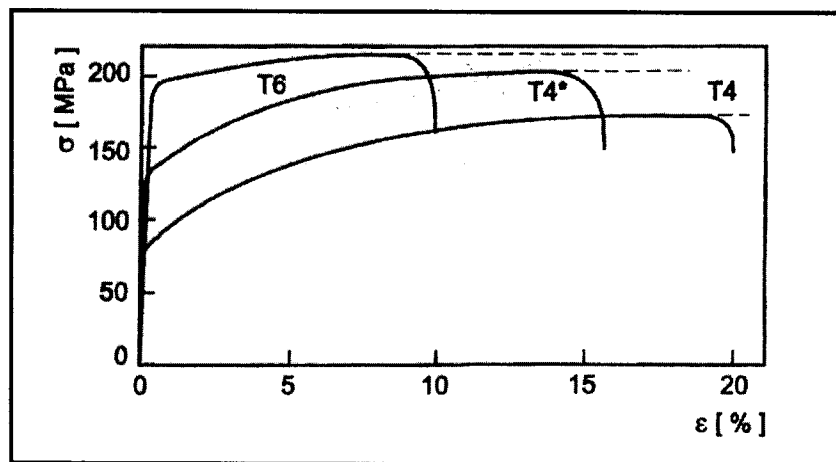


Figure 2.4. Stress versus strain curves of extrusion materials considered by Langseth et al [11].

It was reported in reference [11] that material hardening properties and tube geometry had important influences on the mean crushing load and energy absorption of square aluminum tube extrusions subjected to axial crushing. Even though all tubes collapsed in the symmetric mode regardless of heat treatment or wall thickness, the number of lobes formed was found to be dependant solely on heat treatment. Six lobes were formed in the tubes with T4 heat treatment, between 6 and 7 were formed in the tubes with the modified T4 treatment, and 7 were formed in the tubes with the T6 heat treatment.

The mean crushing load and energy absorption were higher for the tubes with the T6 heat treatment than for the tubes with the T4 heat treatment, due to the differences in yield strength of the materials. However, the ratio of the mean load of the tubes treated with the T6 heat treatment to that of the tubes treated with the T4 heat treatment decreased with increasing wall thickness. Langseth and Hopperstad [11] attributed this to the difference in hardening properties between the two heat treatment conditions. Increasing the wall thickness causes an increase in strains yielding a significant increase in plastic flow stress for the T4 condition. Due to the lower hardening modulus for the T6 condition, no flow stress increase occurs for the tubes with the T6 heat treatment condition.

For thin walled square tubes, Arnold and Altenhof [12,13] have experimentally and numerically investigated the deformation patterns of AA6061 T4 and T6 square tubes. In this research, specimens with length of 200 mm and 300 mm, wall thickness of 3.15 mm, and nominal side width of 38.1 mm have been axially crushed to observe deformation patterns and energy absorption behaviour. Specimen geometry was chosen to have a predicted global bending collapse pattern based on the research work of Abramowicz and Jones [14]. Centrally located circular holes, with diameters of 7.1 mm and 14.2 mm machined into the two opposing walls of the tubes, were used as crush initiators to commence the plastic buckling process. For specimens of T4 temper without discontinuity, the deformation patterns observed were illustrated in Figure 2.5. Specimen #1 deformed in the global bending pattern. Specimen #2 collapsed in the progressive-symmetric pattern. Specimen #3 collapsed in the progressive-asymmetric mode as shown by the non-uniform folding pattern. Specimen #4 initially collapsed in the progressive-

asymmetric mode, which led to a severe global bending. It can be observed that tubes with assumed same geometry and material properties can exhibit different deformation modes. This difference could be caused by the inherent imperfections of the structure induced during the manufacture and heat treatment process.

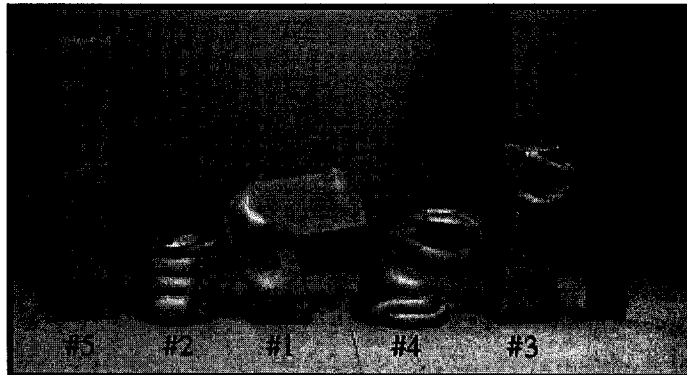


Figure 2.5. Deformation patterns of AA6061-T4 Aluminum extrusions with length of 200 mm, wall thickness of 3.15 mm, and nominal side width of 38.1 mm [12].

Another two deformation patterns, namely SMI and SMII, were reported for specimens of T6 temper with circular hole discontinuities of diameter 14.2 mm and 7.1 mm as illustrated in Figure 2.6 and Figure 2.7. A lateral shift of the top half of the absorber relative to the bottom half was observed for mode SMI. As the lateral shift continued, the top half of the absorber was only supported by a small cross-section of the bottom half. This resulted in a large stress concentration that ultimately led to a splitting mode in which the top half of the absorber acted as a cutter that split the bottom half. In mode SMII, the top portion of the absorber was driven down inside the bottom portion, causing the sidewalls to split at the corners.

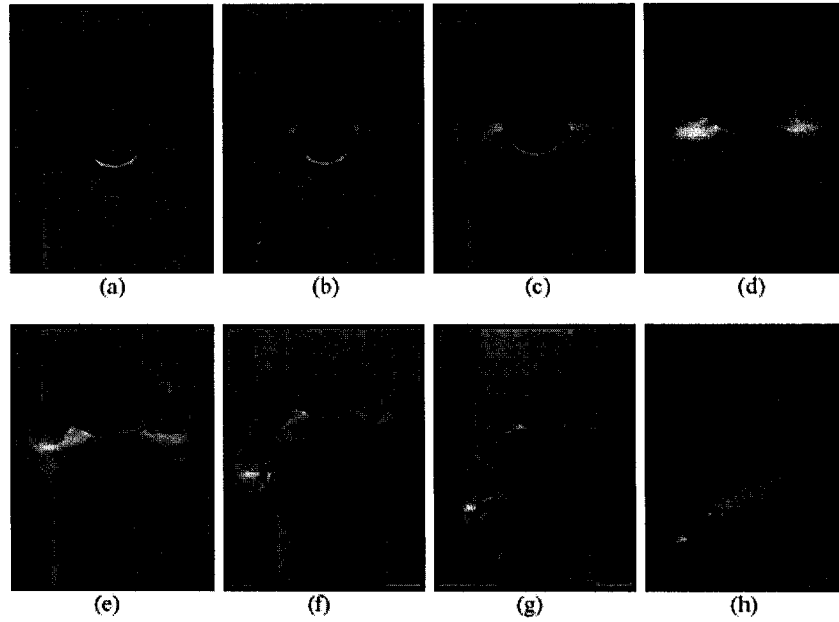


Figure 2.6. Experimentally obtained deformation pattern of AA6061-T6 Aluminum extrusion with circular hole discontinuity of 14.2 mm in diameter ($L=200$ mm, $D=14.2$ mm, $t=3.15$ mm) [12].

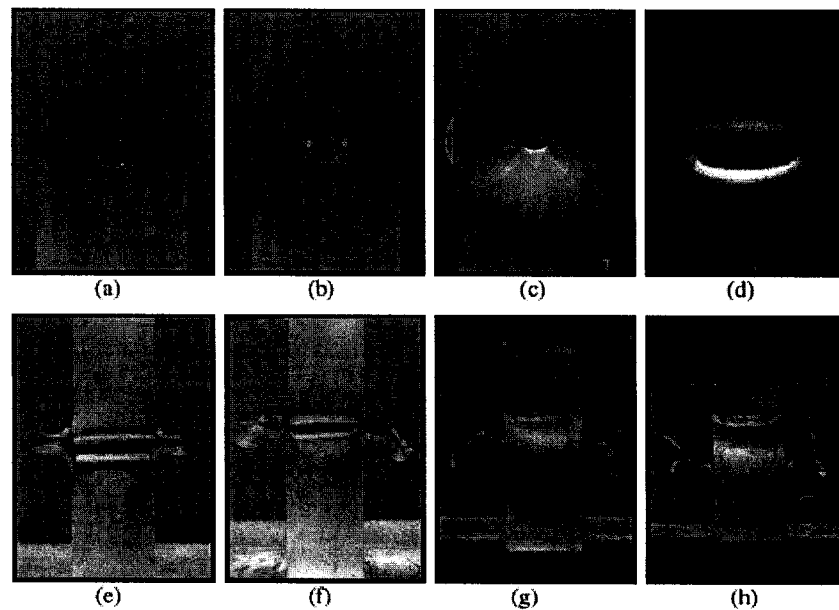


Figure 2.7. Experimentally obtained deformation pattern of AA6061-T6 Aluminum extrusion with circular hole discontinuity of 7.1 mm in diameter ($L=200$ mm, $D=14.2$ mm, $t=3.15$ mm) [12].

2.1.2 External Inversion

External inversion deformation is a process in which a tube, when subjected to axial compression, will undergo inside-out inversion to form a double walled part [6]. Inversion of tube for energy absorbers was pioneered by General Motors as indicated in reference [15]. Recently, however, this process has also been steered toward practical and industrial application, particularly in the metal-forming area [15]. The large plastic strains involved in tube inversion limit its occurrence to ductile materials, such as steels and aluminium alloys.

The external inversion of a tube using a die is characterized by the axial compression of a tube over a die with an appropriate radius as shown in Figure 2.8 [16]. The plastic deformation of the tube is the result of three different mechanisms: bending, stretching and friction [17].

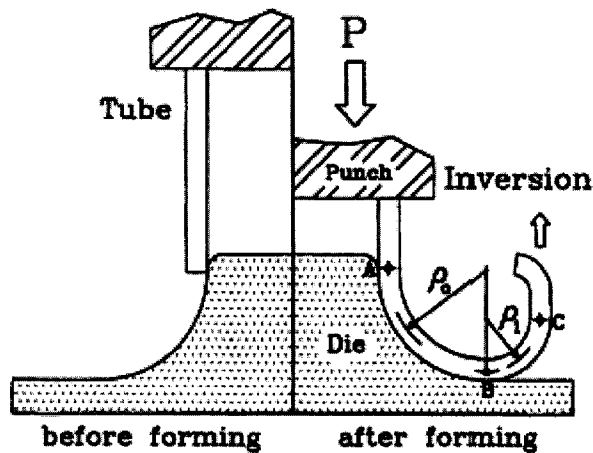


Figure 2.8. Schematic representation of the external inversion of tubes using a die [16].

Information regarding theoretical and experimental fundamentals of the external inversion of tubes using a die can be found in references [6, 15-17]. These publications investigated issues related to the prediction of load, to the identification of the main parameters that govern the process, and to the classification of the typical patterns of deformation that may occur during the process (successful inversion, local buckling and fracture) and to the influence of interface friction on material, material damage and fracture.

Miscow and Al-Qureshi [15] have performed an experimental and theoretical analysis of tube inversion under quasi-static and dynamic loading conditions. At the start of each test, the tube (outside diameter of 50.8 mm, wall thickness of 1.58 mm, and height of 88.9 mm) was placed over a lubricated die. Then, the operation was performed simply by subjecting the ends of the tube to an increasing axial (quasi-static or dynamic) load. In the case of quasi-static testing, the die assembly was attached to the lower platen of the hydraulic testing machine (capacity of 200 kN, velocity of 20 mm/min). Whereas, the punch was fixed to the movable upper ram. A typical load versus displacement curve for copper tube using die radius of 4.76 mm is shown in Figure 2.9, submitted to quasi-static axial compressive loading. It can be seen that from the initial flaring outwards of the material covering the die radius, until the final steady-state inversion, the tube passed through many stages. Typical samples of the tubes at various stages of external inversion were shown in Figure 2.10.

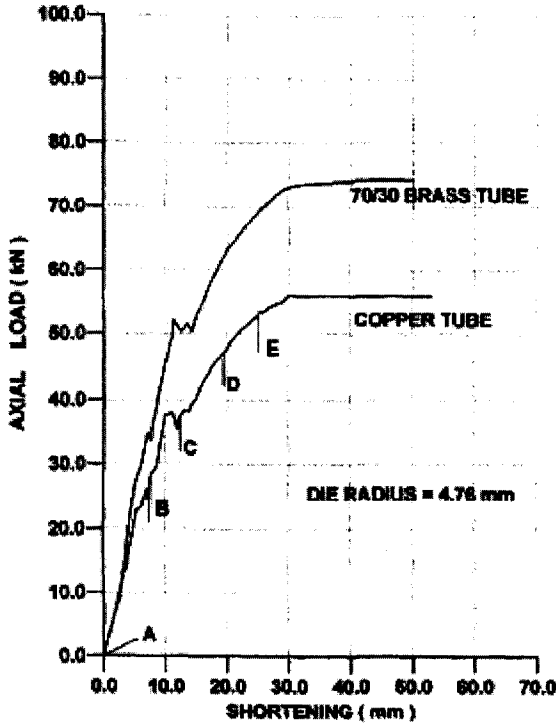


Figure 2.9. Load versus displacement curves for copper tubes under quasi-static inversion process. Letters refer to Figure 2.10 [15].

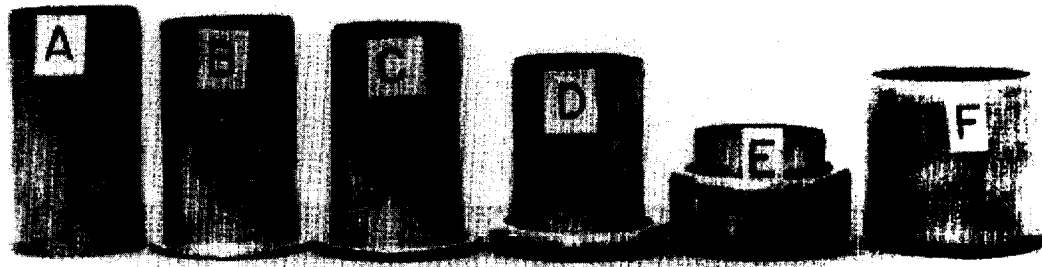


Figure 2.10. Various stages of the inversion of a copper tube in quasi-static method [15].

2.1.3 Axial Splitting

A splitting deformation mode was seen as a failure mode for tube inversion, but has been developed as an energy absorbing mechanism [6]. From the viewpoint of energy absorption, this collapse mode has a long stroke of over 90 per cent of the total tube length. Stronge et al. [18] conducted experiments with square tubes split against a radius/flat die. Huang et al. [19, 20] studied the splitting and curling behaviour of circular and square tubes axially compressed between a plate and a pyramidal die. Lu et al. [21] investigated the tearing energy involved in splitting square metal tubes. Tearing energy in thin metal sheets was studied by Lu et al. [21], Yu et al. [22] and Fan et al. [23], among others. Reddy and Reid [24] studied the splitting behaviour of circular tubes compressed axially between a plate and a radius die.

The splitting deformation mechanism has advantages for energy absorption in that it has a long stroke while steady crush force. During the splitting process, cracks were observed to propagate along the axial direction. Strips rolled up into curls with an almost constant radius after splitting. The crush force became steady after some initial fluctuations. Three energy dissipation mechanisms were involved: (1) Splitting and tearing of the tube; (2) plastic bending and stretching; (3) the friction as the tube interacted with the die [19].

Huang et al. [19] have investigated the axial splitting and curling behaviour of circular metal tubes. Mild steel and aluminum circular tubes (with yield stress $\sigma_y = 450$ MPa for mild steel, and $\sigma_y = 180$ MPa for aluminum) were pressed axially onto a

series of conical dies each with different semi-angles. By pre-cutting eight 5 mm slits which were distributed evenly at the lower end of each tube, the tube split axially and the strips curled outward. The experimental set-up is sketched in Figure 2.11. A cone-shaped die was fixed to the bottom bed of the testing machine. A short cylindrical mandrel was used inside the tube to prevent the tube from tilting. The axes of the die, tube and testing machine were carefully aligned. The cross-head of the testing machine then pressed the tube onto the conical die at a constant rate of 0.0333 mm/s. Three different semi-angles of 45, 60 and 75 were selected for the conical die. All dies were made from mild steel and heat-treated to increase their surface hardness. All the specimens tested were commercially available circular tubes with length of 200 mm long. The ratio of the diameter to the thickness ranges from 15 to 50. Typical force-compression curves for mild steel tubes ($D = 76.0$ mm and $t = 2.0$ mm) with three different dies are shown in Figure 2.12 and the corresponding specimen photographs after tests are shown in Figure 2.13 with side and end views.

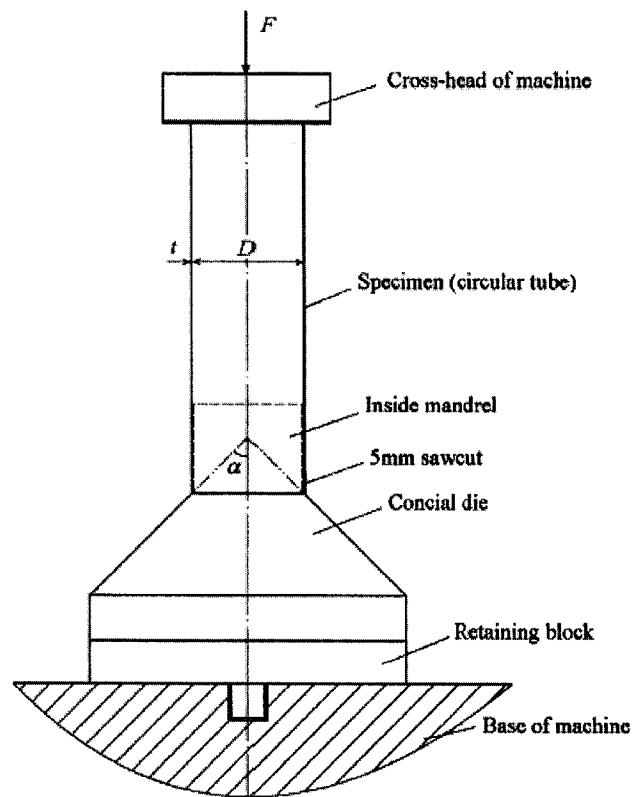


Figure 2.11. Sketch of the experimental set-up, with 8 evenly spaced 5 mm initial saw-cuts around lower circumference [19].

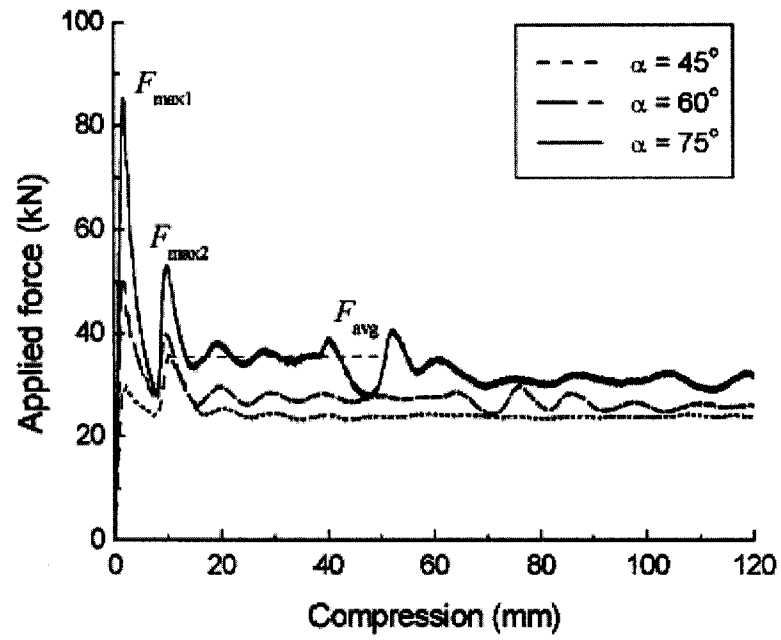


Figure 2.12. Typical force-displacement curves for mild steel tubes with $D=74.0$ mm; $t=1.8$ mm against dies with semi-angle $\alpha = 45^\circ$, 60° , and 75° respectively [19].

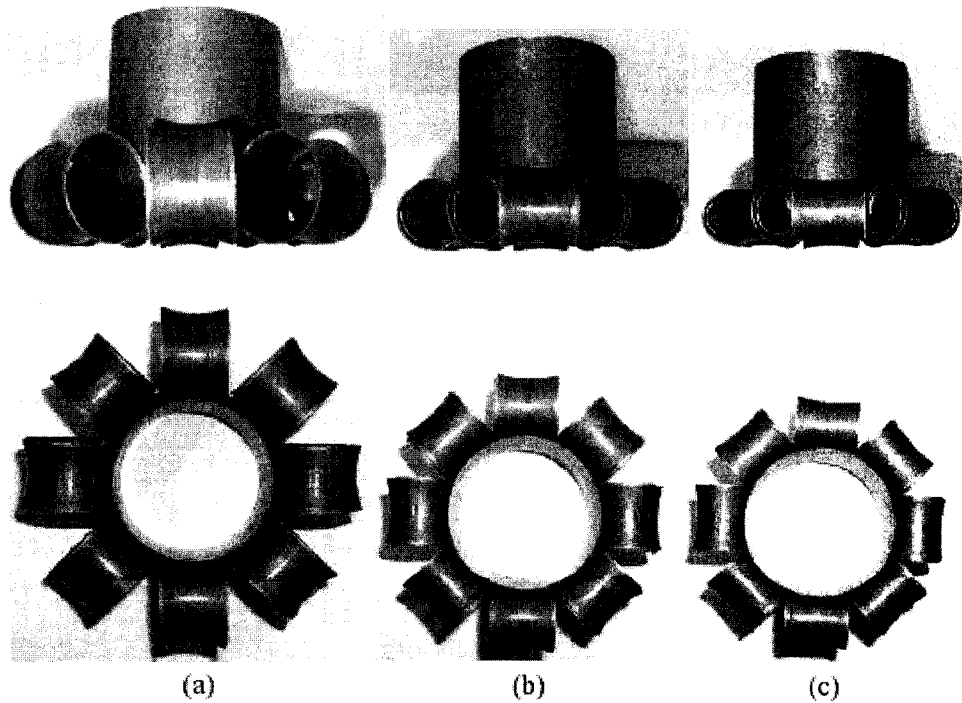


Figure 2.13. Photographs of typical mild steel specimens ($D=74.0$ mm; $t=1.8$ mm) after tests: from left to right $\alpha=45^\circ$, $\alpha=60^\circ$, $\alpha=75^\circ$ [19].

Figure 2.14 shows typical force-compression curves for the aluminum tubes pressed onto three different semi-angled dies. Corresponding specimen photographs after tests are shown in Figure 2.15.

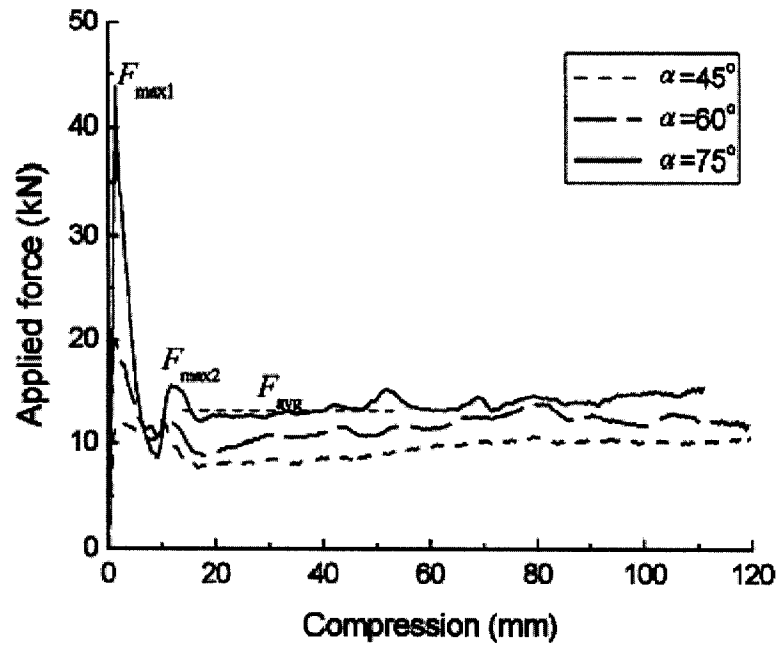


Figure 2.14. Typical force-displacement curves for aluminum tubes with $D=77.9$ mm; $t=1.9$ mm against dies with semi-angle $\alpha=45^\circ$, $\alpha=60^\circ$, $\alpha=75^\circ$, respectively [19].

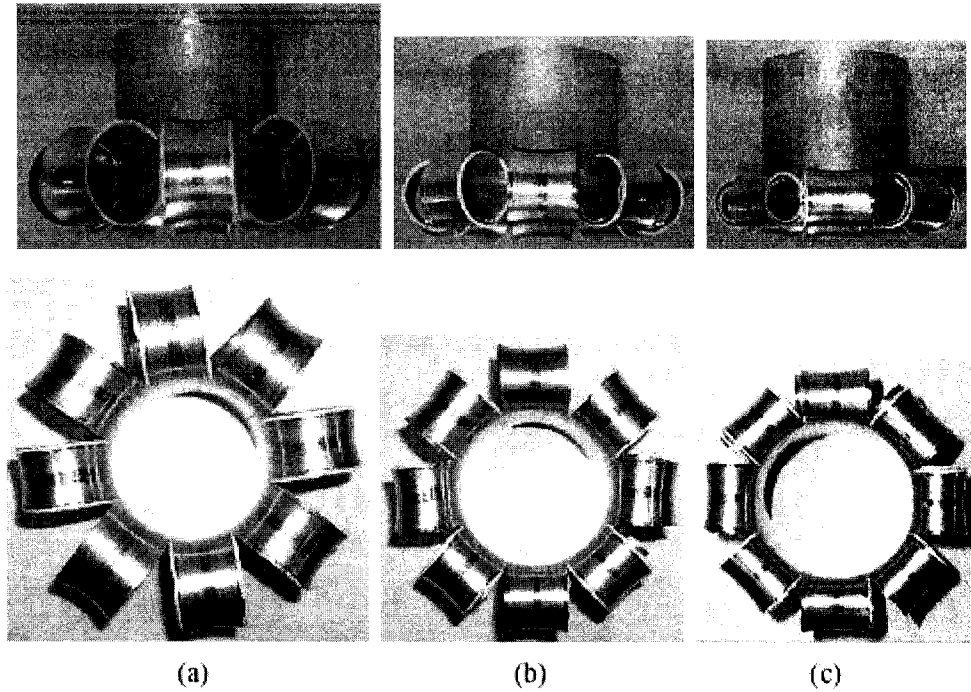


Figure 2.15. Photographs of typical aluminum specimens (with $D = 77.9$ mm; $t = 1.9$ mm) after tests: from left to right $\alpha = 45^\circ$, $\alpha = 60^\circ$ and $\alpha = 75^\circ$ [19].

Huang et al. [20] also investigated the energy absorbing behaviour of axially splitting square metal tubes. Tubes of 50 mm square with a variable thickness were pushed slowly against rigid pyramid shaped dies, which had various semi-angles. By pre-cutting 5 mm long slits at the four corners, the tube splits along the corners and curls outward with a certain radius at a constant force. Typical force–displacement plots for three different cases are shown in Figure 2.16. The corresponding specimens after testing are shown in Figure 2.17.

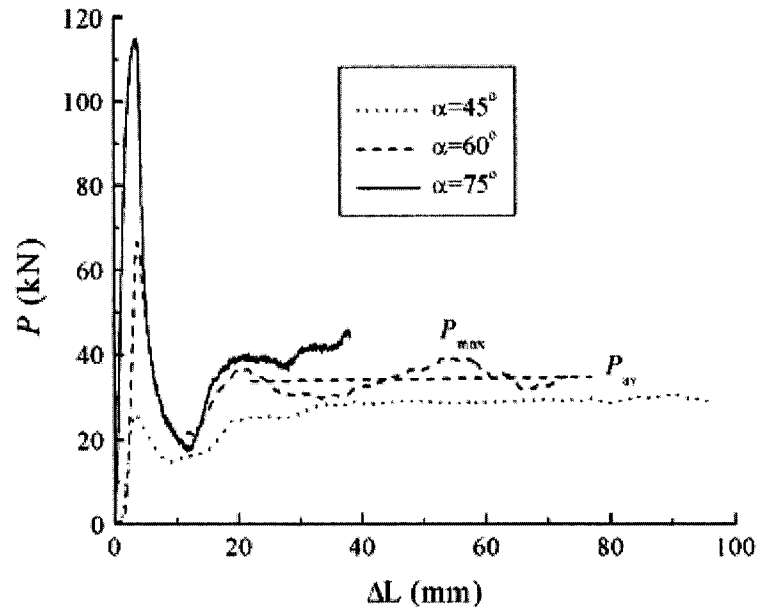


Figure 2.16. Typical force–displacement traces for mild steel square tubes with $t = 2.5$ mm against dies with semi-angle $\alpha = 45^\circ$, 60° and 75° , respectively [20].

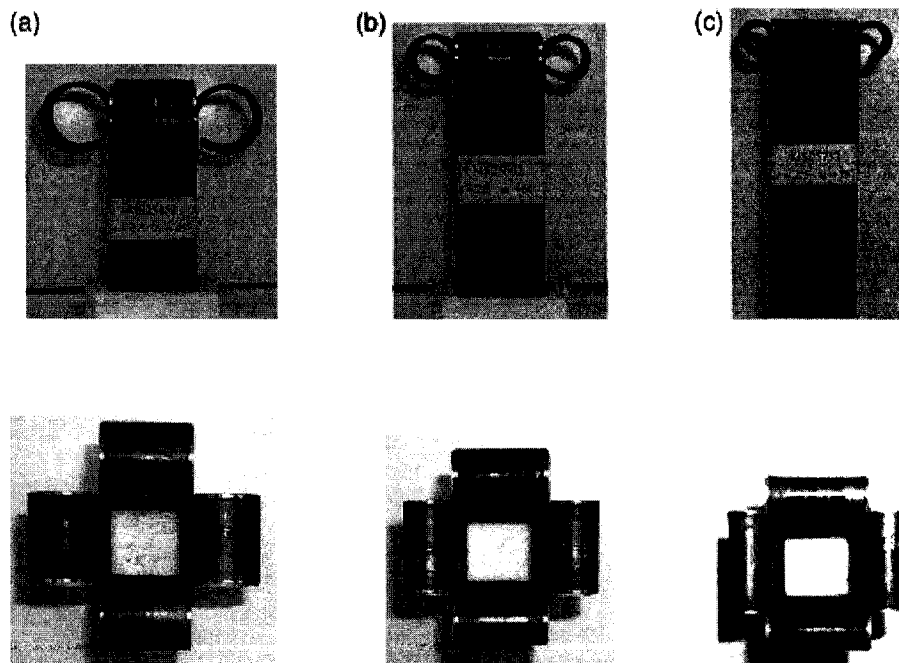


Figure 2.17. Photographs of typical specimens after tests [20].

2.1.4 Interactive Modes of Deformation

A significant amount of work has been done in the investigation of interactive modes of deformation. Reid et al. [25], Abramowicz and Wierzbicki [26], Reddy and Wall [27], have investigated foam-filled circular or square tubes under axial crushing. Reddy and Al-Hassani [28] have investigated axial crushing of wood-filled square metal tubes. Reid [29] presented load–displacement curves for central transverse loading of tubes filled with sand.

Hanssen, Hopperstad and Langseth [30] investigated the crash performances of aluminum foam filled circular and square cross-section tubes in axial compression. Quasi-static and dynamic experimental test showed that the aluminum foam had the effect of increasing the stiffness of the tube wall, resulting in an increased buckling load and higher energy absorption of the structure. As shown in Figure 2.18, foam filled tube had a higher number of sidewall lobes than the tube without foam. The increased number of lobes means higher efficiency in energy absorption. The foam filler provides internal support to the wall that reduces the buckling length of the sidewall resulting in an increased buckling load compared to the tube without foam filler. [30-32]

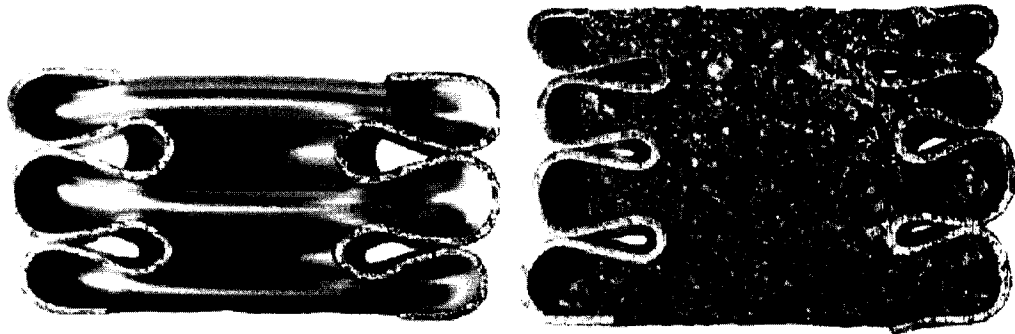


Figure 2.18. Non-filled and filled square tubes under quasi-static compression [30].

The summation of individual energies of crushing the foam and the tube alone does not equal that of the foam-tube assembly [30]. The difference between the two is known as the ‘interaction effect’. The addition of the foam to the tube results in

additional energy absorbing ability due to the deformation of the tube wall interacting with the foam core and is illustrated in Figure 2.19.

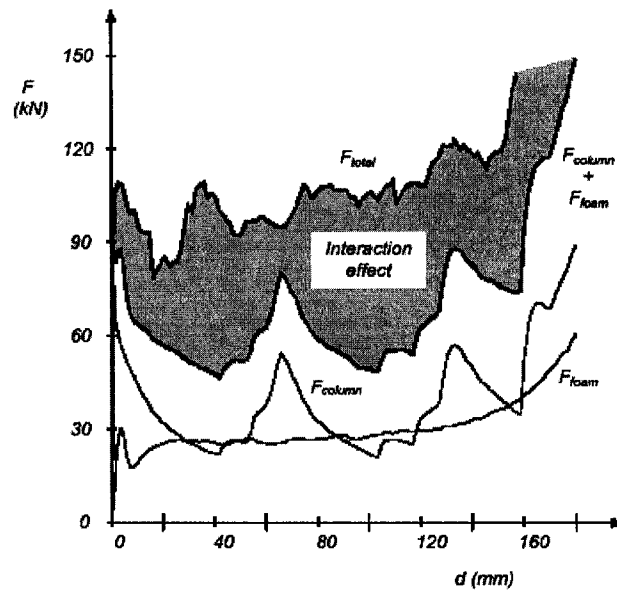


Figure 2.19. Force versus displacement curve for compression of tube and foam [30].

Langseth, Hopperstad and Hanssen [33] reported that the energy absorbing capacity of aluminum foam was related to the foam density under axial compression. Through experimental quasi-static compression testing of square cross-section tubes, they found that as foam density increased the specific force required to crush the test specimens increased and the force versus displacement curve tended to be more stable.

2.1.5 Deformation Mode of Aluminum Foam Filled Braided Tube under Tensile Loading Conditions

This part of literature review is related to energy absorption structural members which function under tensile loading conditions. Energy absorbing devices are needed in tensile loading conditions as in automobile side impact and in space frame structures, where a structure is subjected to tensile loading. Under a tensile loading condition, traditional metallic structures tend to deform locally, which results in very low efficiency energy absorption. The application of metallic or polymeric foam to enhance the energy

absorption capabilities of a new class of braided tubes under tensile loading results in a very efficient energy absorption device [5]. Harte et al. [34] have researched the energy absorption of polymeric foam filled circular braided composite tubes both experimentally and theoretically. In Harte's research, it was found that foam-filled braided circular tubes exhibited promising energy absorbing characteristics due to a combination of energy absorption by the polymeric foam core and by the composite braided tube. The energy absorbing process included two distinct phases. In the first phase, scissoring of the braided tube tows under tensile loading caused the epoxy matrix to crack resulting in energy absorption. The delocalized cracking of the matrix was dependent on the correct selection of matrix material and tow fiber material. Crushing of the foam core, caused by the decrease in the diameter of the braided tube as it elongated, resulted in further energy absorption and was defined as the second phase. The energy absorption after tow lock-up was not investigated in Harte's research. Geometry of braided tube is shown in Figure 2.20, while testing results in terms of stress strain curve is shown in Figure 2.21.

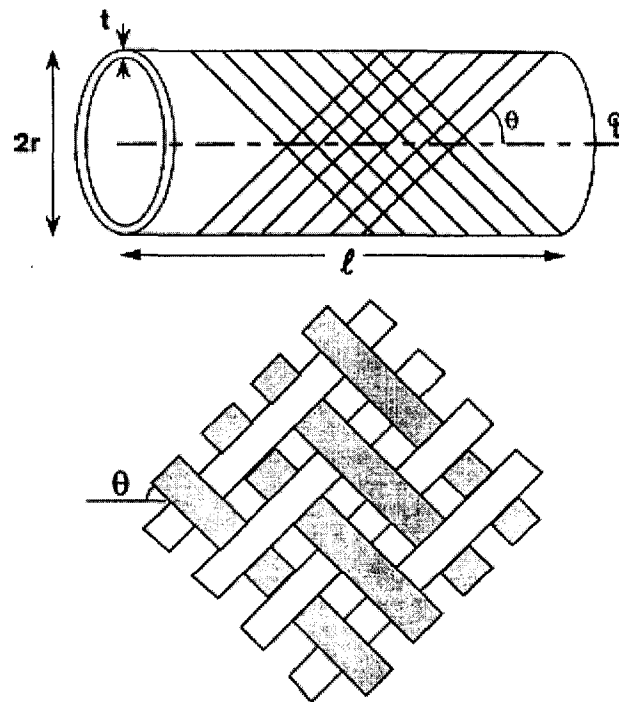


Figure 2.20. Geometry of a braided tube in reference [34].

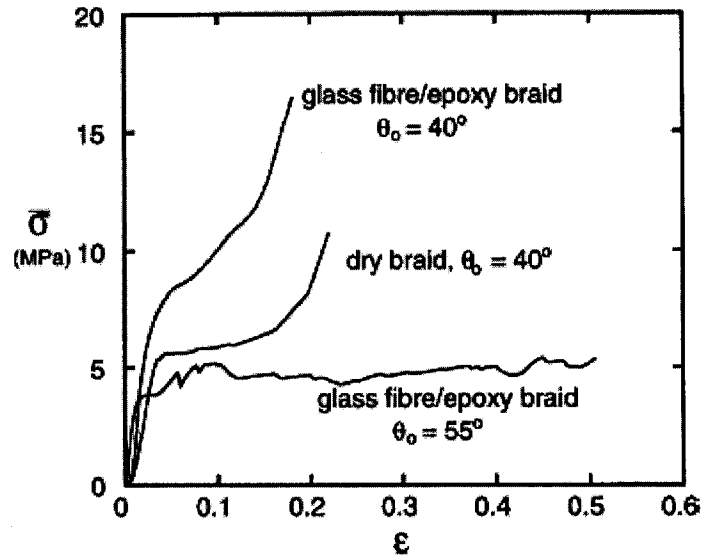


Figure 2.21. Tensile stress versus strain curve for three braids with polyurethane foam cores in reference [34].

Unlike Harte's treatment of assuming the braided tube as a rigid-ideally plastic solid, Cox et al. [35, 36] have investigated the influence of steel chain geometry and matrix materials (including an aluminum/magnesium alloy, epoxy, polycarbonate, and a lead/tin alloy) on the energy absorption capacity of knitted chain composites. Chain composites were geometrically configured to delocalized damage under tensile loading. The chains and fiber tows were positioned in the manufacturing process to ensure that they were not in direct contact with each other. Only after cracking of the matrix material, did individual chains or tows come into contact with each other. Energy absorption capacity, for the knitted chain composites, per unit volume and per unit mass were experimentally observed to be approximately 55 MJ/m^3 or 14 J/g respectively and is significantly dependent upon the matrix material. Geometry of chain composite is shown in Figure 2.22. A stress/strain relationship of the chain composite under tensile loading is shown in Figure 2.23.

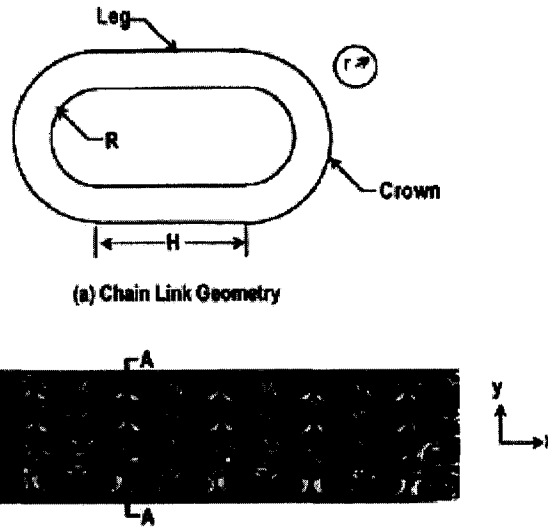


Figure 2.22. (a) Geometry of a standard chain link (a racetrack link). (b) Contracted chain configuration used in composites [35].

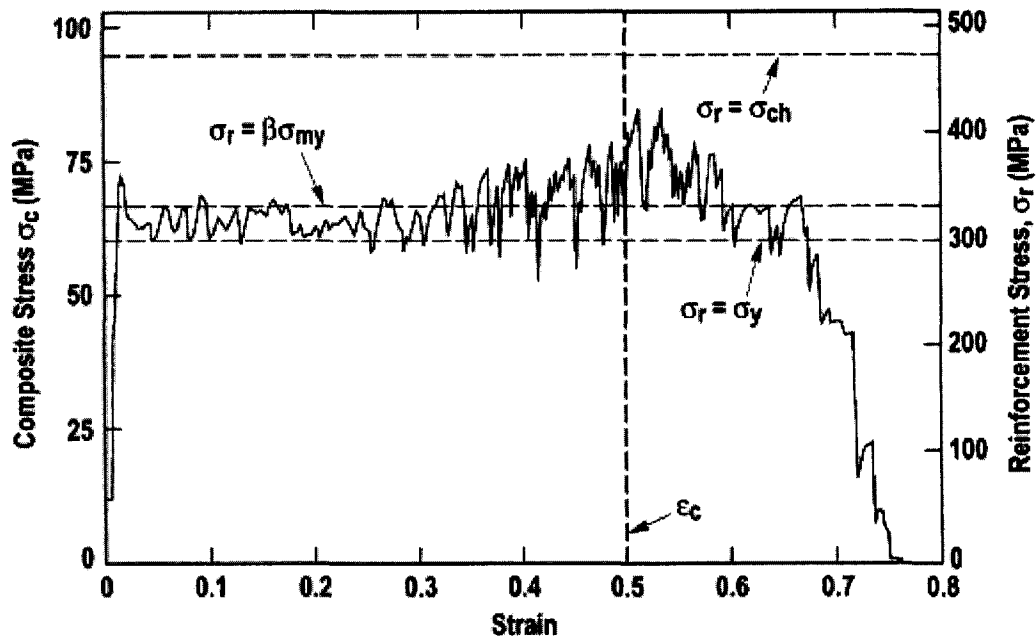


Figure 2.23. Stress strain record for small-link chain-polycarbonate composite [36].

Altenhof et al. [5] has experimentally investigated the deformation behaviour of metallic foam filled braided tubes and has observed three distinct regions of deformation which have been related to the kinematic displacement constraints of the braided tube and the material properties of the aluminum foam and the stainless steel braided tube.

Experimental observations from reference [5] have indicated that the mechanical response of the foam filled braided tube is dependent upon the density and geometry of the aluminum foam core and the geometry of the braided stainless steel tube. An aluminum foam filled braided stainless steel tube is shown in Figure 2.24.

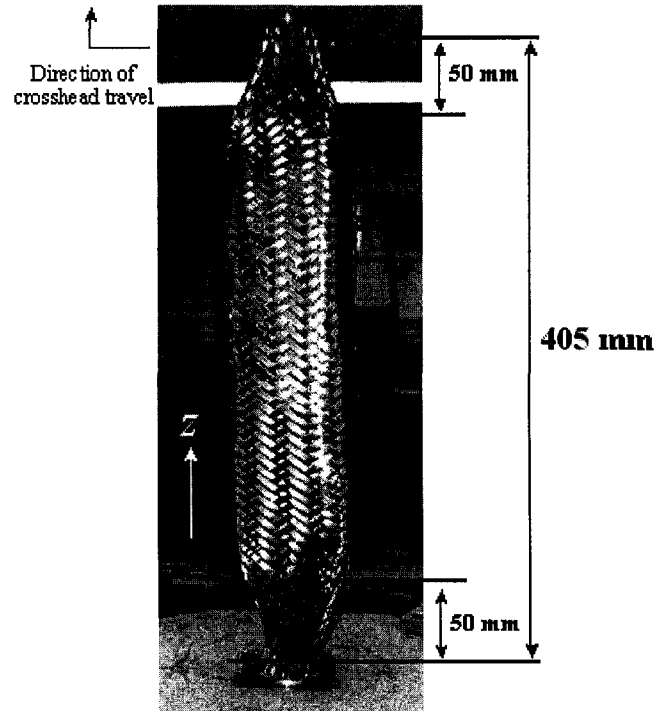


Figure 2.24. Aluminum foam filled braided tube secured into the tensile testing machine prior to loading [5].

2.2 Factors That Influence Collapse Mode

2.2.1 Cross Section Geometry

It is recognized that the number of “angle” elements on a tube’s cross-section decides, to a large extent, on the efficiency of the energy absorption [37, 38]. It is therefore desirable to design thin walled sheet metal profiles or extrusion with internal webs for weight-efficient energy absorption.

Kim [39] has proposed two new multi-cell cross sections as shown in Figure 2.25. The columns were made of an aluminum extrusion AA 6063-T7 with the mechanical properties of Young’s modulus $E= 69$ GPa, initial yield stress $\sigma_y= 86.94$ MPa, and Poisson’s ratio $\nu= 0.3$.

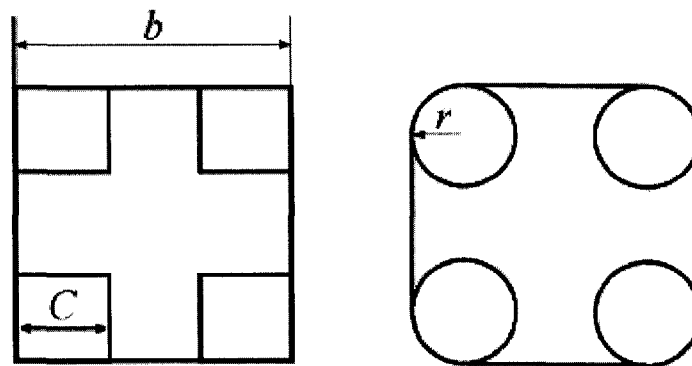


Figure 2.25. Proposed cross-sections in reference [39].

Numerical simulations of both cross-sections in Figure 2.26 were made for $b = 40$ mm, $C = 20$ mm and $r = 10$ mm cases. The uniform thickness over the entire cross-section, $t = 2$ mm is used. The deformed shapes are shown in Figure 2.26, and the crushing forces are compared in Figure 2.27. The deformation mode is governed by the square or circular element on the corner part, so that the very short folding wavelength is observed for both cases and the side flanges act as the stabilizer between each corner element.

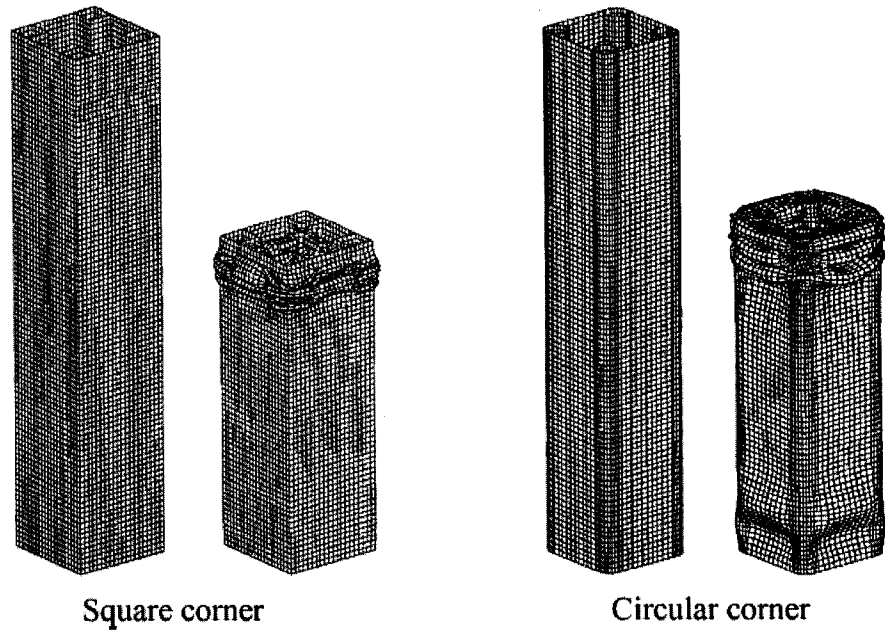


Figure 2.26. Deformed shapes in reference [39].

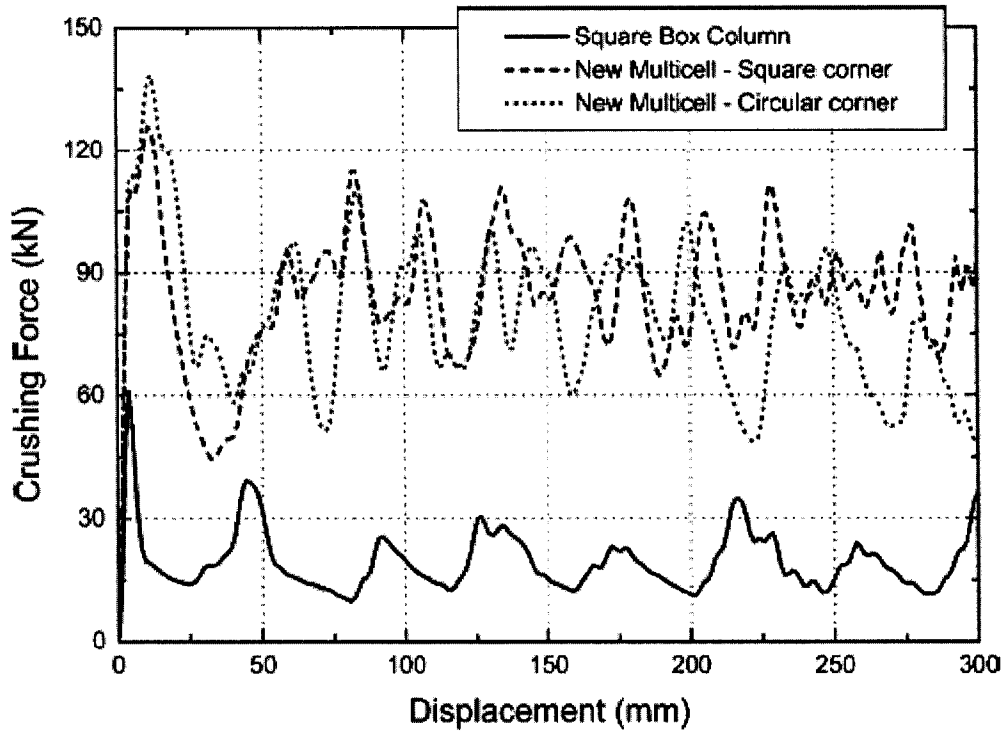


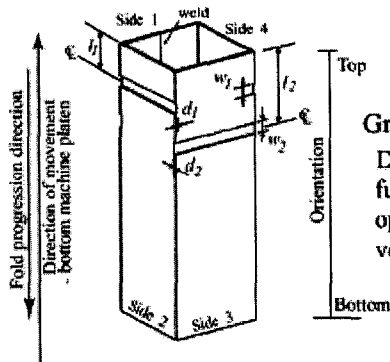
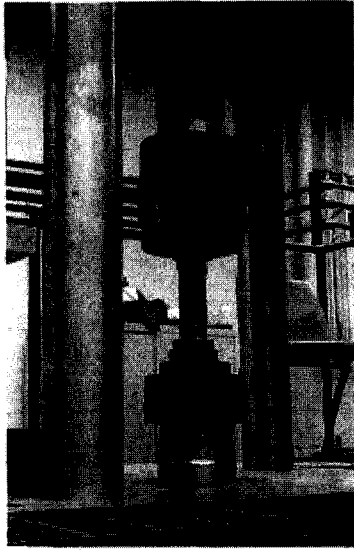
Figure 2.27. Crushing forces displacement curve in reference [39].

2.2.2 Extrusion Materials

Axial collapse behaviours of tubular structures have been investigated with respect to many types of materials. Studies have been performed on circular/square tubes of aluminum alloys, stainless steel, mild steel, low and high strength steel [40]. Dipaolo [40] has experimentally investigated the quasi-static, symmetric axial crush response mode of commercially produced, welded AISI 304 stainless steel square box components by using control techniques such as tube end constraints and collapse initiators. He also investigated the effect of alloy composition and microstructure on the axial crush configuration response. The test specimens used in the investigation were fabricated from AISI 304 austenitic stainless steel. The cross-sections of the tubes had square box-type geometry with rounded corners. Dimensions included nominal 50 mm by 50 mm outside dimensions, a 1.6 mm wall thickness, and an average corner inside radius of 3.6 mm. The material yield stress was 330 MPa, and the ultimate tensile strength was 570 MPa.

It was found by Dipaolo [40] that the structural response can be restricted to a specific axial crush configuration mode and therefore, a controlled and repeatable energy absorption process can be obtained and that higher concentration of carbon and smaller grain size resulted in an 18% increase in energy absorption.

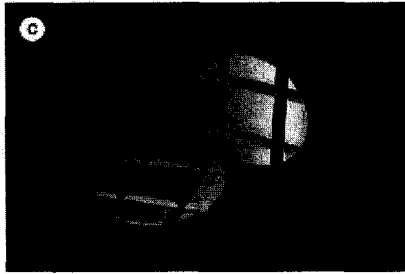
Experimental set up, tube end side constraints and crash initiator geometry are illustrated in Figure 2.28. Photograph illustrating a deformed specimen and load displacement curve are shown in Figure 2.29.



Groove design:
 Double set of machined full width grooves in opposite sidewalls with vertical offset

Groove dimensions:

	Upper set - "set 1"		Lower set - "set 2"	
	S1	S3	S1	S3
width (mm)	w_1	6.4	w_2	6.4
depth (mm)	d_1	0.23	d_2	0.18
distance from top end of tube (mm)	l_1	21.6	l_2	44.5



QUASI-STATIC TESTING

- MTS universal testing machine
- 1350 kN capacity
- cross-head speed = 2.5 mm/min
- displacement control
- Temperature - 20°C

(a)

Figure 2.28. Experimental test set-up and controls: (a) test machine set-up; (b) collapse initiator geometry and (c) grooved end cap set for tube end constraints [40].

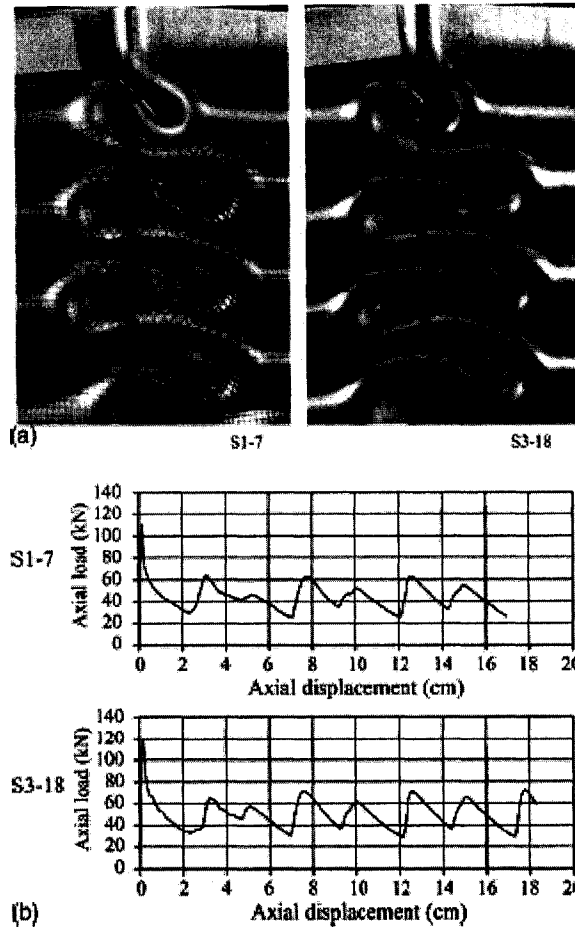


Figure 2.29. Experimental tests results: (a) fold formations and (b) load–displacement curves [40].

Advanced High-Strength Steels (AHSS) have been recently developed by steel companies to meet the requirements of automotive company to reduce the vehicle weight while maintaining its strength [2]. AHSS is relatively new to the materials world, but its application in automotive structures has been increasing recently since the steel industry's UltraLight Steel Auto Body (ULSAB), UltraLight Steel Auto Closures (ULSAC) and ULSAB-AVC (UltraLight Steel Auto Body - Advanced Vehicle Concepts) programs have successfully demonstrated its weight-saving and performance improvement qualities. Based on mechanical properties, High-Strength Steels (HSS) are defined as those steels with tensile strengths from 270–700 MPa. Ultra-High-Strength Steels (UHSS) are defined as steels with tensile strengths greater than 700 MPa. Four types of AHSS steels currently in worldwide production are: Dual Phase (DP), Transformation

Induced Plasticity (TRIP), Complex Phase (CP), and Martensite (Mart). Figure 2.30 shows the Strength-Elongation relationships for low strength, conventional HSS, and advanced HSS steels.

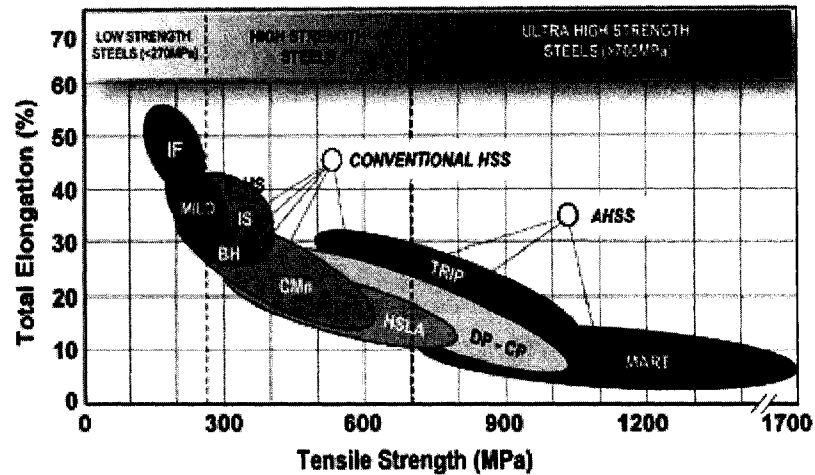


Figure 2.30. Strength-Elongation relationships for low strength, conventional HSS, and Advanced HSS steels [2].

ULSAB-AVC vehicle concepts were subjected to and successfully passed the most severe crash simulations, encompassing seven different events that represented the New Car Assessment Program (NCAP) requirements anticipated by the year 2004. Two steel longitudinal rails are the backbone of the entire under body and integral crash load-carrying structures for frontal crash energy management. These structures are hydroformed, tailored tubes made of Dual Phase (DP) steel. Figure 2.31 shows a Mercedes A-Class body structure. The proportion of high-strength and advanced high-strength steel alloys comprised 67 per cent of its total material usage [2].

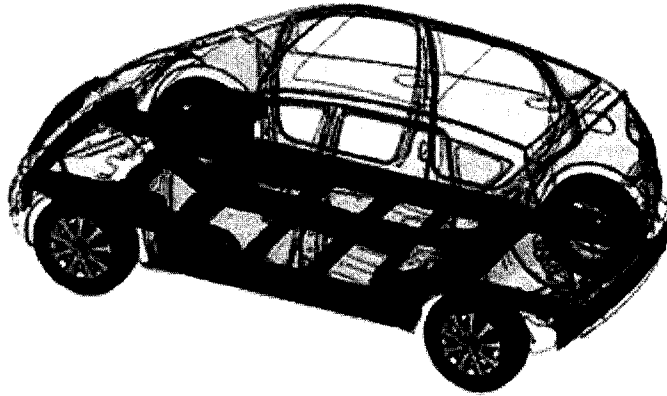


Figure 2.31. Mercedes A-Class body structure [2].

Link and Grimm [41] have experimentally studied crash energy absorption characteristics of steel tubes with different strengths and thicknesses. Figure 2.32 shows the force displacement curve of steel tube made from TRIP 590 Steel with a diameter of 70mm and a wall thickness of 1.61 mm during a drop tower crash tests. Figure 2.33 shows the comparison of force displacement curves of steel tube specimens made from different materials.

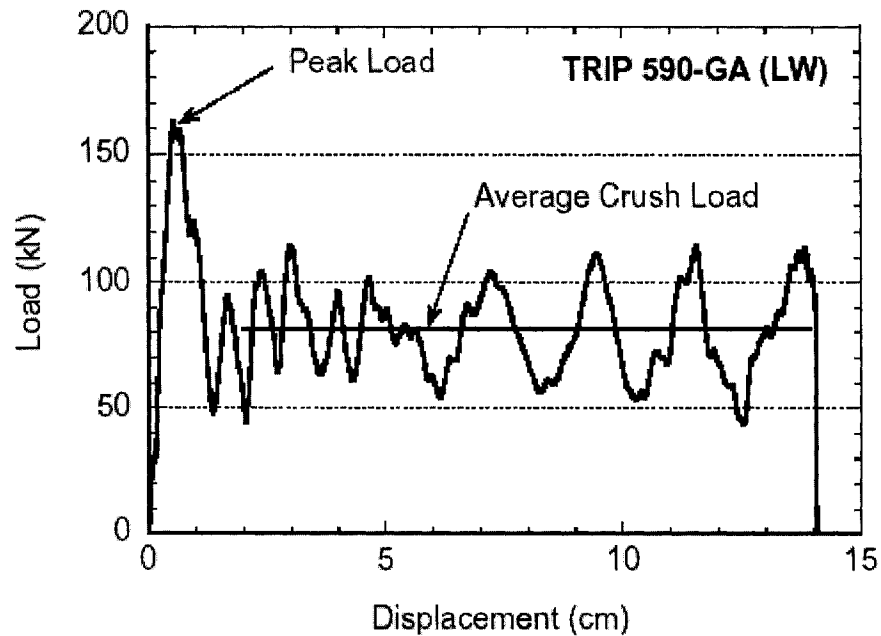


Figure 2.32. Force displacement relationship of TRIP 590 Steel tube during drop tower crash test: diameter: 70 mm, wall thickness $t=1.61$ mm [41].

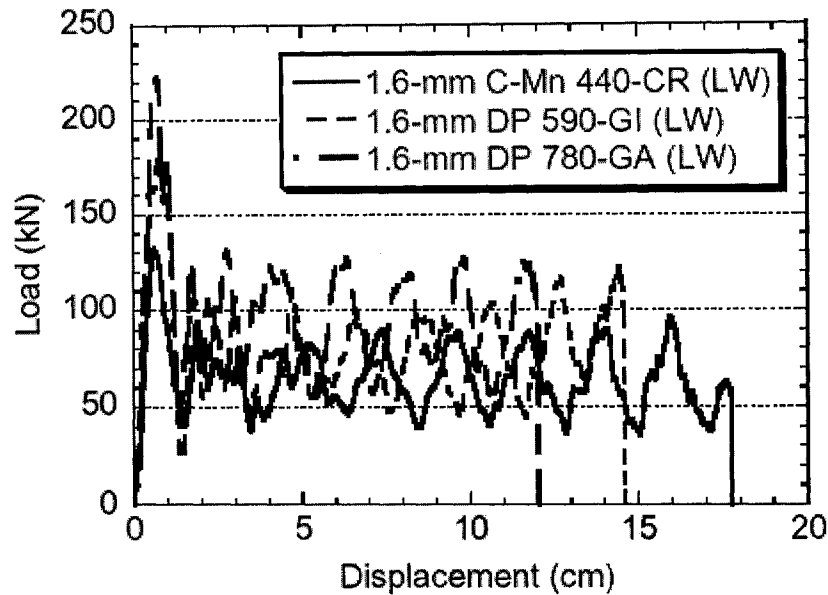


Figure 2.33. Force displacement curve of specimens made from different materials [41].

2.2.3 Geometrical Dimensions

Geometrical dimensions of length, width/diameter, and thickness of the tubular structure and its relationship between each other play a very important role in determining deformation pattern of axial buckling mode. Abramowicz and Jones [14] have studied the role of geometric parameters of mild steel square/circular cross section tubes in determining whether a tube will collapse in the global bending mode or in the progressive buckling mode. A total of 128 thin-walled mild steel columns with a wide range of lengths, widths, and wall thickness were quasi-statically crushed in order to determine their collapse modes. There are six different cross sections ($5.5 \leq C/t \leq 38$) for square tubes and five different cross sections ($9.6 \leq 2R/t \leq 48$) for circular tubes.

The experimental results are summarized in Figure 2.34 in terms of the dimensionless parameters L/C and C/t , where L is the length of the tube, C is the width of the sides, and t is the wall thickness. The solid line in the figure approximately separates the experimentally determined progressive buckling and global bending regions (i.e. regions above the line represent geometries of tubes that collapse in the global bending

mode and regions below the line represent geometries of tubes that collapse in the progressive buckling mode).

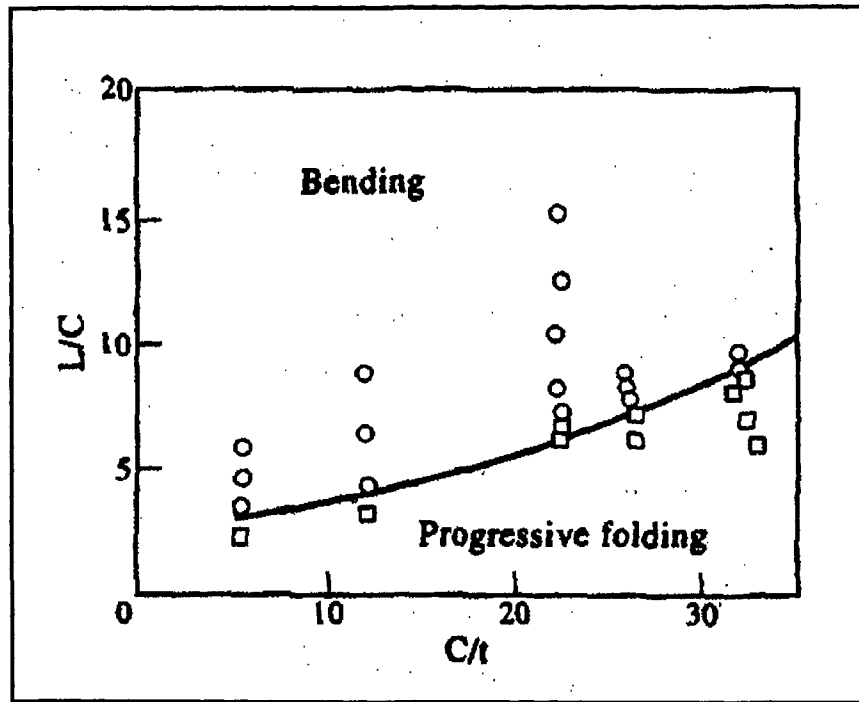


Figure 2.34. Experimental results from Abramowicz and Jones [14].

It was also noted in reference [14] that an accurate description of the transition process was difficult since it required a detailed knowledge on the formation of a plastic mechanism as well as a precise distribution of the stresses in a column cross section. Although a complete solution to this problem was not available, a simplified model of a collapsing column was used to develop the following theoretical relation for the transition boundary between the global bending mode and the progressive collapse mode for plastic buckling of square tubes as a function of C/t :

$$\left(\frac{L}{C}\right)_{cr} = 2 \frac{\left(\frac{C}{t}\right)^{\frac{1}{3}}}{1 - 2.88 \left(\frac{C}{t}\right)^{\frac{4}{3}}} \quad (2.1)$$

Equation (2.1) is plotted in Figure 2.35 along with equation (2.2), which is an empirical equation describing the transition boundary between the global bending mode and the progressive collapse mode for plastic buckling of square tubes as a function of C/t . Equation (2.2) was obtained by a curve fit method.

$$\left(\frac{L}{C}\right)_{cr} = 2.482 \cdot \exp\left(0.0409 \frac{C}{t}\right) \quad (2.2)$$

Langseth and Hanssen [42], who have done extensive research on the axial crushing of aluminum extrusions, suggest a critical length to width ratio of 3 for a stable (progressive buckling) collapse mode. For small width-to-thickness ratios, this value is in reasonable agreement with the experimental and theoretical results illustrated in Figure 2.36.

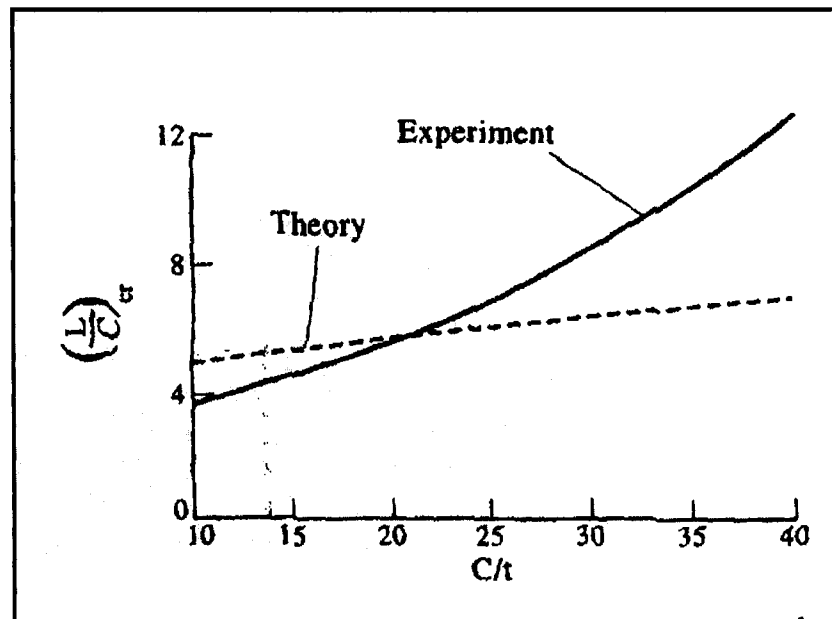


Figure 2.35. Empirical and theoretical transition lines found by Abramowicz et al [14].

2.3 Crush Initiators

Crush initiators, sometimes called triggers, stress concentrators, imperfections, or geometrical discontinuities by different authors in different literatures, is a deformation control technology which can be used to initiate a specific axial collapse mode, stabilize the collapse process and minimize variations in crash mode due to imperfections in materials, part geometry, manufacturing, and assembly processes etc. For axial crush deformation, the use of crush initiator can reduce the peak buckling load, improve crush characteristic parameters and trigger deformation at a specific location. Initiators can be obtained by either material properties changes or geometric modifications to the structure. Examples of material property changed initiators are locally heat treated regions at desired locations. Geometric initiators can be obtained by mechanical methods of structural additions or deletions on the component. Geometric initiators can be easily controlled by the change of location, shape, dimension and quantity.

The naturally-formed initiators involve pre-buckling of the component past the peak load. Quasi-static pre-buckling or pre-crushing of a specimen has been performed to eliminate initial peak load on honeycomb specimens and to control behavior of square tubes as mentioned in reference [40]. More commonly used mechanically-induced initiators such as local transverse indentations, circular holes, or crimping have been used on tubes for collapse mode control and peak load reduction. Circular corner cut-outs on square tube specimens have been employed by Abah et al. [43] to initiate collapse and reduce the peak load. Abah et al. considered tubes with a length of 200 mm, width of 48 mm and a thickness of 1 mm. A diameter range of 2 mm to 12 mm of initiators was considered in the research. It was found by Abah et al. that the hole initiators caused a peak buckling load decrease proportional to increasing initiator size, while the mean crushing load remained relatively constant.

Holes in circular cylindrical tubes have been drilled to set the collapse initiation site, reduce the peak load, and alter the deformation mode by Gupta et al. [44]. Combinations of transverse sidewall indentations and holes in square tube specimens without end constraints have been studied to control the peak load magnitude and stability of the collapse mode by Marshall and Nurick [45].

Krauss [46] studied the effect of different geometric discontinuities on reducing peak buckling loads and promoting a stable collapse mode. Krauss introduced circular and diamond shaped holes in square steel tubes subjected to dynamic axial loading. The geometry of the initiators is illustrated in Figure 2.36.

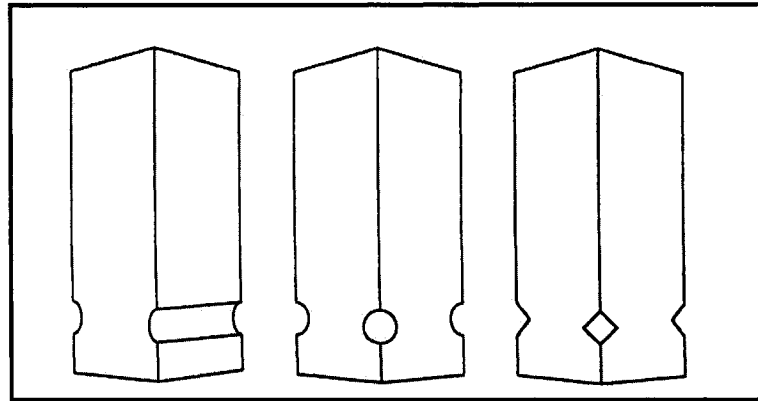


Figure 2.36. Initiator geometry configurations studied by Krauss [46].

It was found by Krauss that each type of initiator effectively reduced the peak buckling load. The numerically obtained load versus displacement curves for each size of circular hole initiator as well as the specimen with no initiator are shown in Figure 2.37. For the circular and diamond shaped notches, the peak buckling load decreased as the size of the initiator increased.

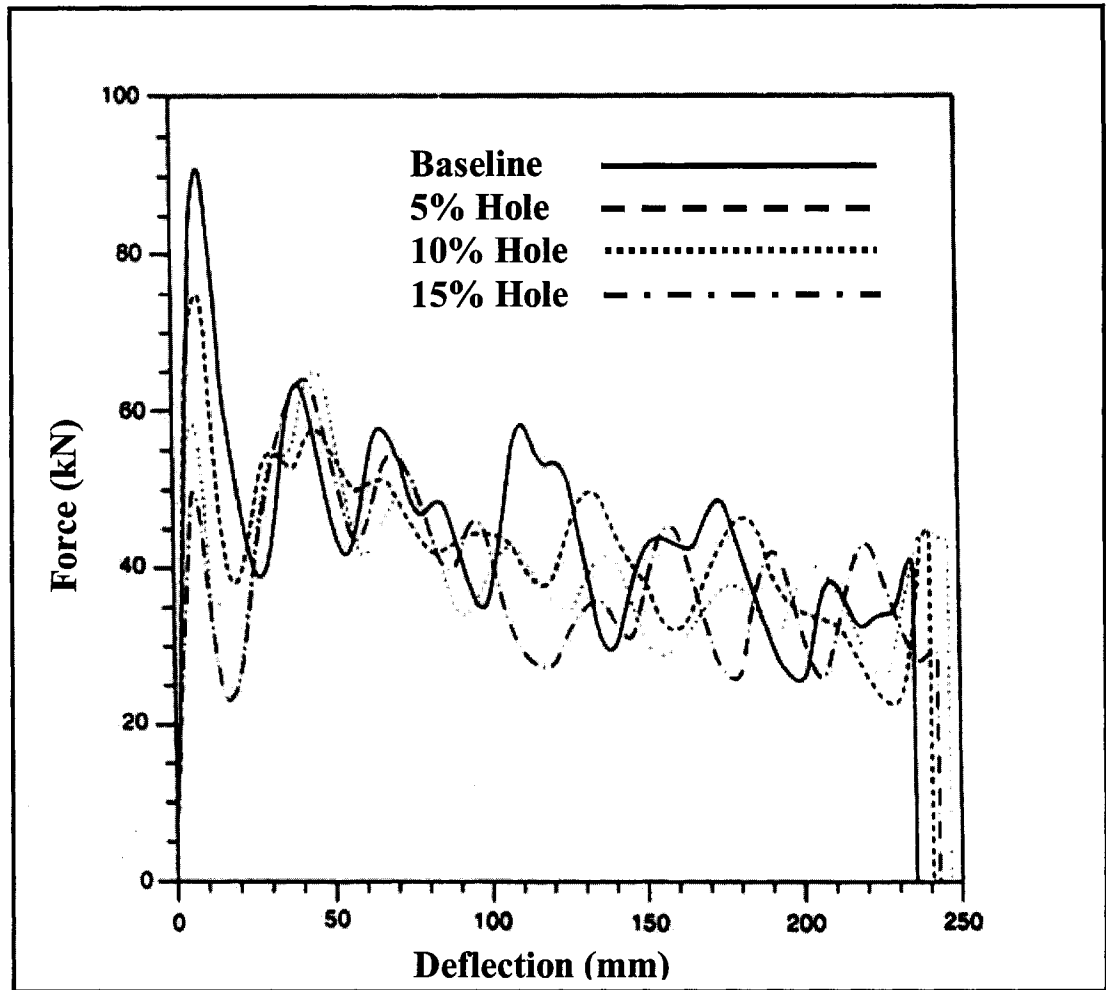


Figure 2.37. Numerically calculated force versus deflection curves for specimens with each size of circular crush initiator studied by Krauss [46].

Lee [47] has also studied the effect of crush initiators on the energy absorption of axially loaded square tubes. Lee introduced rows of grooves into dynamically loaded aluminum tube extrusions. The energy absorption performance of the tubes was then evaluated by conducting quasi-static crushing tests on a 10-ton Instron compressive testing machine using a crosshead speed of 20mm/min. FE simulations were also conducted using the FE simulation program PAM-CRASH. The groove geometries considered are illustrated in Figure 2.38. Two types of grooves, referred to as the full dent and the half dent, were used as initiators in the study. As illustrated in Figure 2.38, the grooves are 1mm deep and 2mm wide and extend across either the full side width of the tube or half the side width.

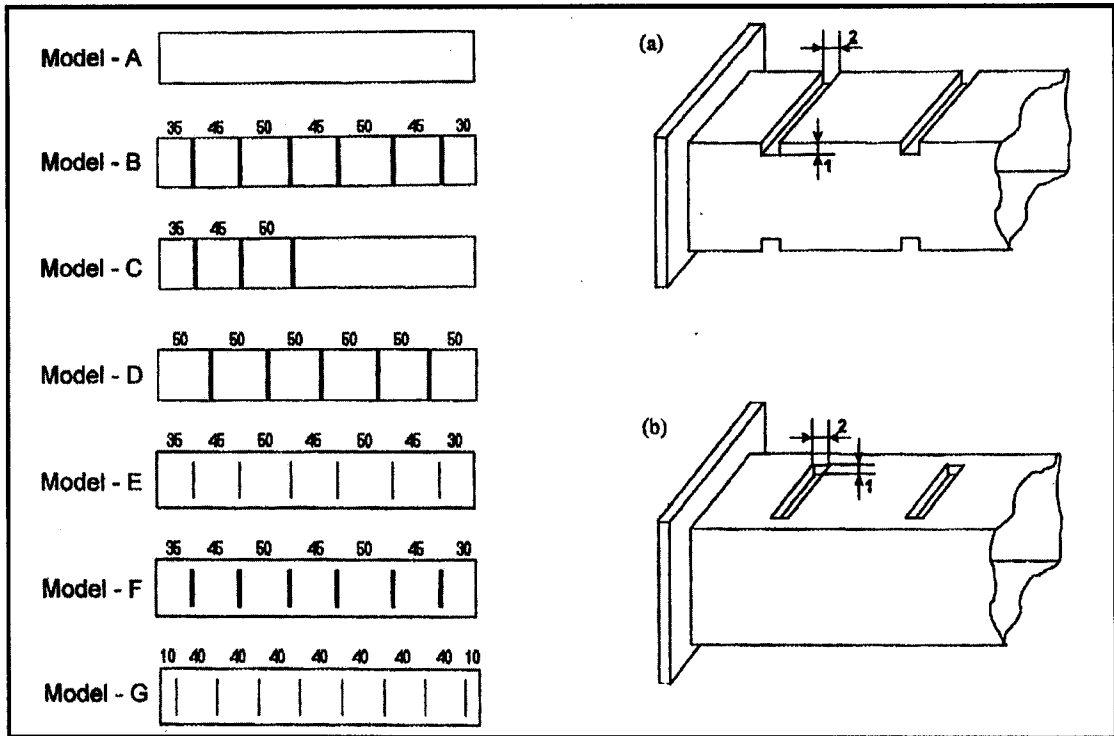


Figure 2.38. Geometry and configurations of dents considered by Lee [47]. All dimensions are in millimeters.

The configurations of the grooves considered by Lee are also illustrated in Figure 2.38. Six dent configurations are considered, plus one baseline tube with no dents. The dent configurations of models B, C, E and F are based on the predicted or pre-estimated folding sites and the dent configurations of models D and G are spaced at even intervals at locations that do not correspond to the natural folding sites. The results showed that the tubes with dent configurations corresponding to the pre-estimated folding sites collapsed in the same mode as the baseline model (symmetric), while decreasing the peak buckling load and the subsequent peak loads corresponding to each fold formed. However, the models with dent locations not corresponding to pre-estimated folding sites exhibited a non-uniform crushing mode accompanied by global bending.

Bjorneklett and Myhr [48] studied the application of localized heat treatment of energy absorption components. The heat treatment method enabled local modification of yield strength and ductility in order to guide plastic deformation. Figure 2.39 shows the locally heat treated specimen. Figure 2.40 shows the changed yield stress of specimen and Figure 2.41 shows the test results.

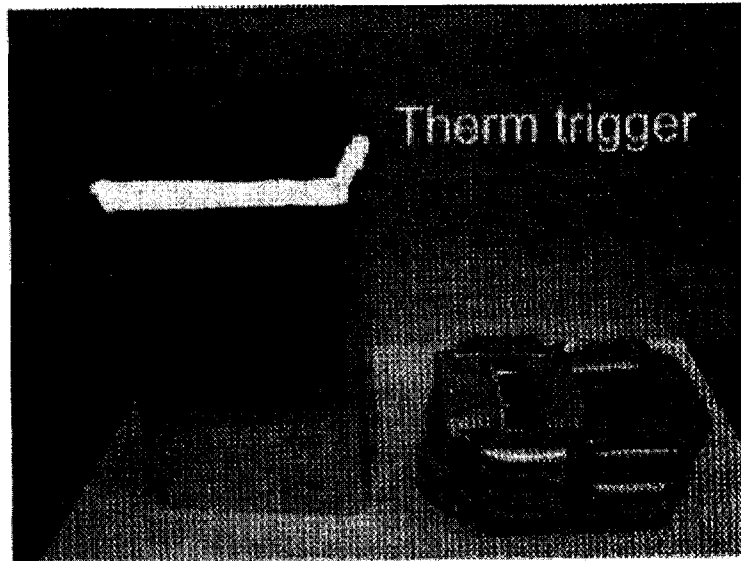


Figure 2.39. The initial box is to the left. The drawn line indicates the location of the thermal trigger. On the right side the box is shown after approximately 130 mm of axial compression [48]. Reprinted with permission from SAE paper number 2003-01-2794 (c) 2003 Society of Automotive Engineers, Inc.

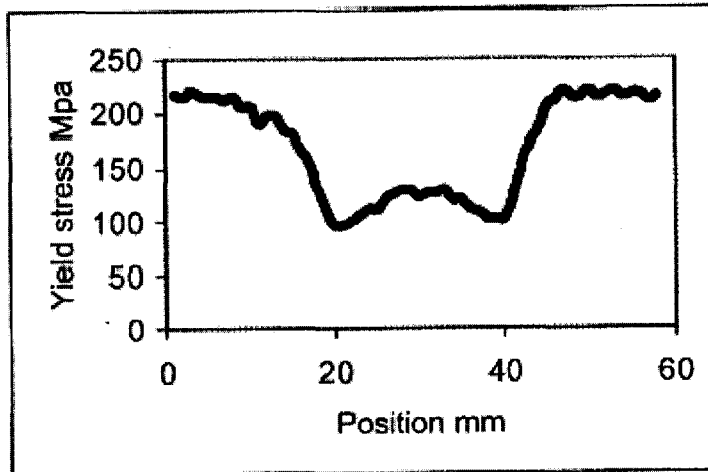


Figure 2.40. Yield stress values across a thermal trigger. The base material yield stress is about 220 MPa while yield stress within the 20 mm wide region representing the trigger is reduced to about 100-125 MPa [48]. Reprinted with permission from SAE paper number 2003-01-2794 (c) 2003 Society of Automotive Engineers, Inc.

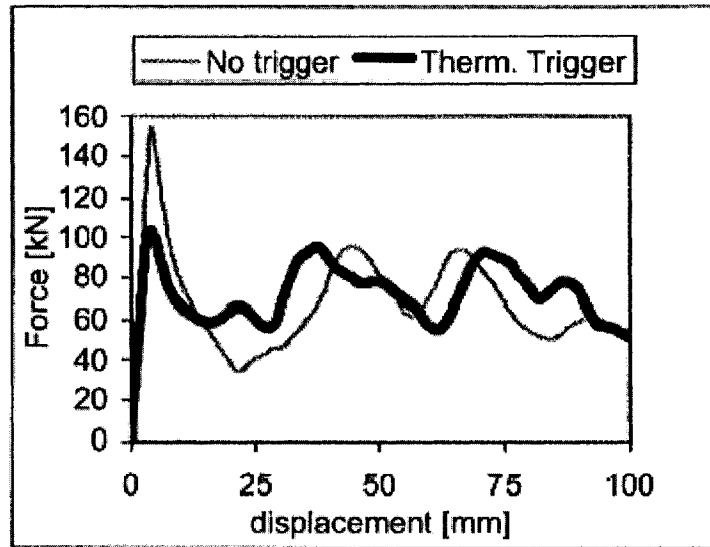


Figure 2.41. Fat line shows force displacement from a box having thermal triggers while thin lines show results from three boxes without triggers. The absorbed energy i.e. the integral under the curves is about the same in both experiments [48]. Reprinted with permission from SAE paper number 2003-01-2794 (c) 2003 Society of Automotive Engineers, Inc.

Chen et al. [49] have experimentally and numerically investigated trigger hole shape and size sensitivity using a production vehicle front rail, while lab produced crash columns using thinner gauge dual phase (DP) steel with a minimum ultimate tensile strength of 600 MPa (DP600) were utilized to study the trigger hole location sensitivity. As shown in Figure 2.42, the total rail tip length is 480 mm, five rectangular trigger holes with dimension of 8×13 mm were located at every corner of the rail assembly. The distance from the front end to the first hole and between the holes in the middle were 43 mm, 51 mm, 75 mm, 47 mm, and 43 mm, respectively. In addition to the rectangular trigger holes, five other shapes of the holes shown in Figure 2.43 were applied at the same locations. The material used for the front rail tip is 3.90 mm High Strength Low Alloy (HSLA) steel with minimum yield strength of 280 MPa.

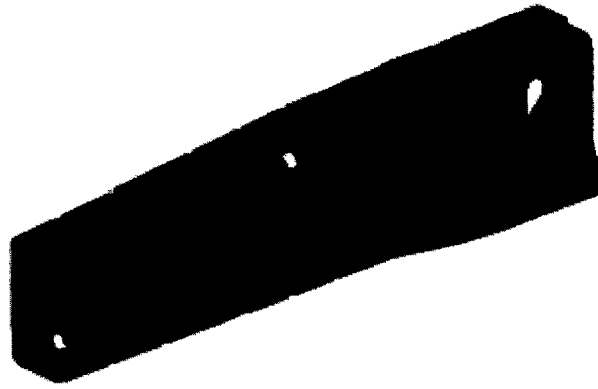
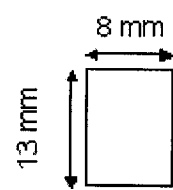
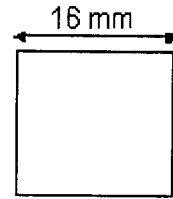


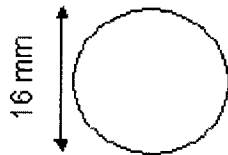
Figure 2.42. Front rail tip with rectangular trigger holes at the corners [49]. Reprinted with permission from SAE paper number 2005-01-0355 (c) 2005 Society of Automotive Engineers, Inc.



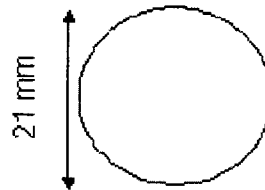
Rectangle - baseline



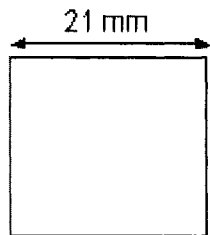
Square - 16 mm



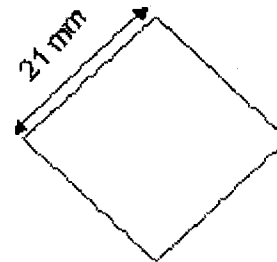
Circle - 16 mm



Circle - 21 mm



Square - 21 mm



Diamond - 21 mm

Figure 2.43. Trigger hole shapes and size [49]. Reprinted with permission from SAE paper number 2005-01-0355 (c) 2005 Society of Automotive Engineers, Inc.

Experimental tests showed that the crash characteristics in terms of average crash forces and peak buckling loads were not sensitive to the trigger shapes. At the same trigger hole size, the crash results, for example, from 16 mm square and circle or 21 mm square, circle and diamond, are at the similar level. However, when the trigger size increases, the rail becomes softer which results in greater crash distance, lower average crash force and lower first peak load. It is also shown in Figure 2.44 that the first peak load is relatively more sensitive to the trigger hole size. DP600 is less sensitive to the trigger size than HSLA steel.

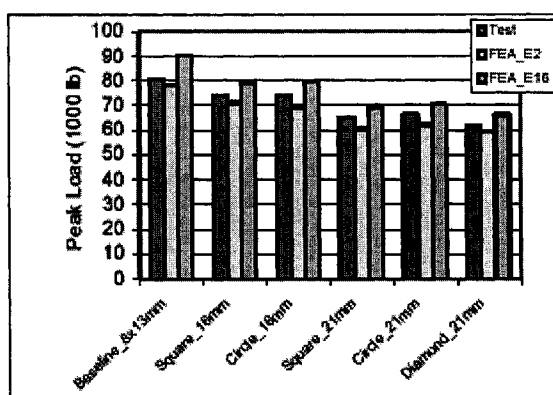
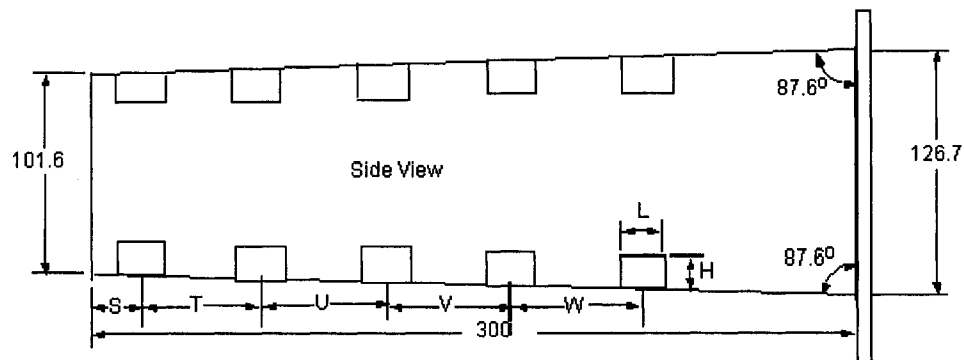


Figure 2.44. Peak buckling load [49]. Reprinted with permission from SAE paper number 2005-01-0355 (c) 2005 Society of Automotive Engineers, Inc.

Trigger hole location sensitivity was studied by using lab produced crash columns with 1.70 mm DP600 steel, as shown in Figure 2.45. The 300 mm long columns were longitudinally symmetric with rectangular cross-sections made of two U-channels continuously welded together. Rectangular trigger holes were placed at the corners of the columns at the locations specified in the table in Figure 2.45. Two hole sizes were tested, i.e. big hole at 12×8 mm and small hole at 6×8 mm, respectively. Part P24-78 has two rows of big holes, while part 24-78-120 has three rows of big holes with one more row added at 120 mm away from the second row. Part S33-50-60 has three rows of small holes, and part S27-37-35-60-60 has five rows of small holes.

Test results showed that the right combination of size, location, and the number of trigger holes was critical to have a controllable, stable and predictable crash mode.

Smaller or fewer trigger holes may produce more variations in real crash and the crash process was less controllable, stable and predictable.



Part ID #	S	T	U	V	W	L	H	Amount
P24-78	24	78	none	none	none	12	8	3
P24-78-120	24	78	120	none	none	12	8	3
S33-50-60	33	50	60	none	none	6	8	3
S27-37-35-60-60	27	37	35	60	60	6	8	3

Figure 2.45. Crash column geometry and trigger hole locations [49]. Reprinted with permission from SAE paper number 2005-01-0355 (c) 2005 Society of Automotive Engineers, Inc.

Arnold and Altenhof [12, 13] have experimentally and numerically investigated the deformation mode and energy absorption of AA6061 temper T4 and T6 with and without the presence of circular discontinuities. Under compressive axial loading, the structures under consideration had L/C and C/t ratios that resulted in a prediction of global bending collapse, according to theoretical and empirical predictions of reference [14]. In order to change the collapse mode of the structures from global bending to a mode that promotes greater energy absorption, centrally located circular holes were placed at two opposite side walls at the midpoint of the extrusion structures. It was expected that these circular hole discontinuities would act as crush initiators and have the effect of decreasing the peak buckling load and increasing energy absorption.

It has been found that collapse mode and energy absorption of the structure is sensitive to both material properties and the presence of geometrical discontinuities. The difference in material behaviour between AA6061 T4 and AA6061T6 determined the collapse modes of progressive buckling for tubes with a T4 heat treatment and cracking or splitting mode for tube with a T6 heat treatment. For AA6061 T4 tubes of the same

dimensions, with the presence of a centrally located circular discontinuity, the energy absorption capacity has been increase by 22 %. Test specimen configuration and test results are shown in Figure 2.46 and Figure 2.47.

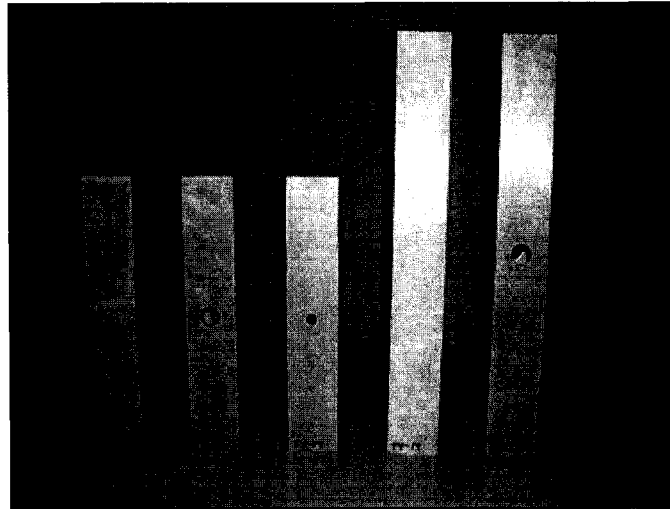


Figure 2.46. Test specimens used in reference [12].

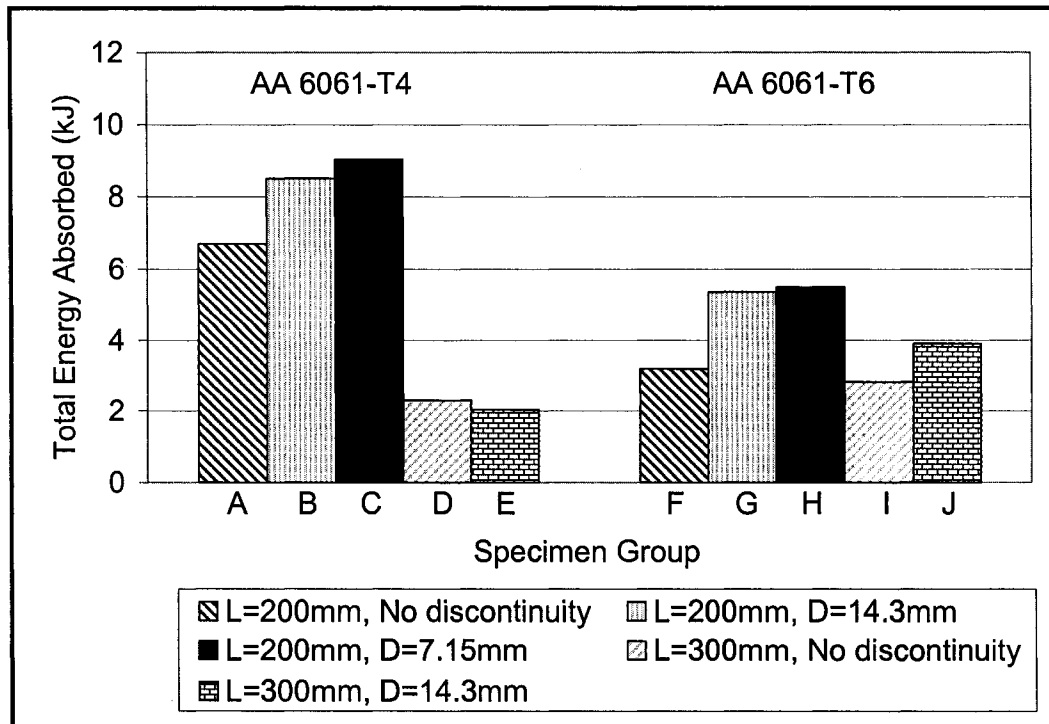


Figure 2.47. Mean total energy absorption for each crush test specimen group in reference [12].

2.4 Analytical Developments on the Axial Crushing of Square Tubes

Wierzbicki and Abramowicz [37] developed an analytical solution for the axial progressive crushing of a thin-walled square column using their super folding element method. The expression for the average or mean crush load was derived from the energy balance by equating the external work done by the crush load with energies dissipated in different types of deformation mechanisms as they occurred in a folding process.

The mean crushing force P_m can be calculated by

$$P_m = 13.06\sigma_0 b^{1/3} t^{5/3} \quad (2.3)$$

Where σ_0 denotes the flow stress of the sectional width; t is the wall thickness; b is the sectional width.

The half wavelength H for the folding deformation can be calculated by

$$H = 1.276b^{2/3} t^{1/3} \quad (2.4)$$

The flow stress σ_0 for material with power law hardening can be approximated by an energy equivalent stress [50]

$$\sigma_0 = \sqrt{\frac{\sigma_y \sigma_u}{1+n}} \quad (2.5)$$

where σ_y and σ_u denote the yield strength and the ultimate strength of the material, respectively; n is the exponent of the power law.

Magee and Thornton [51] have experimentally developed an analytical model for the calculation of mean crushing force. A relationship between structural effectiveness η of the section and relative density \emptyset was established by using data from crush tests of columns (steels ranging in tensile strength from 40 to 190 ksi, aluminum alloys and composites) of several different section geometries. The structural effectiveness η is defined as the ratio of specific energy (maximum energy that can be dissipated, divided by specimen weight) to the specific ultimate strength (ultimate tensile strength divided by material density). Also, the relative density \emptyset is defined as the ratio of material volume to the volume enclosed by the structural section. They then derived, by way of curve fitting, a relationship between these two parameters. Table 2.2 taken from reference [51]

shows the relationship for some basic structure configurations, where t is wall thickness, D outside diameter, S length of side, ρ_f foam density and ρ_m matrix density.

The expression for mean crush load is obtained from the expression for specific energy ($E_s = P_m / \rho \phi A_0$) and is of the form:

$$P_m = \eta \sigma_u \phi A_0 \quad (2.6)$$

ρ being the density and A_0 the overall area of the section as defined by its outer circumference. For a square section $\eta = 1.4 \phi^{0.8}$ and the mean crush load becomes:

$$P_m = 17t^{1.8} b^{0.2} \sigma_u \quad (2.7)$$

where b is the width of the side and t is the wall thickness.

Table 2.2. Empirical relationship between η and ϕ for the collapse of various structures [51].

Structure	$\eta = (\phi)$	ϕ
Cylindrical Tubes	$2\phi^{0.7}$	$4t/D$
Square and Rectangular Tubes	$1.4\phi^{0.8}$	$4t/S$
Honeycomb	$5\phi^{0.9}$	$8t/3S$
Foam	$0.7\phi - 4\phi$	ρ_f/ρ_m

One of the drawbacks of the formulations given by equation 2.3 and equation 2.7 is that the elasticity of the material has not been considered [1]. Thus, for the same ultimate strength, materials like steel and aluminum would exhibit the same mean crush strength (P_m). This has been shown by Mahmood and Paluszny [52] to be contrary to test findings, which do show a considerable difference in the crush characteristics for these two materials.

Mahmood and Paluszny [53] developed an analytical approach that overcomes some of these drawbacks. They start with a premise that thin walled box columns, composed of plate elements and subjected to axial compression, will buckle locally when critical stress is reached. Local buckling initiates the processes that lead to the eventual

collapse of the section and a subsequent folding of the column. The collapse strength of the section is related to its thickness/width (t/b) ratio and material properties. For very small t/b ratios ($t/b=0.0085-0.016$), representing the so called “non-compact” sections, the mode of collapse of a section will be influenced predominantly by the geometry, since its local buckling strength is considerably below the material yield strength. As shown in Figure 2.48, the mode of collapse of “non-compact” sections is characterized by large irregular folds, which give rise to a bending type (global buckling) instability that is induced by fold irregularities. For larger t/b ratios, typifying the “compact” sections in which the elastic buckling strength exceeds material yield strength, the material strength properties are expected to govern the mode of collapse and, consequently, the post-buckling stability. The collapse mode in this case, as shown in Figure 2.49, will appear very stable even in the presence of considerable geometry or loading imperfections. Since the “compactness” of an axially compressed column affects the stability of collapse, it is important to define when a section becomes “non-compact” and fails in a crumbling mode. According to Mahmood and Paluszny [54] the threshold (t/b) ratio is given as:

$$(t/b) < 0.48 \left[\sigma_y \frac{(1-\nu^2)}{E} \right]^{1/2} \quad (2.8)$$

where E is the Young’s modulus of elasticity and ν the Poisson’s ratio.

The elastic critical local buckling stress is

$$\sigma_{cr} = k\pi^2 E(t/b)^2 / 12(1-\nu^2) \quad (2.9)$$

$$k = (b/\lambda)^2 + p + q(\lambda/b)^2 \quad (2.10)$$

where λ is the elastic half wave length and p and q are factors that depend on the degree of restraint of its longitudinal edges. The plate with a smaller (t/b) ratio is regarded as a buckling plate and the other as the restraining plate.

In reference [52], for a square steel column, the maximum buckling load and mean crush load were given by equation 2.11 and 2.12

$$P_{\max} = 9430t^{1.86} b^{0.14} \beta^{-0.43} \sigma_y^{0.57} \quad (2.11)$$

$$P_m = 3270t^{1.86} b^{0.14} \beta^{-0.43} \sigma_y^{0.57} \quad (2.12)$$

Where, t is the wall thickness, b is the tube width, β is the material strain hardening factor, σ_y is the material yielding stress.



Figure 2.48. Folding pattern of thin-walled box with very small thickness/width ratio [53]. Reprinted with permission from SAE paper number 811302 (c) 1981 Society of Automotive Engineers, Inc.

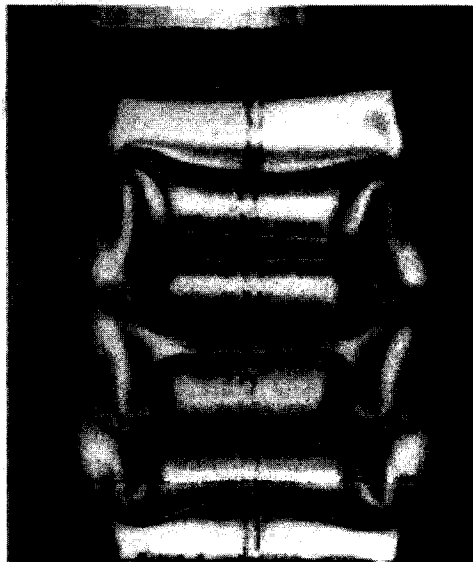


Figure 2.49. Folding pattern of thin-walled box with large thickness/width ratios [53]. Reprinted with permission from SAE paper number 811302 (c) 1981 Society of Automotive Engineers, Inc.

2.5 Finite Element Modeling of the Axial Crushing of Square Tubes

Analytical approaches as discussed in section 2.5 for axial collapse are valuable for quick calculations to get an approximate figure during the creative design stages of a column. However, these techniques do not lead themselves to the detailed design and analysis stages when specifics such as crush-controlling mechanisms are designed. On the other hand, numerical simulation is well-suited for detailed design analysis.

Numerical simulation for thin-walled column collapse has concentrated on both beam modelling and shell/plate theory. Beam modelling has been effective for low cost simulations (i.e. reduced modelling time and computer requirements). Shell/plate theory is generally regarded as the foundation of nonlinear, large deformation finite element analysis (FEA). The shell element that has been the basis of all crashworthiness simulations is the 4-noded Belytschko and Tsay shell [55]. For crashworthiness application, nonlinear FEA can be used to simulate component, subsystem and integrated system including occupant, restraint system and detailed vehicle structure [56, 57].

Langseth, Hopperstad, and Berstad [58] have numerically simulated the axial crash of aluminum extrusions by using explicit non-linear code LS-DYNA. The simulation results were validated by the experimental testing results reported in reference [11]. As mentioned in reference [58], an essential ingredient in the development and use of numerical simulation is the validation of the codes by comparison with precision tests. This is of vital importance when introducing new materials, such as aluminium alloys, which compared to commonly used steel qualities have different material characteristics.

In the finite element model, as shown in Figure 2.50, the free length of the specimens was 310 mm. At the lower end all degrees of freedom were fixed, while at the upper end the rotational degrees of freedom were fixed to avoid unrealistic deformation modes. Since the symmetric collapse mode was observed in experimental testing, only one quarter of the tube was modeled in order to save computation time. The tubes were modeled using Belytschko-Lin-Tsay shell elements. A material model developed by Berstad, Hopperstad, and Langseth [59] was applied to the tube models (material 103 in LS-DYNA). This material model uses isotropic elasticity, the von-Mises yield criterion and non-linear isotropic hardening. The hardening of the material at strains beyond those

where diffuse necking takes place is extrapolated using an equation based on the stress strain data used as input. The contact between the rigid block and the specimen was modelled using a nodes-to-surface contact algorithm with a friction coefficient of 0.25 to avoid lateral movements. To account for the contact between the lobes during deformation, a single surface contact algorithm without friction was used. Furthermore, several simulations were carried out to determine the proper mesh density and an element size of 3×3 mm was found to be sufficient, giving a total of 2500 elements in the quarter model. As shown in Figure 2.50, a trigger was created by moving a group of nodes 2 mm out of the plane of the side wall.

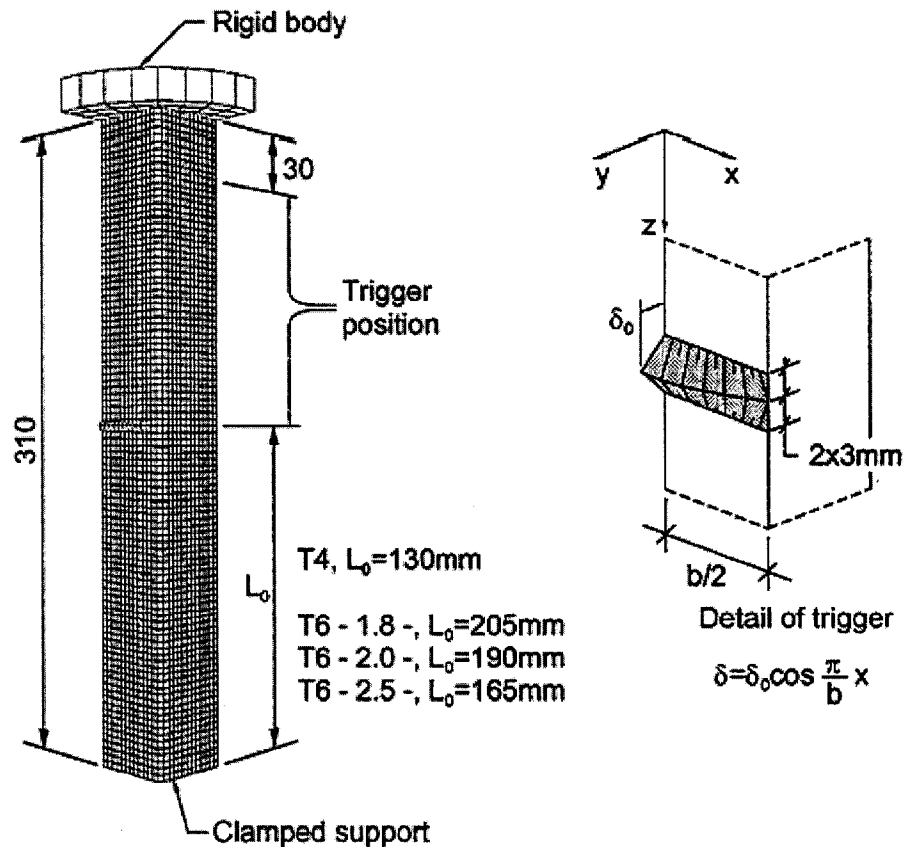


Figure 2.50. One quarter "finite element model including trigger position in reference [58].

The results of the simulations of these models correlated well with the experimental results of reference [11]. As with the experimental results, the numerical results showed that six lobes were formed in the model with the T4 heat treatment while

seven lobes were formed in the model with the T6 heat treatment. Furthermore, the numerically calculated peak buckling and mean crushing loads were found to be within 10% of their experimentally obtained counterparts.

Yamazaki and Han [60, 61] used LS-DYNA to study the dynamic axial crushing of square tubes. In their study, crash triggers were added to the tube models by moving one node out of its side-wall plane by a magnitude of 1% of the wall thickness to simulate the inherent geometrical or material imperfections. Shell and brick elements were used in the simulation based on the wall thickness of specimens.

Arnold and Altenhof [13] have numerically investigated the influence of circular discontinuities and material properties on energy absorption characteristics of aluminum extrusions. Due to the symmetry observed in the experimental quasi-static crushing process of these specimens [12], only one quarter of the absorber specimen was modelled. Solid elements were used for the model development. As shown in Figure 2.51, the mesh density was finer in the region of the structure surrounding the circular hole discontinuity. This was necessary in order to ensure an accurate calculation of the stress distribution resulting from the stress concentration caused by the circular hole discontinuity. Four layers of elements through the thickness of the tubes were utilized to accurately calculate the stress and strain distribution. Surface to surface contact algorithm available in LS-DYNA was used to model the contact between rigid plate and the tubes. Single-surface contact algorithm was used to model the contact between the lobes during tube deformation.

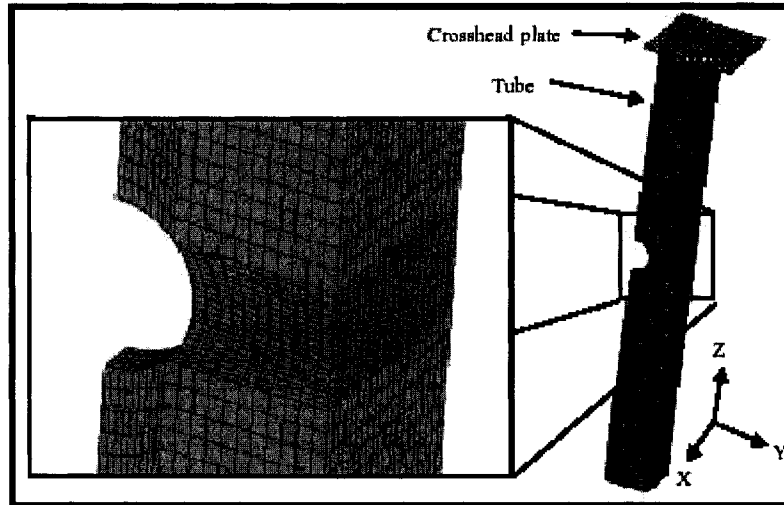
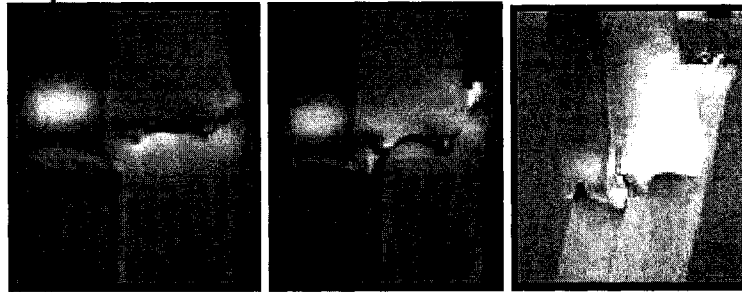


Figure 2.51. Discretization of group B, G, and L specimens (L=200 mm, D=14.2 mm, t=3.15 mm) [13]. Reprinted with permission from SAE paper number 2005-01-0703 (c) 2005 Society of Automotive Engineers, Inc.

Material model 105 in LS-DYNA was used to model the extrusion absorber materials considered in this research. This material allows the direct input of the true stress versus true plastic strain data in the form of a piecewise linear curve. During the simulation, LS-DYNA performs a curve fit of the data and determines the strain hardening properties. This material model also allows the implementation of failure mechanism. An iterative calibration process was capable to determine the material failure parameters D_c and S .

A good correlation was observed between the results of FE simulations and the results of quasi-static crush testing of extrusion absorber structures. FE simulations successfully predicted the cracking and complex splitting collapse modes that were observed in experimental testing of the AA6061-T6 and AA6063-T5 tube specimens as show in Figure 2.52 and Figure 2.53.

Experimental:

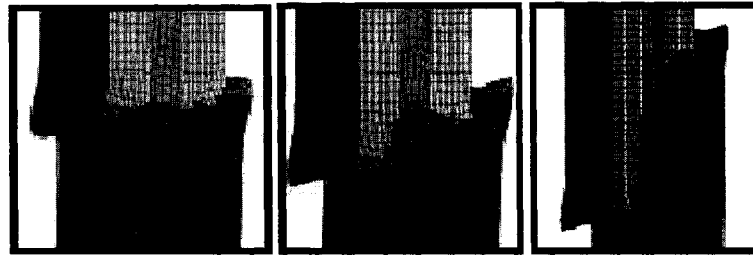


a) $d=9\text{mm}$

b) $d=19\text{mm}$

c) $d=55\text{mm}$

Numerical:



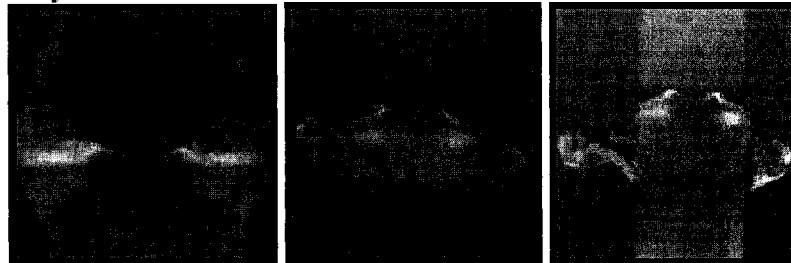
e) $d=9\text{mm}$

f) $d=19\text{mm}$

g) $d=54\text{mm}$

Figure 2.52. Experimental and numerical crushing process for T6 specimen [13]. Reprinted with permission from SAE paper number 2005-01-0703 (c) 2005 Society of Automotive Engineers, Inc.

Experimental:

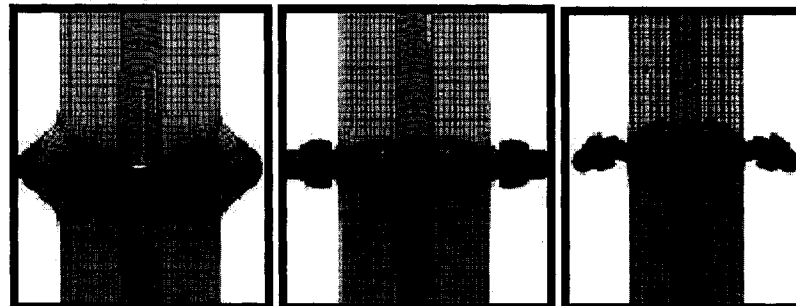


a) $d=14.0\text{mm}$

b) $d=35.0\text{mm}$

c) $d=47.0\text{mm}$

Numerical:



e) $d=14.0\text{mm}$

f) $d=35.0\text{mm}$

g) $d=47.0\text{mm}$

Figure 2.53. Experimental and numerical crushing process for T5 specimen [13]. Reprinted with permission from SAE paper number 2005-01-0703 (c) 2005 Society of Automotive Engineers, Inc.

3. FOCUS OF RESEARCH

The research documented in this thesis focuses on the investigation of deformation behaviour and energy absorption capacity improvements of structural members made from braided stainless steel tube and aluminum extrusions. Braided stainless steel tubes as a prospective energy absorbing component is intended to be used under tensile loading conditions. Deformation behaviour and energy absorption capacity of aluminum foam filled braided stainless steel tubes were experimentally and analytically investigated. For energy absorbing devices under compressive loading conditions, deformation modes and influence of crush initiators were experimentally investigated. An experimental investigation was conducted to compare the crush characteristics and energy absorption capacity of AA6061-T6 aluminum alloy extrusions with centrally located circular, slotted, and elliptical through-hole discontinuities. Another experimental investigation was completed to investigate the load/displacement and energy absorption characteristics of aluminum extrusions under a cutting deformation mode by the use of a specially designed cutting tool. In summary, the following research was completed were taken to investigate deformation process and to explore energy absorption improvement methods of structural members:

- 1) Analytical investigations of the deformation process and energy absorption of aluminum foam filled braided stainless steel tubes under quasi-static tensile loading conditions.
- 2) Experimental investigations on the axial crush behaviour of AA6061-T6 aluminum square tubes with different types of through-hole discontinuities. Three different types of geometrical discontinuities, namely, circular, slotted and elliptical holes were fabricated into AA6061-T6 structural members.
- 3) Load displacement and energy absorption performances of AA6061-T6 tubes under a cutting deformation mode were investigated. A specially designed cutting tool was used to cut the four corners of the aluminum tubular extrusions under compressive loads.

4. EXPERIMENTAL TESTING METHOD

The experimental testing involved in this research included the quasi-static axial compressive crushing of AA6061-T6 extrusions with different geometrical discontinuities and quasi-static axial compressive cutting of AA6061-T6 extrusions. Aluminum extrusions considered in this research had a nominal side width of 38.1 mm, wall thickness of 3.15 mm and tube lengths of 200 mm and 300 mm. For the development of an analytical model to predict energy absorption of aluminum foam filled braided stainless steel tube, an overview of the experimental work completed by Powell and Altenhof [5] is given in this section for the quasi-static tensile testing of both braided stainless steel tube and aluminum foam filled braided stainless steel tube. An overview is also given for the tensile testing of dog-bone shaped specimens extracted from the as-received AA6061-T6 aluminum alloy extrusion as accomplished by Arnold [12].

4.1 Overview of Tensile Testing of Empty Braided Stainless Steel Tubes

The braided tube was woven with AISI 304 stainless steel wires with a diameter of 0.51 mm. The mechanical characteristics of AISI 304 stainless steel is presented in Table 4.1 [62]. Eight strands of wire formed a tow and 48 tows were interlaced together around the circumference of the tube. The nominal tube diameter of the braid that was selected for this study was 64.5 mm. A standard weave of the tows was used in this research, which consists of a “2 over, 2 under” pattern as illustrated in Figure 4.1.

Table 4.1. Mechanical characteristics of the AISI 304 stainless steel braid wire [62].

Young's modulus (GPa)	Yield strength (MPa)	Tensile strength (MPa)	Elongation (%)	Density (kg/m ³)
193	241	586	55	8027

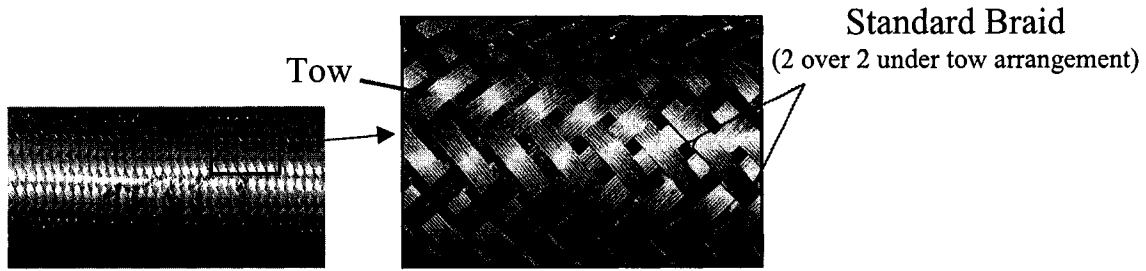


Figure 4.1. Stainless steel braided tube geometry and tow profile.

Tensile testing for unfilled braided tubes was carried out to assess the mechanical characteristics of the tube. Experimental testing was completed on a hydraulic 150 kN Tinius Olsen tension/compression testing machine. A 150 mm range linear voltage differential transformer (LVDT) was used to measure the displacement of the translating platform on the testing machine. Data acquisition, which obtained load and displacement from the Tinius Olsen testing machine, was performed using a personal computer at a sampling rate of 10 Hz.

Through a trial and error process it was determined that a circular clamping device, as illustrated in Figure 4.2, best constrained the motion of the ends of the braided tube to the testing machine. The two clamp housings, one for each end of the tube, were fastened to the translating and stationary crossheads of the Tinius Olsen testing machine. After insertion of the tube in the clamp housing the conical wedge was pressed into the housing with a load of approximately 27 kN. This procedure was conducted to minimize any slipping which may occur between the braided tube and the wedge/clamp housing. Tensile testing was completed at a nominal crosshead speed of 30 mm/min. Braided tube specimens with lengths of 185 mm and 330 mm, measured between clamp points, were tested. Tensile testing was deemed completed when either failure of the tube occurred or when maximum crosshead stroke was reached.

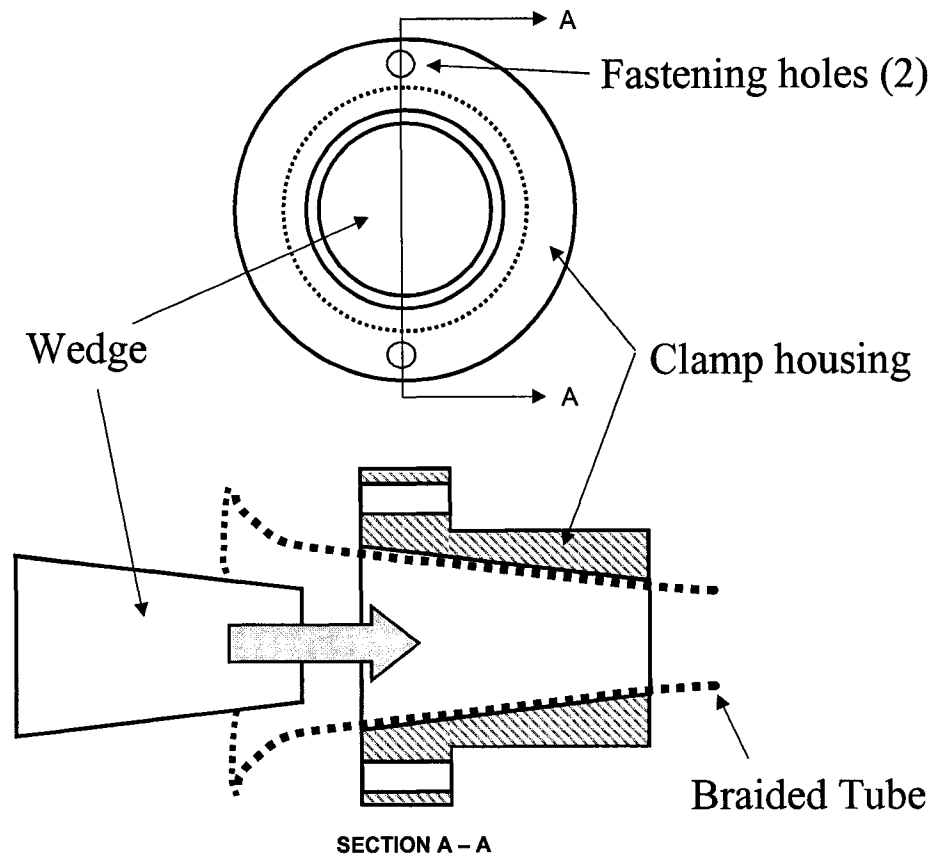


Figure 4.2. Circular clamping device.

4.2 Overview of Tensile Tests of Aluminum Foam Filled Braided Tubes

Prior to assembly of the aluminum foam cores and the braided tubing, preparation of both materials was completed. Braided tube lengths of 610 mm, which had a mass of approximately 713 g, were cut from an 8 m length of braided tube using sheet metal cutters. Four aluminum foam specimens, with densities of 248 kg/m³, 288 kg/m³, 298.2 kg/m³, and 373 kg/m³, were cut into rectangular prisms with approximate dimensions of 305 mm length, 74 mm height, and 50 mm width, using a conventional band saw. The assembly process of the aluminum foam filled braided stainless steel tube involved considerable human effort and did not encompass the use of any machinery. Figure 4.3(a) shows the unfilled tube in its undeformed configuration. The braided tube was compressed, as illustrated in Figure 4.3(b), to an extent such that the aluminum foam core, when inserted, slid into the compressed tube with minimal effort or guidance, as

shown in Figure 4.3(c). Compression of the tube increased the angle between the tows resulting in an increase in the diameter of the tube. No permanent deformation of the tube was resulted due to the compression and great efforts were taken to ensure that snagging of the foam core edges on the wires of the braided tube did not occur. To complete the preparation of the test specimen, the tube was released from its compressed state and the braided tows were carefully massaged to ensure that the foam core was centered within the length of the tube as illustrated in Figure 4.3(d). Figure 4.3(e) depicts the aluminum foam core within the braided tube as viewed from the tube opening. After assembly, the angle between tows was measured to be 53° and the length of the foam filled braided tube was approximately 525 mm.

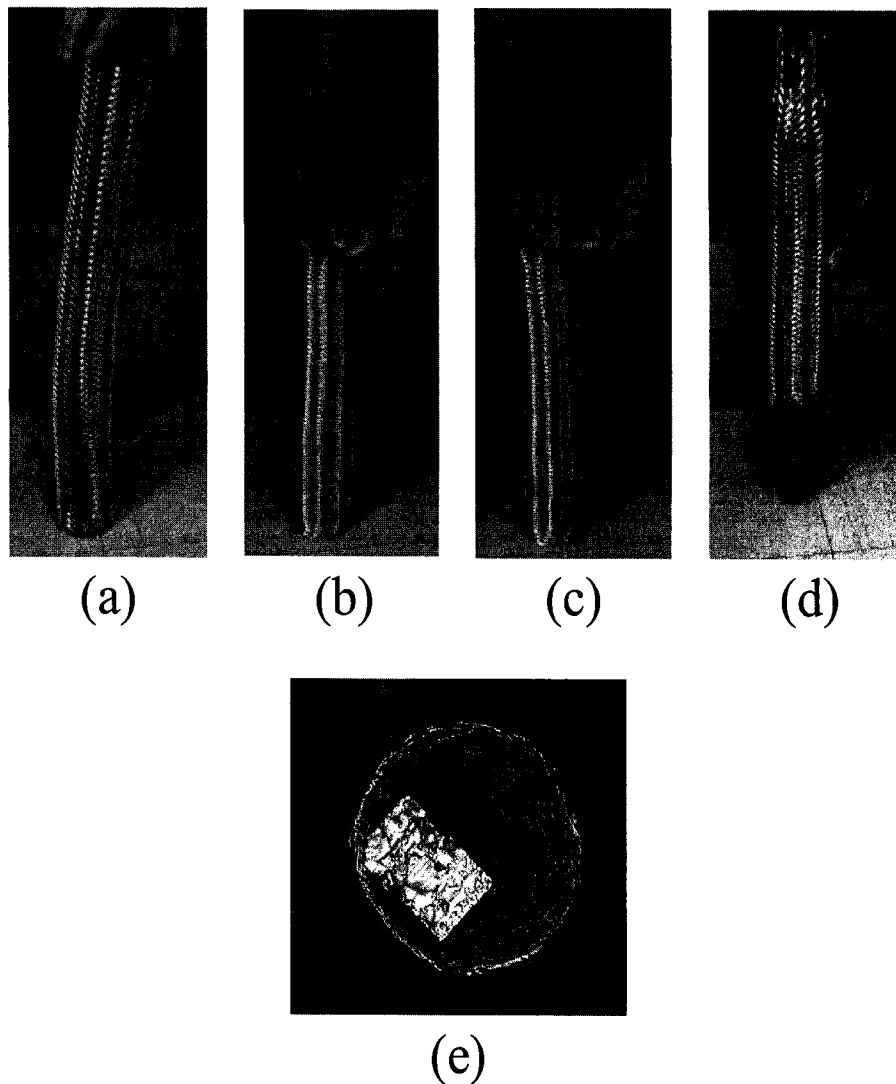


Figure 4.3. Assembly process of the aluminum foam filled braided tubes.

The circular wedge clamps, which were fastened to the fixed and translating crossheads of the tension/compression testing machine, were used to secure the upper and lower ends of the foam filled braided tube. Prior to the tensile testing, the length of each aluminum foam filled braided tube was verified to be 405 mm measured between the clamp points. The position along the direction of crosshead displacement, the z-axis direction, of each tube was set such that the foam core was centered in between the translating and fixed crossheads. An approximate spacing of 50 mm from the top and bottom of the foam core to the fixed and translating crossheads existed prior to tensile testing as illustrated in Figure 4.4. A 27 kN load was applied to each circular wedge to ensure that slipping between the braided tube and the wedge/clamp housing was minimized.

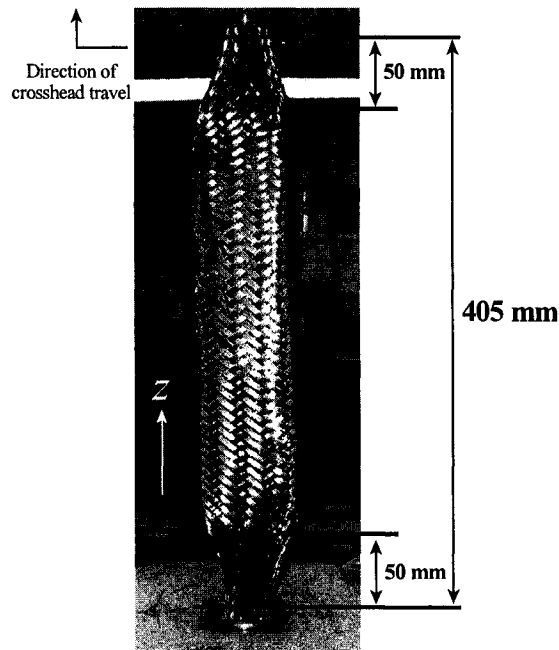


Figure 4.4. Aluminum foam filled braided tube secured into the tensile testing machine prior to loading.

Tensile tests for all specimens were completed at a nominal crosshead speed of 75 mm/min. Due to crosshead travel restrictions of the tension/compression testing machine, which was limited to approximately 150 mm, the complete test for each specimen was divided into three distinct stages. In the first stage of tensile loading

(referred to as “stage 1”), both of the circular clamp housings were fastened to the fixed and translating crossheads and testing was completed after approximately 150 mm of crosshead travel. The load was removed from the specimen and the clamping housing on the upper, translating crosshead was unfastened from the crosshead. Prior to the second stage of loading, a 171 mm spacer was placed in between the upper translating crosshead and the support flange of the clamp housing. The position of the translating crosshead was reset to the starting position. Tensile loading was repeated and referred as “stage 2” of the complete testing procedure for the specimen. After approximately 150 mm of crosshead travel, the load was removed from the specimen. A second 108 mm length spacer was placed in between the 171 mm spacer and the clamp housing. Tensile loading was repeated a third time and referred as “stage 3” of the complete tensile testing procedure. Use of the spacers and repeated loading permitted approximately 420 mm of axial elongation of the foam filled braided tubes.

4.3 Overview of Tensile Testing of Aluminum Extrusion Material Properties

Tensile tests were performed to acquire material properties of the commercially obtained AA6061-T6 aluminum extrusions. Eight tension test specimens were extracted from the sides of the tube stock in the direction of extrusion. The testing was completed in accordance to ASTM standard E8M [63] on an INSTRON tensile testing machine equipped with a 100 kN load cell. The elongation in the specimen was measured using an extensometer with a gauge length of 25.4 mm. Data from the load cell and extensometer was acquired using a personal computer data acquisition system. Load and extension measurements were recorded at a sampling rate of 5 Hz. The tests were conducted using a constant crosshead speed of 5 mm/min.

4.4 Quasi-static Axial Crush Testing

The aluminum extrusions used in this testing were square cross section AA6061-T6 tubes with a nominal side width (C) of 38.1 mm, wall thickness (t) of 3.15 mm and length (L) of 200 mm. Under compressive axial loading, the structures under consideration had L/C and C/t ratios that resulted in a prediction of global bending

collapse, according to theoretical and empirical predictions reported by Abramowicz and Jones [14]. In order to change the collapse mode of the structures from global bending to a mode that promotes greater energy absorption, centrally located geometrical discontinuities were placed at two opposite side walls at the midpoint of the extrusion structures. It was expected that these discontinuities would act as crush initiators and have the effect of decreasing the peak buckling load and increasing energy absorption.

Circular, slotted and elliptical holes with different major axis lengths and aspect ratios were selected as the geometrical discontinuities to be investigated in this research. The major axis of a discontinuity refers to the longer axis of the discontinuity which is perpendicular to the direction of compression. The minor axis is perpendicular to the major axis. The major and minor axes for a circular discontinuity are equal to the diameter of the circular hole. The aspect ratio is defined as the ratio of the length of major axis to the length of the minor axis and is equal to unity for circular discontinuities. Specimens with circular holes and slotted holes were fabricated using a Cincinnati BridgePort milling machine with a digital readout. Specimens with elliptical holes were fabricated using a 1 mm diameter endmill on a vertical CNC milling machine. No deburring treatment was needed by use of these machining methods. The location and the geometry shape of the discontinuities and the aluminum extrusion are illustrated in Figure 4.5.

Specimens were organized into four groups. Group 1 contained specimens without any discontinuity. For the remaining groups, each group had a different major axis length and included specimens with circular, slotted and elliptical discontinuities. Specimens were further classified into sub-groups within Groups 2, 3, and 4 according to the geometry of the discontinuity fabricated into the specimen. The detailed geometries and dimensions are presented in Table 4.2, Table 4.3 and Table 4.4 for specimens within Group 2, Group 3 and Group 4 respectively.

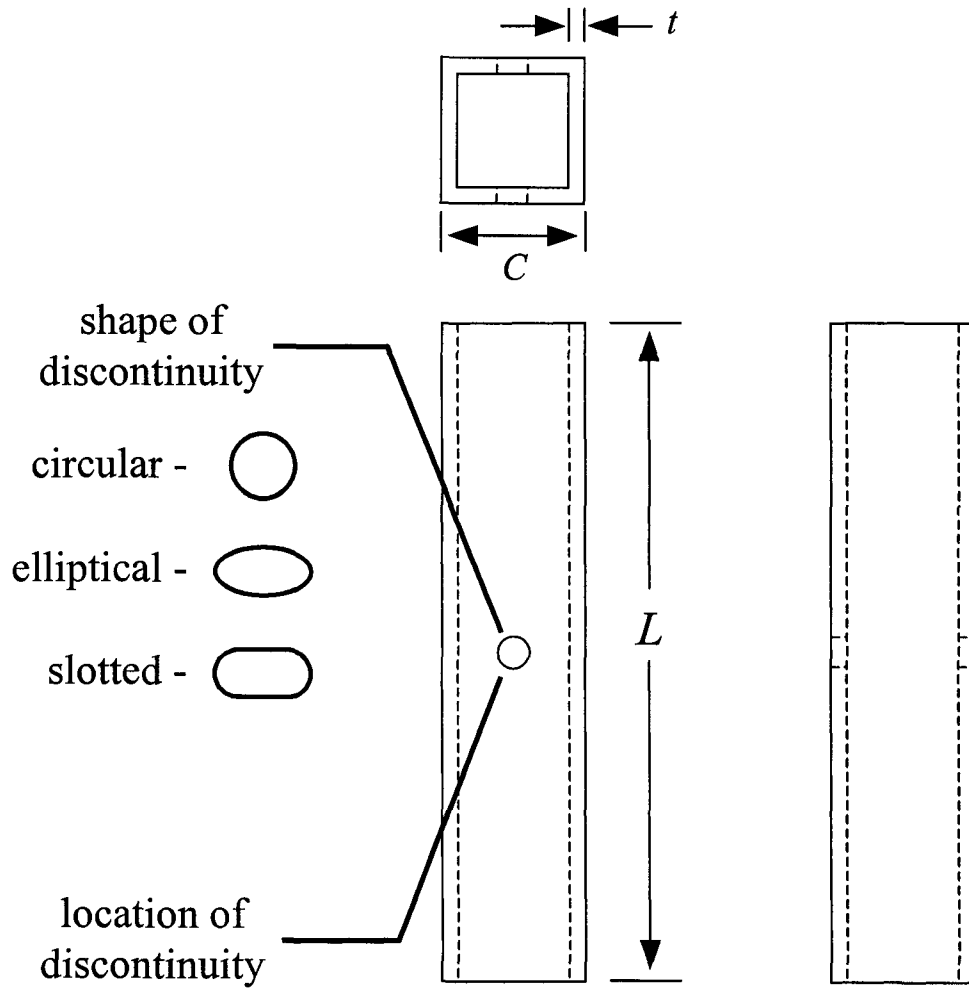


Figure 4.5. Geometries of the aluminum extrusion and discontinuities under consideration. L is the tube length, C is the width of the sidewalls and t is the wall thickness of the tube specimens.

Table 4.2. Specimen geometries in Group 2

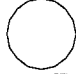
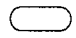





Group 2			Discontinuity description	Discontinuity Shape	
Sub-group identifier	Shape of discontinuity	Specimen #		Major Axis (mm)	Aspect ratio
C2		T6-5, T6-6 T6-7, T6-8	circular discontinuity	14.29	1.0
S2-3		T6S-1, T6S-2 T6S-3, T6S-4	slot shape discontinuity	14.29	3.0
S2-2		T6S-5, T6S-6 T6S-7, T6S-8	slot shape discontinuity	14.29	2.0
S2-1		T6S-9, T6S-10 T6S-11, T6S-12	slot shape discontinuity	14.29	1.33
E2-3		T6E-1, T6E-2 T6E-3, T6E-4	elliptical shape discontinuity	14.29	3.0
E2-2		T6E-5, T6E-6 T6E-7, T6E-8	elliptical shape discontinuity	14.29	2.0
E2-1		T6E-9, T6E-10 T6E-11, T6E-12	elliptical shape discontinuity	14.29	1.33

Table 4.3. Specimen geometries in Group 3


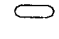




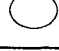
Group 3			Discontinuity description	Discontinuity Size	
Sub-group identifier	Shape of discontinuity	Specimen #		Major Axis (mm)	Aspect ratio
C3		T6-9, T6-10 T6-11, T6-12	circular discontinuity	10.72	1
S3-3		T6S-13, T6S-14 T6S-15, T6S-16	slot shape discontinuity	10.72	3.0
S3-2		T6S-17, T6S-18 T6S-19, T6S-20	slot shape discontinuity	10.72	2.0
S3-1		T6S-21, T6S-22 T6S-23, T6S-24	slot shape discontinuity	10.72	1.33
E3-3		T6E-13, T6E-14 T6E-15, T6E-16	elliptical shape discontinuity	10.72	3.0
E3-2		T6E-17, T6E-18 T6E-19, T6E-20	elliptical shape discontinuity	10.72	2.0
E3-1		T6E-21, T6E-22 T6E-23, T6E-24	elliptical shape discontinuity	10.72	1.33

Table 4.4. Specimen geometries in Group 4

Group 4			Discontinuity Shape		
Sub-group identifier	Shape	Specimen #	Discontinuity description	Major Axis (mm)	Aspect ratio
C4	○	T6-13, T6-14 T6-15, T6-16	circular discontinuity	7.14	1.0
S4-3	◓	T6S-25, T6S-26 T6S-27, T6S-28	slot shape discontinuity	7.14	3.0
S4-2	◓	T6S-29, T6S-30 T6S-31, T6S-32	slot shape discontinuity	7.14	2.0
S4-1	○	T6S-33, T6S-34 T6S-35, T6S-36	slot shape discontinuity	7.14	1.33
E4-3	◓	T6E-25, T6E-26 T6E-27, T6E-28	elliptical shape discontinuity	7.14	3.0
E4-2	◓	T6E-29, T6E-30 T6E-31, T6E-32	elliptical shape discontinuity	7.14	2.0
E4-1	○	T6E-33, T6E-34 T6E-35, T6E-36	elliptical shape discontinuity	7.14	1.33

4.4.1 Quasi-static axial crush testing method

Compressive tests were completed on a hydraulic Tinius-Olsen testing machine. Specimens were placed on the centre of a translating crosshead of the compression testing machine such that the axial direction of the test specimen was parallel to the direction of translation of the moving crosshead. A fixed crosshead was located above the test specimen. The load cell used to measure the compressive force had a range of 150 kN. Displacement was measured using a linear voltage differential transformer (LVDT) with a range of 150 mm. A personal computer equipped with data acquisition software was used to record the measurements from the load cell and the LVDT at a sampling rate of 60 Hz. The specimens were crushed at a nominal crosshead speed of 120 mm/min. At this testing speed, it was considered acceptable to evaluate the crush behaviour as quasi-static deformation [64]. All tests were performed at room temperature.

4.5 Quasi-static Axial Cutting Testing

The aluminum extrusions considered in this testing were square AA6061-T6 tubes with a nominal side width (C) of 38.1 mm, wall thickness (t) of 3.15 mm, and lengths (L) of 200 mm and 300 mm as illustrated in Figure 4.6. Under compressive axial loading, the tubular members in consideration had L/C and C/t ratios that resulted in a prediction of global bending collapse, according to theoretical and empirical predictions reported by Abramowicz and Jones [14]. These tubular geometries were selected to see if the cutting mode of deformation suppressed the global bending deformation mode. Furthermore, to investigate the stability of the cutting deformation process a longer tube length (300 mm) was also considered in this investigation.

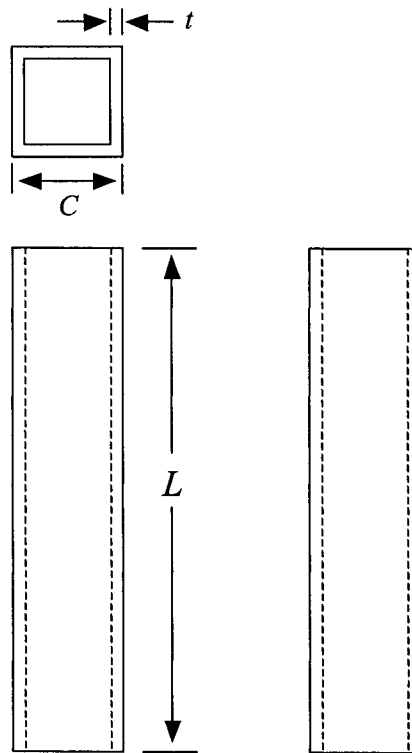


Figure 4.6. Geometry of aluminum extrusion considered in this research. L is the tube length, C is the width of side walls and t is the nominal wall thickness.

4.5.1 Cutting Tool Design and Manufacturing

In an effort to generate a cutting mode of deformation within the tubular members a cutting tool was designed with four thin cutting blades with widths that should initiate stresses in the tubular member which should exceed the ultimate stress of the AA6061-T6 alloy without deformation or failure of the cutting blades.

The shape and dimensions of the cutting tool are shown in Figure 4.7. Four tapered cutting blades, 7 mm in length, were CNC machined from AISI 4140 round bar stock. The geometry of the cutter was designed to slit the aluminum extrusion in each of the four corners of the tube. The outside diameter of the cutter and thickness were 101.6 mm and 20 mm respectively. The cutting edge had a width of 3 mm with a taper at both edges to 1.2 mm.

After machining, the cutting tool was heat treated in a two stage process as detailed in reference [65]. The cutter was heated to 843°C and held at this temperature for one hour to ensure the completeness of the austenitic transformation. The second stage involved oil quenching to room temperature. Oil quenching provided a fast cooling rate to produce a martensitic structure. After hardening, tempering was completed at a temperature of 225°C for one hour to reduce residual stresses induced during quenching. The hardness of both sides of the cutter after heat treatment was determined and is listed in Table 4.5.

After manufacturing and heat treatment the width of the tips of the cutting blades were measured using a Vernier calliper. The measured values of the widths for each blade are listed in Table 4.6 and the corresponding location of each blade on the cutter is presented in Figure 4.8. It was found that the thinner blades on side A corresponded to thicker blades on side B. The average blade tip thickness of side A was 1.12 mm, and the average blade tip thickness of side B was 1.09 mm. Also illustrated in Figure 4.8 is the hub of the cutter which supported the blades and was the location of force application to the cutter from the testing machine.

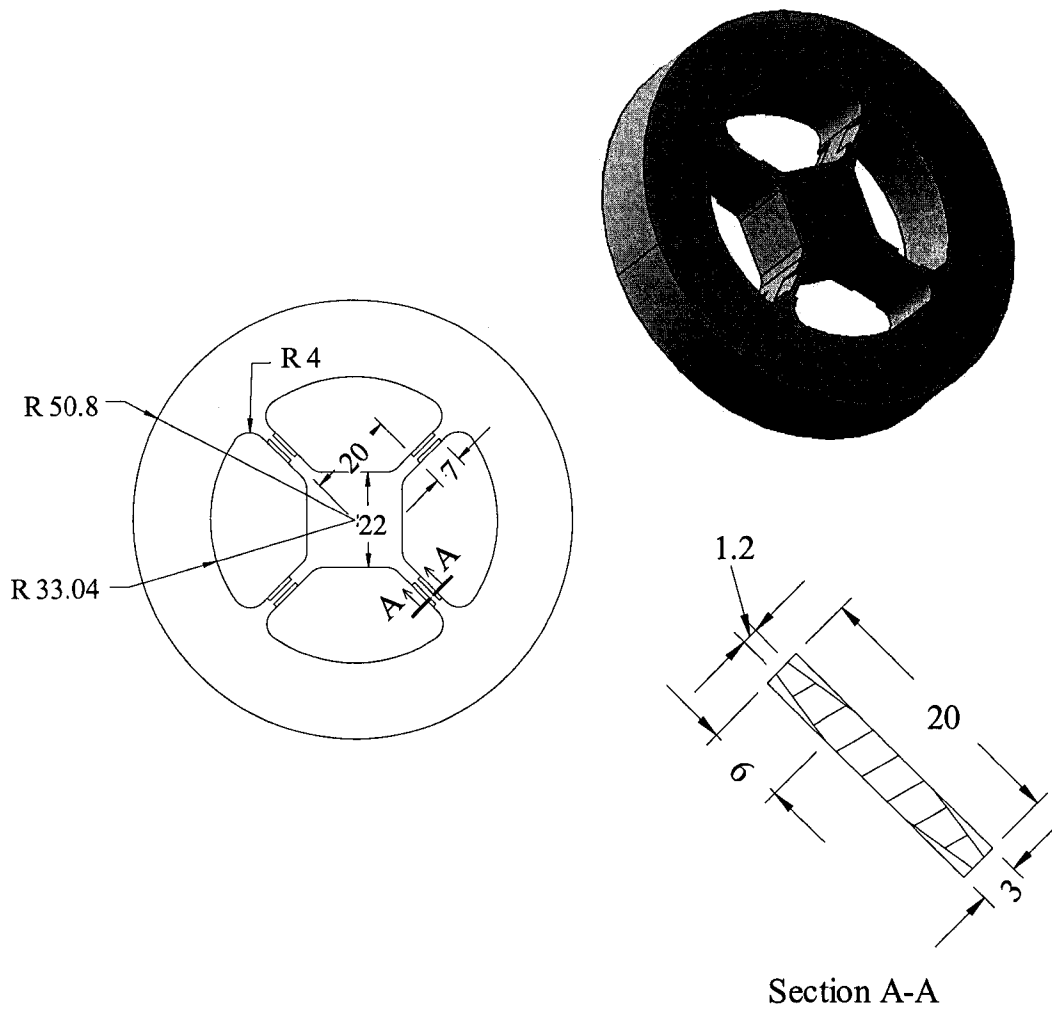


Figure 4.7. Cutting tool shape and dimensions (all dimensions are in mm)

Table 4.5. Hardness measurements of the cutter after heat treatment.

Side A		Side B	
Surface hardness (Rockwell 'C' scale)		Surface hardness (Rockwell 'C' scale)	
Rim	Centre	Rim	Centre
54.0	52.7	54.0	56.6

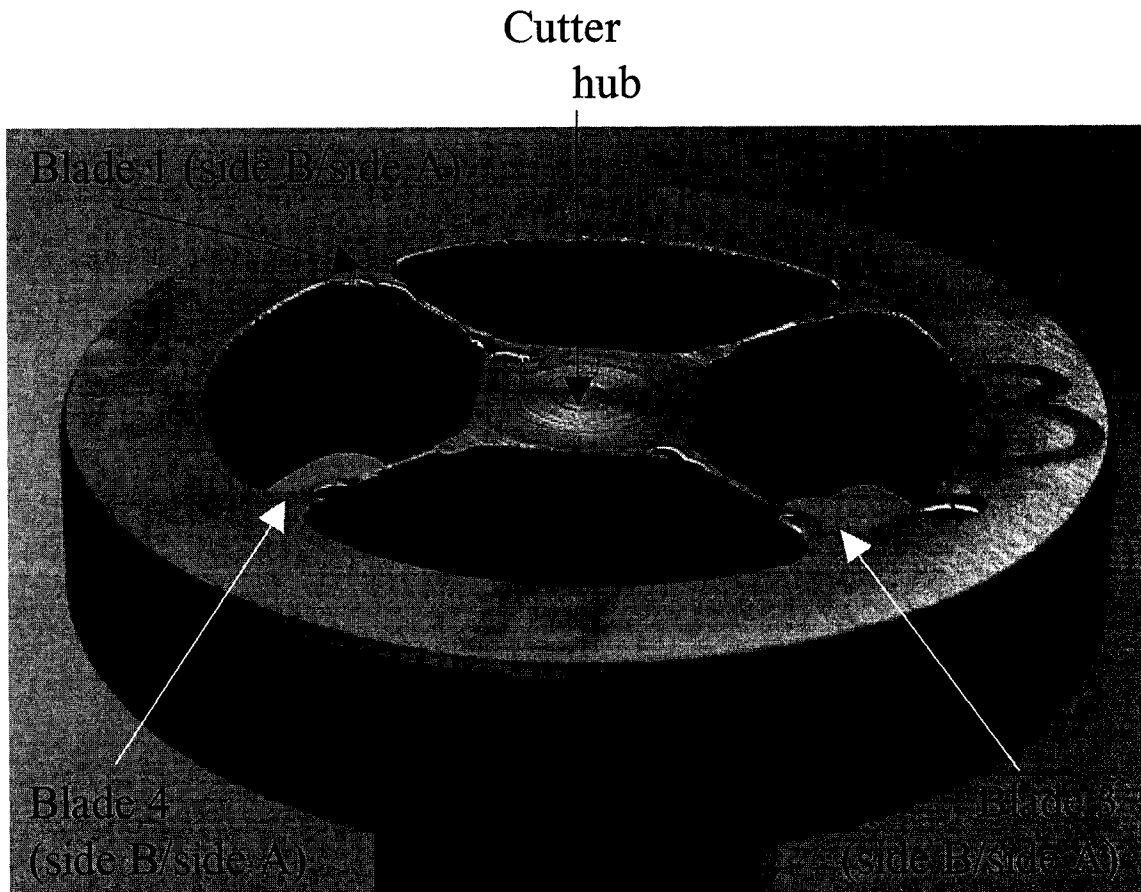


Figure 4.8. Cutting blade positions after manufacturing and heat treatment (side B facing upwards).

Table 4.6. Blade tip width dimensions (in mm) of cutter on sides A and B.

	Blade 1	Blade 2	Blade 3	Blade 4
Side A	1.21	1.03	1.26	0.97
Side B	0.93	1.25	0.93	1.23

4.5.2 Quasi-Static Axial Cutting Testing Method

Twenty quasi-static axial cutting tests were performed to evaluate the design of the cutter and the energy absorption and load/displacement behaviour of the aluminum extrusions under the cutting deformation mode. Six quasi-static axial buckling tests,

without the presence of the cutter, were also completed to compare the deformation modes of both types of loading conditions. It is acceptable practice to evaluate energy absorbing structures quasi-statically as many dynamic impact events that energy absorbing structures are subjected to occur at velocities that may be considered quasi-static. It is generally accepted, and noted in reference [64], that dynamic loads applied at velocities on the order of 10 m/s or lower may be considered quasi-static. Furthermore, strain rate effects for the extrusions under consideration may be neglected since aluminum alloys are considered strain rate insensitive [12].

Test specimens were organized into six groups. Each group for the cutting tests had five specimens. For the axial buckling tests (testing without the use of the cutter), each group had three specimens. Specimens in group 1 and group 2 had a tube length of 200 mm and were tested using side A and side B of the cutter, respectively. Specimens in group 3 and group 4 had a length of 300 mm and were tested using side A and side B of the cutter, respectively. Specimens in group 5, with a tube length of 300 mm, and specimens in group 6, with a tube length of 200 mm, were tested under crush loading without the use of the cutter. Detailed specimen grouping information and geometry dimensions are listed in Table 4.7.

Axial compressive testing was performed using a hydraulic 150 kN loading capacity Tinius-Olsen testing machine. The specimen was placed vertically on the centre of the fixture of the testing machine. The cutter was placed on the top end of the extrusion with careful alignment to make sure the cutting blades were in the proximity of the four corners of the tube. A lubricating liquid, with a trade name “Pump-Spray PS-8”, was sprayed on the four cutting blades of the cutter. For the last two completed cutting tests, namely specimens LB4 and LB5, no lubrication was used to check the role of lubrication fluid on the cutting force. A round steel bar with a diameter of 25.4 mm was inserted between the cutter and the translating crosshead. The setup of the test prior to and during the initial cutting of the extrusion is illustrated in Figure 4.9.

The load cell used to measure the compressive load had a range of 150 kN. Displacement was measured using a linear voltage differential transformer (LVDT) with a range of 150 mm. A personal computer equipped with data acquisition software was used to record the measurements from the load cell and the LVDT at a sampling rate of

60 Hz. The specimens were cut/crushed at a crosshead speed of approximately 120 mm/min. At this testing speed, it is considered acceptable to evaluate the behaviour as quasi-static deformation [64]. All tests were performed at room temperature.

Table 4.7. Specimen grouping information and geometry.

Group	Specimens	Length (mm)	Tube width (mm)	Tube thickness (mm)	Cutter side
1	SA1	200	38.1	3.15	A
	SA2	200	38.1	3.15	A
	SA3	200	38.1	3.15	A
	SA4	200	38.1	3.15	A
	SA5	200	38.1	3.15	A
2	SB1	200	38.1	3.15	B
	SB2	200	38.1	3.15	B
	SB3	200	38.1	3.15	B
	SB4	200	38.1	3.15	B
	SB5	200	38.1	3.15	B
3	LA1	300	38.1	3.15	A
	LA2	300	38.1	3.15	A
	LA3	300	38.1	3.15	A
	LA4	300	38.1	3.15	A
	LA4	300	38.1	3.15	A
4	LB1	300	38.1	3.15	B
	LB2	300	38.1	3.15	B
	LB3	300	38.1	3.15	B
	LB4	300	38.1	3.15	B
	LB5	300	38.1	3.15	B
5	LG1	300	38.1	3.15	N/A
	LG2	300	38.1	3.15	N/A
	LG3	300	38.1	3.15	N/A
6	SG1	200	38.1	3.15	N/A
	SG2	200	38.1	3.15	N/A
	SG3	200	38.1	3.15	N/A

N/A – tubes in groups 5 and 6 were axially crushed without the use of the cutter.

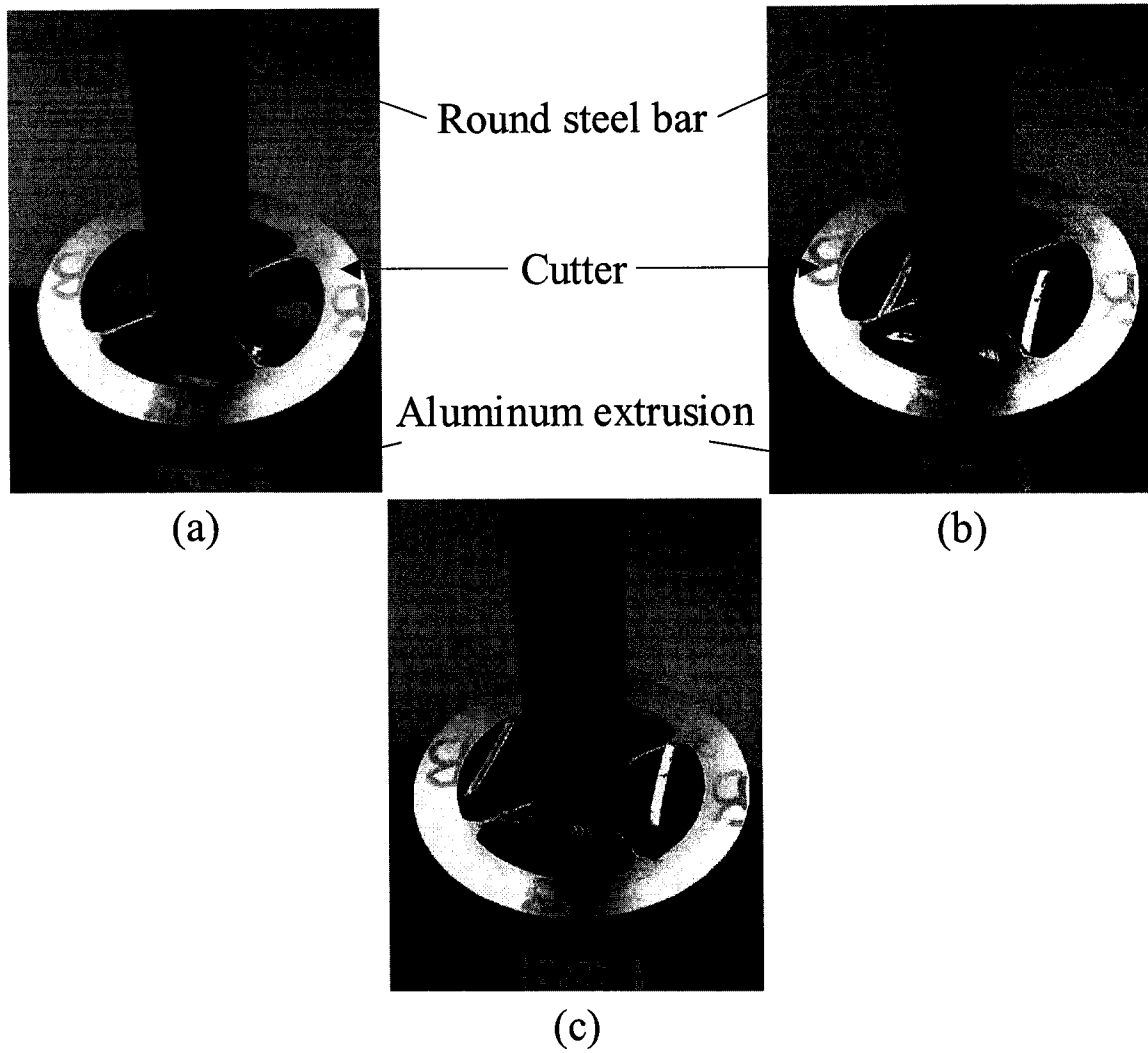


Figure 4.9. Cutting test setup. (a) Setup of the test prior to axial crushing, (b) penetration of blades of cutter into aluminum extrusion commencing on specimen SA2, (c) cutting in progression.

5. PARAMETERS USED IN EVALUATING ENERGY ABSORPTION STRUCTURES

Force/displacement performance parameters and energy absorption capacity measurements have been developed by a number of researchers. Magee and Thornton [51] used the peak buckling load and mean crush load to characterize the energy absorption of axially loaded square tubes that collapse in the symmetric mode. Mahmood and Paluszny [53] developed the concept of the crush force efficiency to compare the performance of energy absorbers of different shapes, sizes, and strengths. Different crush performance parameters are described in this section and will be used in the subsequent sections to characterize the force/displacement and energy absorption performances of the testing specimens.

5.1 Peak Buckling Load

The peak buckling load, P_{max} , is the maximum load experienced by the structure. The peak load transmitted through an energy absorbing structure should be minimized in order to minimize the peak deceleration occurring during crash situations.

5.2 Total Energy Absorption

The total energy absorbed by an extrusions is calculated as the work done by the crush force as described in equation (5.1).

$$E_{absorbed} = \int P \cdot d\delta \quad (5.1)$$

Where P is the crushing force and δ is the crosshead displacement both in the axial direction. During testing, data from the load cell along with the LVDT is used to develop the load versus crosshead displacement curve. For a finite number of data points, collected during the experimental process, the integration in equation (5.1) is replaced by the summation in equation (5.2)

$$E_{absorbed} = \sum_{i=2}^{N-1} P_i \left(\frac{\delta_{i+1} - \delta_{i-1}}{2} \right) \quad (5.2)$$

There are many different numerical integration schemes which can be used to evaluate equation (5.1). The scheme presented in equation (5.2) is the rectangular rule. Other schemes, such as trapezoidal rule or Simpson rules can also be used. In this research, equation (5.2) was used to calculate the energy absorbed.

5.3 Mean Crush Force

Based on the total energy absorption determined in equation (5.2), the mean crush force is defined as dividing equation (5.2) by the total crushing distance (δ_t) in the axial direction experienced by the specimen.

$$P_m = \frac{1}{\delta_t} \sum_{i=2}^{N-1} P_i \left(\frac{\delta_{i+1} - \delta_{i-1}}{2} \right) \quad (5.3)$$

5.4 Crush Force Efficiency

The crush force efficiency (*CFE*) is defined as the ratio of the average crushing force to the peak buckling load as shown in equation (5.4).

$$CFE = \frac{P_m}{P_{max}} \quad (5.4)$$

The most desirable situation would be a value of unity, corresponding to a square load versus crosshead displacement curve.

5.5 Specific Energy Absorption

The specific energy absorption (*SEA*) is defined as the energy absorbed by a structure divided by its mass as presented in equation (5.5). This is a useful quantitative

parameter, especially when comparing performances of energy absorbers with different mass and geometries.

$$SEA = \frac{E_{absorbed}}{m} \quad (5.5)$$

6. ANALYTICAL MODEL DEVELOPMENT AND COMPARISON WITH EXPERIMENTAL FINDINGS FOR ALUMINUM FOAM FILLED BRAIDED STAINLESS STEEL TUBE

A theoretical model which considers material properties (of both the braided tube and aluminum foam), tubular geometry, and deformation characteristics of the braided tube has been developed and is presented. Experimental observations by Altenhof and Powell [5], as reviewed in the appendix section, have indicated that the mechanical response of the foam filled braided tube is dependent upon the density and geometry of the aluminum foam core and the geometry of the braided stainless steel tube. The lightweight and corrosion resistance characteristics of both the aluminum foam and the braided stainless steel tubing as well as the deformation characteristics of the braided tube have been integrated to develop an energy absorbing device, which can be configured for specific applications where environmental and physical requirements may arise.

6.1 Braided Tube Kinematic Relationship between Elongation and Diameter

Experimental observations have illustrated that an important characteristic of energy absorption for the foam filled braided tube is related to the kinematic relationship between elongation and tube diameter. Elongation of the tube ends and the resulting change in diameter was observed not to cause any significant deformation of individual tows of the tube in the first stage of deformation, which included the radial crushing of aluminum foam core. The theoretical model used to express these characteristics is based on the unit cell concept. In a unit cell the diameter and the length are related to the angle between each crossing tow. Figure 6.1 illustrates the assumed unit cell superimposed onto a photograph of the braided tube. The local x - y coordinate system shown in Figure 6.1 originates on the face of the tube. The angle θ represents the angle between the assumed tows in the unit cell. In Figure 6.1 the x -axis direction is collinear to the axial direction of the tube and the y -axis is in the circumferential direction. The relationship

between tube radius and braid angle, considering the length of the unit cell along the circumference, is defined as:

$$l_y = 2 \cdot l \cdot \sin\left(\frac{\theta}{2}\right) \quad (6.1)$$

where l is the length of the unit cell measured along the tows. The number of unit cells on the circumference of the tube will remain constant, with the radius and angle between the tows changing as the tube elongates. The relationship between the initial (R_0) and current (R) tube radii and initial (θ_0) and current (θ) braid angles is given as:

$$\frac{R}{R_0} = \frac{\sin\left(\frac{\theta}{2}\right)}{\sin\left(\frac{\theta_0}{2}\right)} \quad (6.2)$$

Along the length of the tube, in the x -axis direction, the distance along the unit cell can be determined from equation (6.3).

$$l_x = 2 \cdot l \cdot \cos\left(\frac{\theta}{2}\right) \quad (6.3)$$

The relationship between the initial (L_0) and current (L) lengths of the braided tube and the initial (θ_0) and current (θ) braid angles is given as:

$$\frac{L}{L_0} = \frac{\cos\left(\frac{\theta}{2}\right)}{\cos\left(\frac{\theta_0}{2}\right)} \quad (6.4)$$

Initial variables that are known include the initial radius, the initial length of the tube, and the initial braid angle. From equations (6.1) through (6.4), changes to the radius and tube length can be calculated for any braid angle.

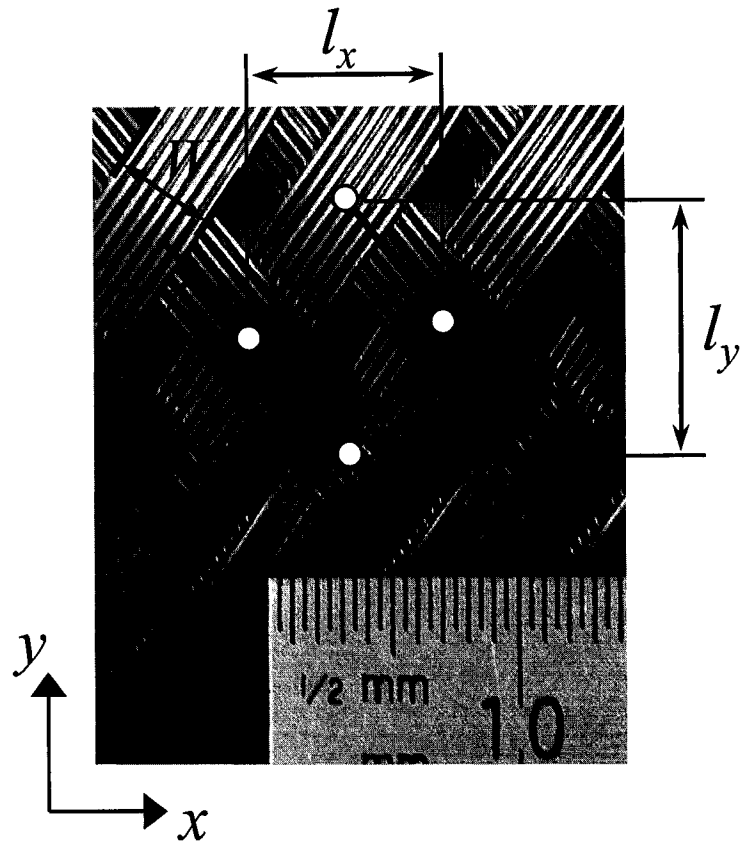


Figure 6.1. Unit cell geometry for theoretical model

In order to identify when the tows of the braided tube lock up, which is important in determining the contribution of energy absorbed by crushing of the interior foam core and by plastic deformation of the braided tube, the perpendicular distance (D) between the tows can be determined from equation (6.5).

$$D = l \cdot \sin(\theta) - W \quad (6.5)$$

In equation (6.5) W is the width of the tows which is the product of the number of wires within a tow and the wire diameter. Equation (6.5) can be rearranged to determine the locking angle θ_L from the constants l and W when the distance between the tows is zero.

$$\theta_L = \sin^{-1}\left(\frac{W}{l}\right) \quad (6.6)$$

For the braided tube that was used in the experiments, equation (6.6) was evaluated to determine the braid lockup angle under extension and compression which were calculated to be 38.35° and 141.65° respectively. Within the lockup angles (38.35° to 141.65°), different volumes of aluminum foam can be inserted within the tube. The volume of aluminum foam inserted in the tube can be dictated by the energy absorption requirements for a specific application.

6.2 Energy Absorbed by the Aluminum Foam Filled Braided Tube

In the proposed theoretical model the work done to deform the braided tube is equated to the energy absorbed by the structure. Experimental observations indicate that the energy absorbed by the aluminum foam filled braided tube consists of contributions from the crushing of the foam core and the elastic and plastic deformation of the braided tube, with the elastic component being recovered. In the proposed theoretical model, energy is absorbed as a result of foam crushing up to tube elongations which correspond to tow lockup. After tow lockup has occurred the energy absorbed by the structure is due to the elastic/plastic deformation of the braided tube only. It is assumed that the energy absorbed by the tow of braided tube while scissoring during foam core crushing (prior to tow lockup) is negligible. From these assumptions the total energy absorbed by the tube can be expressed as:

$$E_{total} = E_{foam} + E_{tube} \quad (6.7)$$

A discussion on the theoretical modeling for determining the energy absorbed by the aluminum foam core and the braided tube is completed in the following sections.

6.3 Energy Absorbed by the Aluminum Foam Core

The energy absorbed by the aluminum foam core was a result of radial compression by the braided tube during elongation prior to tow lockup. The contact area between the tube and the foam was assumed to be equal to the area of the lateral faces of the foam core. Experimental observations have illustrated that during crushing of the foam the braided tube conforms to the geometry of the prismatic foam core. It was also

observed that the foam core maintained a rectangular cross-section shape during crushing (prior to tow lockup). From these observations it was assumed in the theoretical model that the rectangular cross sectional shape of the core was maintained during crush and up to tow lockup. As well, the braided tube conforming to the cross sectional shape of the core implied that loading occurred on all lateral faces of the core.

Figure 6.2(a) and 6.2(b) illustrates assumed cross-section geometries of the foam filled braided tube prior to tube elongation and at tow lockup respectively. Figure 6.2(c) illustrates sections of length x and y which experience infinitesimal deformations dy and dx respectively, during foam crushing. Symmetry about the X and Y axes was applied to simplify the modeling process. The work, dU , associated with infinitesimal displacement dx under the action of a force acting on the lateral face of the foam core, F , can be expressed as:

$$dU_{foam} = F \cdot dx \quad (6.8)$$

The force acting upon the lateral faces of the foam core during radial crushing is the product of the foam plateau stress σ_{pl} and the contact area being $(L_{foam} \cdot y + L_{foam} \cdot x)$. To determine the total work required for the deformation process, from the initial tube geometry up to tow lockup, integration of equation (6.8) is completed as presented in equation (6.9).

$$U_{foam} = 4 \cdot \sigma_{pl} \cdot L_{foam} \left(\int_{\frac{W_{lockup}}{2}}^{\frac{W_0}{2}} x \cdot dy + \int_{\frac{W_{lockup}}{2}}^{\frac{W_0}{2}} y \cdot dx \right) \quad (6.9)$$

In the above equation, the total work done to crush the foam core was expressed as four times the work necessary to crush one quarter of the foam section. Based on the assumed square cross sectional shape, symmetry requires:

$$\int_{\frac{W_{lockup}}{2}}^{\frac{W_0}{2}} x \cdot dy = \int_{\frac{W_{lockup}}{2}}^{\frac{W_0}{2}} y \cdot dx \quad (6.10)$$

In the case of non-square, rectangular cross-sectional shapes, integration for each surface needs to be performed to determine the work done. Upon substituting equation (6.10)

into equation (6.9), the total work necessary to crush the foam core from its initial configuration up to tow lockup can be expressed as:

$$U_{foam} = 8 \cdot \sigma_{pl} \cdot L_{foam} \cdot \int_{\frac{W_{lockup}}{2}}^{\frac{W_0}{2}} x \cdot dy \quad (6.11)$$

Simplification of equation (6.11) gives:

$$U_{foam} = \sigma_{pl} \cdot L_{foam} \cdot (W_0^2 - W_{lockup}^2) \quad (6.12)$$

It is useful to express the work done to crush the foam as a function of instantaneous width, thus equation (6.13) presents the work done to crush the foam core as a function of foam width W .

$$U_{foam} = \sigma_{pl} \cdot L_{foam} \cdot (W_0^2 - W^2) \text{ where } W_0 \leq W \leq W_{lockup} \quad (6.13)$$

Equating the work done to crush the foam core to the energy absorbed by the foam finally gives the energy absorbed as a function of core width as expressed in equation (6.14).

$$E_{foam} = \sigma_{pl} \cdot L_{foam} \cdot (W_0^2 - W^2) \text{ where } W_0 \leq W \leq W_{lockup} \quad (6.14)$$

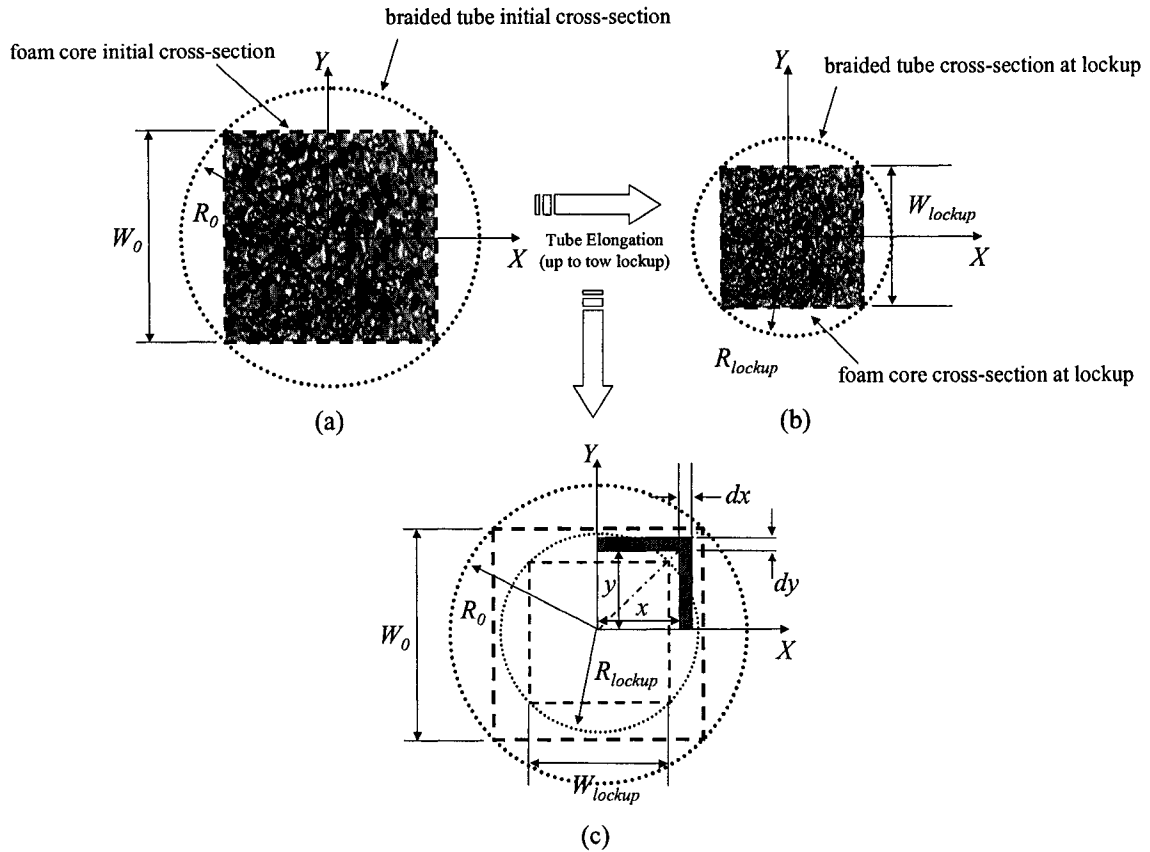


Figure 6.2. (a) assumed initial cross sectional shape of the foam filled tube, (b) assumed cross sectional shape of the foam filled tube at tow lockup, and (c) theoretical model illustrating deformation of one quarter of the foam core.

6.4 Energy Absorbed by the Braided Tube

The braided tube will not contribute to energy absorption until tow lockup. After lockup occurs, tows of braided tube will undergo plastic deformation due to extension. According to experimental observations, the force/displacement behaviour of the braided tube can be divided into two distinct regions as presented in Figure 6.3. A linear approximation in both regions was used to simplify the calculation of the energy absorption capabilities of the braided tube. In each region, a different stiffness was used to represent the force/displacement relationship. The energy absorption for Region 1 can be determined from the product of the stiffness of the tube, k_I , and the change in length of

the tube (z) as presented in equation (6.15). In equation (6.15) L_{lockup} is the tube length at lockup which can be calculated through application of equation (6.4).

$$E_1(z) = \frac{1}{2} \cdot k_1 \cdot (z - L_{lockup})^2 \quad (6.15)$$

The stiffness in Region 1 was evaluated from a least squares regression of the force/displacement relationship of an empty tube under tensile loading up the end of Region 1. The corresponding force/displacement relationship is presented in equation (6.16).

$$F_1(z) = k_1 \cdot (z - L_{lockup}) \quad \text{with} \quad k_1 = 3.2 \cdot \frac{\text{kN}}{\text{mm}} \quad (6.16)$$

A linear regression was also completed for the force/displacement relationship in Region 2 based upon the experimental findings from the 185 mm length tube. The force displacement relation is expressed in equation (6.17).

$$F_2(z) = k_2 \cdot (z - L_{lockup}) + f_2 \quad (6.17)$$

$$\text{with} \quad k_2 = 0.194 \cdot \frac{\text{kN}}{\text{mm}} \quad f_2 = 34.442 \cdot \text{kN}$$

Experimental observations have illustrated that tube length had no significant influence on the stiffness of Region 1. For region 2, however, an inverse relationship between tube length and stiffness was observed as presented in equation (6.18). In equation (6.18), k_2 and L represent the stiffness in Region 2 for the tube with length of the 185 mm and k_2' and L' represent the stiffness in Region 2 for any tube of length other length than 185 mm.

$$\frac{k_2}{k_2'} = \frac{L'}{L} \quad (6.18)$$

The length of the braided tube prior to assembly was 610 mm. The stiffness in Region 2 of this tube was calculated to be 58.8 N/mm, hence the force displacement relationship in Region 2 for the aluminum foam filled tube of length equal to 406 mm is:

$$F_2' = k_2' \cdot (z - L_{lockup}) + f_2 \quad (6.19)$$

$$\text{with} \quad k_2' = 58.8 \cdot \frac{\text{N}}{\text{mm}} \quad f_2 = 34.442 \cdot \text{kN}$$

The abscissa value corresponding to the intersection point of the linear force/displacement relationships for Region 1 and Region 2 can be easily obtained through equation (6.20).

$$z = L_{crit} = \frac{f_2}{k_1 - k_2'} + L_{lockup} \quad (6.20)$$

The energy absorbed in Region 1 due to tube deformation can be expressed as presented in equation (6.21).

$$E_{tube}(z) = \frac{F_1(z) \cdot (z - L_{lockup})}{2} \quad \text{with} \quad L_{lockup} \leq z \leq L_{crit} \quad (6.21)$$

The energy absorbed due to tube deformation in Region 2 is expressed in equation (6.22).

$$E_{tube}(z) = E_{tube}(L_{crit}) + \frac{(F_2'(L_{crit}) + F_2'(z)) \cdot (z - L_{crit})}{2} \quad (6.22)$$

with $L_{crit} < z$

Total energy absorption of aluminum foam filled braided tube is then determine through equation (6.7).

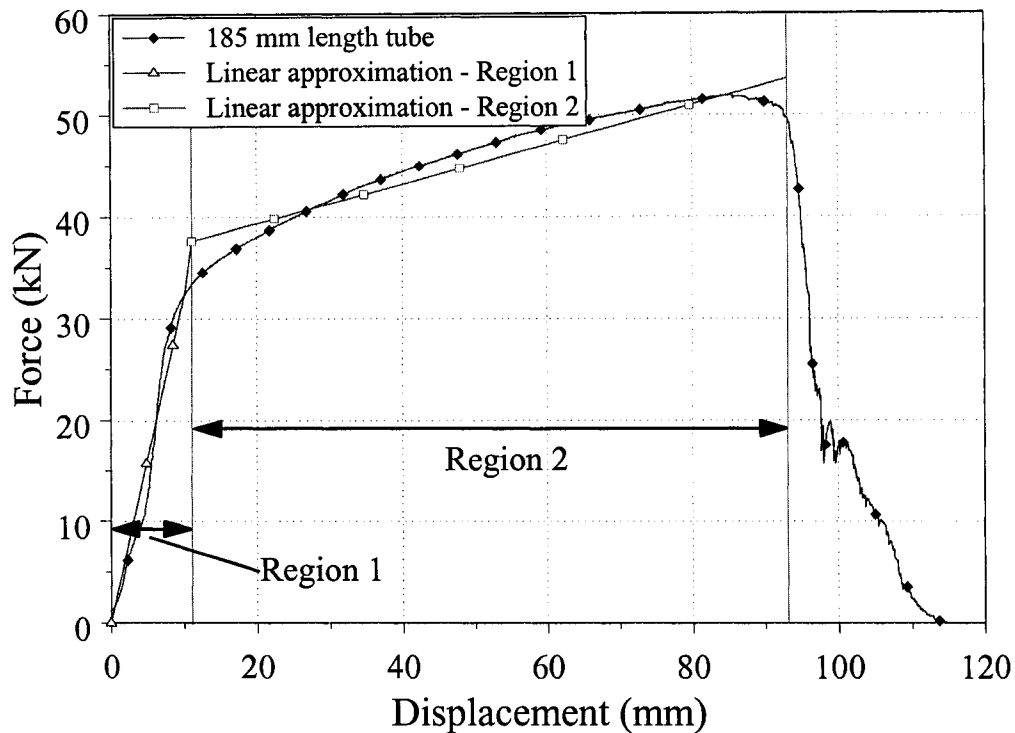


Figure 6.3. Force/displacement behaviour of an empty braided tube with linear approximations in Region 1 and Region 2.

6.5 Results and Discussion

The energy absorption prediction using the theoretical model and the observed experimental energy absorption is illustrated in Figure 6.4. Good predictive capabilities of the theoretical model are observed with a stronger correlation observed in the initial stages of tube deformation. For all displacement values the theoretical model over predicts the energy absorption capabilities of the foam filled braided tube. Prior to tow lockup, at approximately 230 mm crosshead displacement, experimental and theoretical values of the energy absorbed are within 25% error. Possible reasons for higher energy absorption in the theoretical model could be attributed to the lack of consideration of braid slippage, and tensile foam fracture which was observed experimentally.

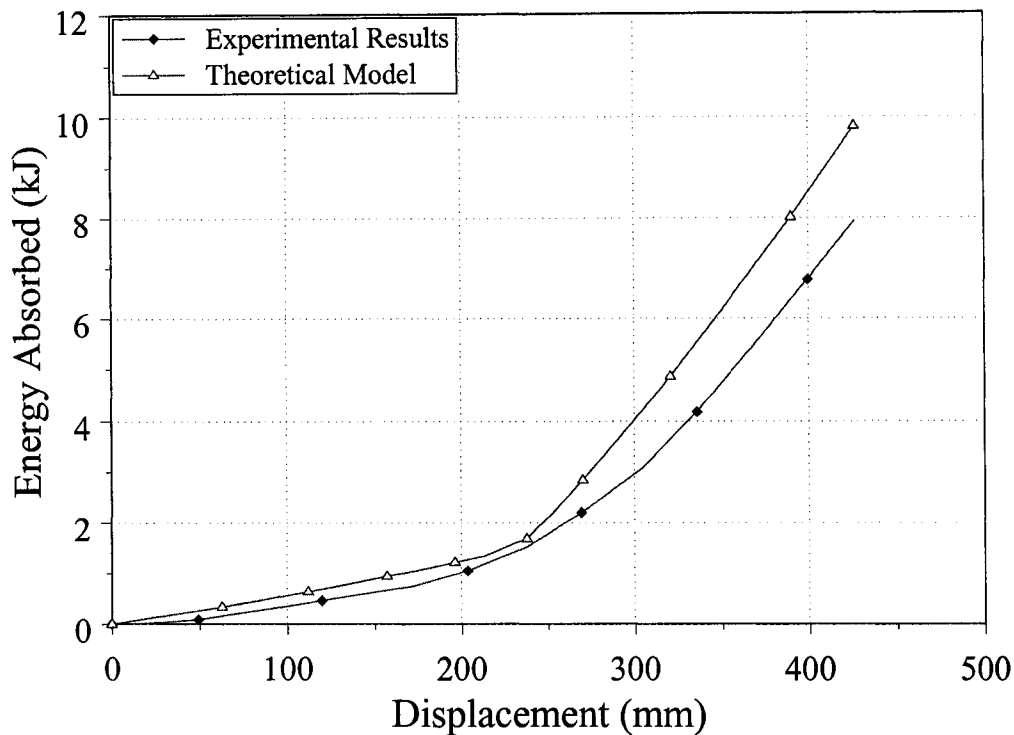


Figure 6.4. Energy/displacement behaviour of from experimental observations and the theoretical model.

After tow lockup the theoretical model predicts a rapid increase in energy absorption while experimental observations indicate that the increase in energy absorption after tow lockup is less severe. Experimental observations showed that a transition region for the force/displacement (and hence energy absorbed/displacement) behaviour of the foam filled tube (stage 2 in Figure A.2 through Figure A.5 as presented in Appendix A) occurred over a finite crosshead displacement during tow lockup. The theoretical model assumes that the energy absorption of the foam filled tube immediately switches from a “foam crushing stage” to a “braided tube plastic deformation stage”; in the theoretical model no form of transition is taken into consideration for the energy response of the structure. A maximum value of the percentage error after tow lockup was found to be approximately 23%.

7. EXPERIMENTAL RESULTS AND DISCUSSION FOR QUASI-STATIC AXIAL COMPRESSIVE CRUSHING AND CUTTING TESTS

The results of the experimental testing conducted for this research are presented in different sections of this chapter. An overview is given in the first section for the results of the tensile tests which were conducted by Arnold [12] to obtain material properties for the aluminum extrusions. The second section details the results of the quasi-static crush testing of the extrusion specimens. The third section compares the results of the crush test between specimens.

7.1 Extrusion Material Property Tensile Testing Results

The engineering stress/strain curve of one representative AA6061-T6 tensile specimen is illustrated in Figure 7.1. Material properties of the AA6061-T6 are summarized in Table 7.1.

Table 7.1. Material properties from extrusion tensile tests [12]

Properties	AA6061-T6
E (GPa)	68.1
σ_y (MPa)	277.5
σ_u (MPa)	320.2
% elongation	14.1

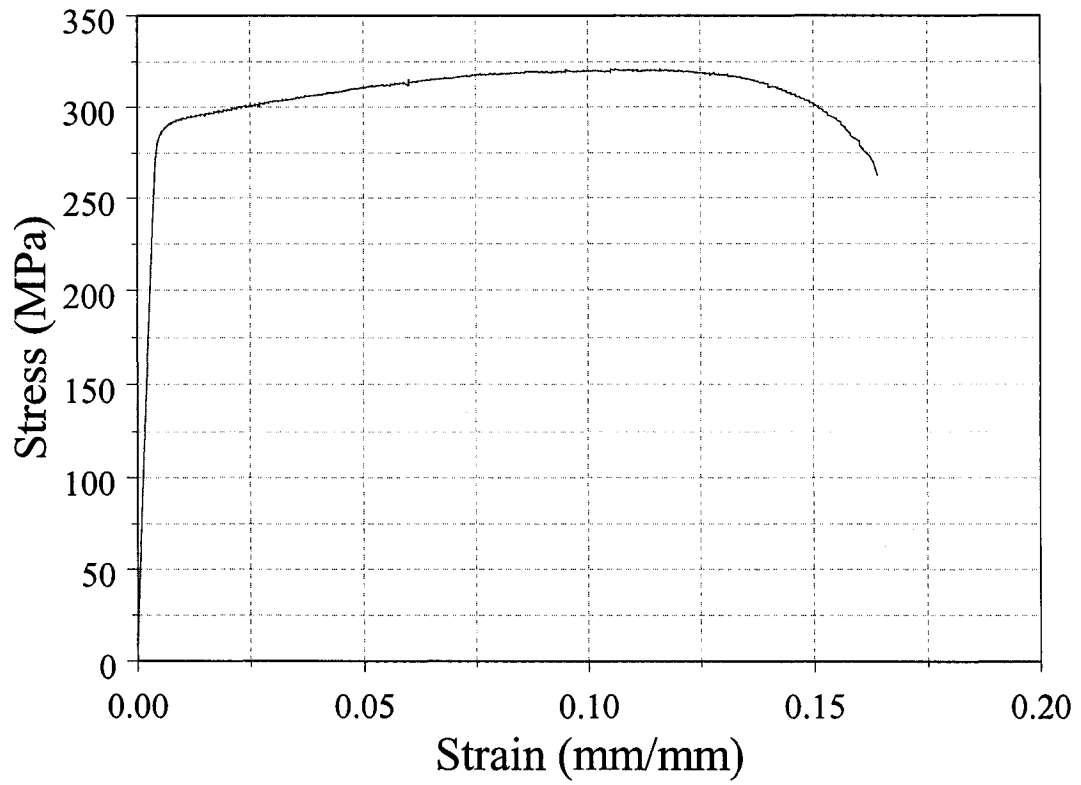


Figure 7.1. Engineering stress-strain curve of AA6061-T6 obtained from tensile testing [12].

7.2 Quasi-Static Axial Compressive Crush Testing Results and Discussion

Although four tests were completed for each sub-group the load/displacement observations for all specimens within a sub-group were fairly consistent with a scatter of less than $\pm 4\%$. For this reason, and for greater clarity, only the mean values of the crush parameters are presented for each sub-group and are used for comparison and discussions. The calculated mean results of the crush parameters for each sub-group are presented in Table 7.2. For each specimen, a qualitative and quantitative examination of the crush testing observations was completed through analysis of photographs and the load/displacement results for crosshead displacements up to 100 mm.

7.2.1 Crush Test Results for Specimens in Group 1 and Group 2

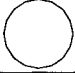
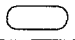


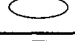

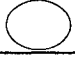

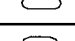

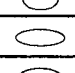
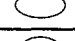


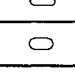
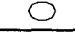
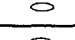
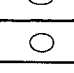



Load/displacement observations from representative specimens containing the circular discontinuities (C2, C3, and C4) and Group 1 are illustrated in Figure 7.2. Figure 7.3 and Figure 7.4 illustrate the load/displacement relationships observed for Group 2 containing the slotted and elliptical discontinuities respectively. For comparison purposes the testing observations from Group 1 are also presented in Figure 7.3 and Figure 7.4. An examination of the observed load/displacement profiles in these figures clearly illustrates that specimen W0, without any discontinuity, obtained the highest peak buckling load of 124.7 kN. After reaching the peak buckling load, the resistance force exerted by the structure decreased rapidly as a result of the formation of a single plastic hinge and material cracking, which resulted in low energy absorption. For specimens in Group 2 the influence of geometrical discontinuity was significant. Relative to experimental observations from Group 1, lower peak buckling loads, higher total energy absorption, higher post-buckling resistance force and a splitting/tearing deformation mode were observed for specimens in Group 2. It was also observed that with the presence of a circular discontinuity, the linear portion of the load/displacement profiles decreased, in the displacement domain, as the major axis length increased for circular discontinuities. For slotted and elliptical geometrical discontinuities a similar decrease was observed, however, there was no dependency on aspect ratio for each sub-group.

Furthermore, the transition region between initiation of plastic buckling and the onset of local collapse was shorter for specimens which contained discontinuities. The transition region appeared to be dependent upon the aspect ratio associated with each sub-group for the same geometrical discontinuity.

Specimen C2, which had a circular discontinuity of diameter 14.29 mm, had the lowest peak buckling load of 101.3 kN amongst all specimens in this investigation. Specimens with slotted and elliptical geometrical discontinuities illustrated a direct relationship between aspect ratio and energy absorption. Specifically, a higher post-buckling resistance force, and hence greater energy absorption, was observed for specimens with these geometries which possessed large aspect ratios. A comparison of the energy absorption performances for specimens in Group 2 indicates that the slotted discontinuity is most favourable, followed by the elliptical and circular holes.

As noted by Arnold and Altenhof [12], splitting and tearing deformation modes referred as mode SMI and mode SMII existed for as-received AA6061-T6 aluminum extrusions under axial compression loading conditions. In mode SMI after initial plastic deformation in the vicinity of the discontinuity, material cracking initiated on either side of the hole, followed by a lateral shift of the top half of the tube relative to the bottom half. As the crushing process continued, the top half portion of the specimen cut through the bottom portion. In deformation mode SMII plastic deformation around the discontinuity area caused material cracking to occur at the edge of the sidewalls rather than at the hole boundary as in SMI. In splitting mode SMII the top half was driven through the bottom portion without any significant form of lateral shift causing material cracking in the corner of both the top and bottom portions with a minor extent of progressive folding observed for the sidewalls. Deformation modes SMI, SMII and global bending were observed in this investigation as presented in Table 7.2. Photographs illustrating the deformation modes of specimens in Group 1 and Group 2 are illustrated in Figure 7.5.

Table 7.2. Experimental testing results

Group #	Sub-group identifier	Shape	$E_{absorbed}$ (kJ)	P_{max} (kN)	P_m Force(kN)	CFE (%)	SEA (kJ/kg)	Deformation mode
1	W0	w/o	3.35	124.7	33.21	26.6	14.11	Global bending
2	C2		4.36	101.3	43.12	42.6	18.53	SMI
	S2-3		5.73	108.9	56.72	52.1	24.20	SMII
	S2-2		4.44	102.1	43.98	43.1	18.80	SMI
	S2-1		4.31	102.1	42.63	41.8	18.27	SMI
	E2-3		5.30	108.7	52.51	48.3	22.65	SMII
	E2-2		4.27	102.3	42.31	41.4	18.39	SMI
	E2-1		4.24	102.3	42.02	41.1	18.48	SMI
3	C3		4.36	109.4	43.16	39.5	18.45	SMII
	S3-3		5.27	112.6	52.05	46.2	22.16	SMII
	S3-2		5.85	111.3	57.92	52.0	24.69	SMII
	S3-1		4.66	109.6	46.10	42.1	19.68	SMII
	E3-3		5.78	113.7	57.27	50.4	24.53	SMII
	E3-2		4.61	109.5	45.67	41.7	19.65	SMII
	E3-1		4.58	108.1	45.37	42.0	19.65	SMII
4	C4		5.56	117.1	55.00	47.0	23.43	SMII
	S4-3		5.13	118.2	50.80	43.0	21.60	SMII
	S4-2		5.23	116.8	51.80	44.3	22.01	SMII
	S4-1		4.89	117.7	48.43	41.1	20.62	SMII
	E4-3		4.39	116.3	43.48	37.4	18.54	SMII
	E4-2		5.30	115.6	52.50	45.4	22.41	SMII
	E4-1		4.94	114.5	48.88	42.7	20.94	SMII

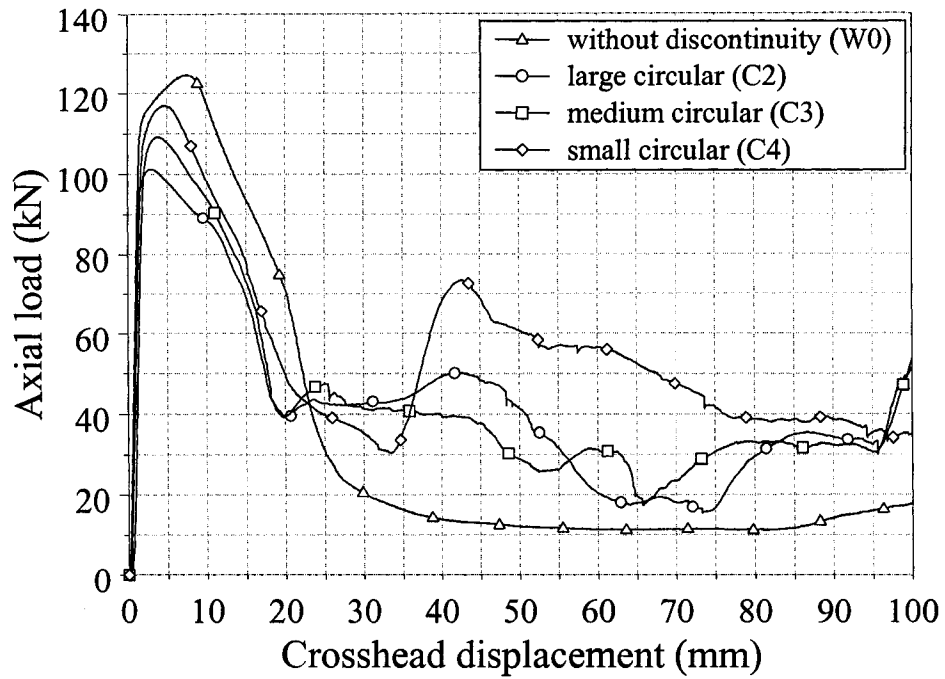


Figure 7.2. Experimental obtained load/displacement profiles for specimens with circular discontinuities and specimen without discontinuity.

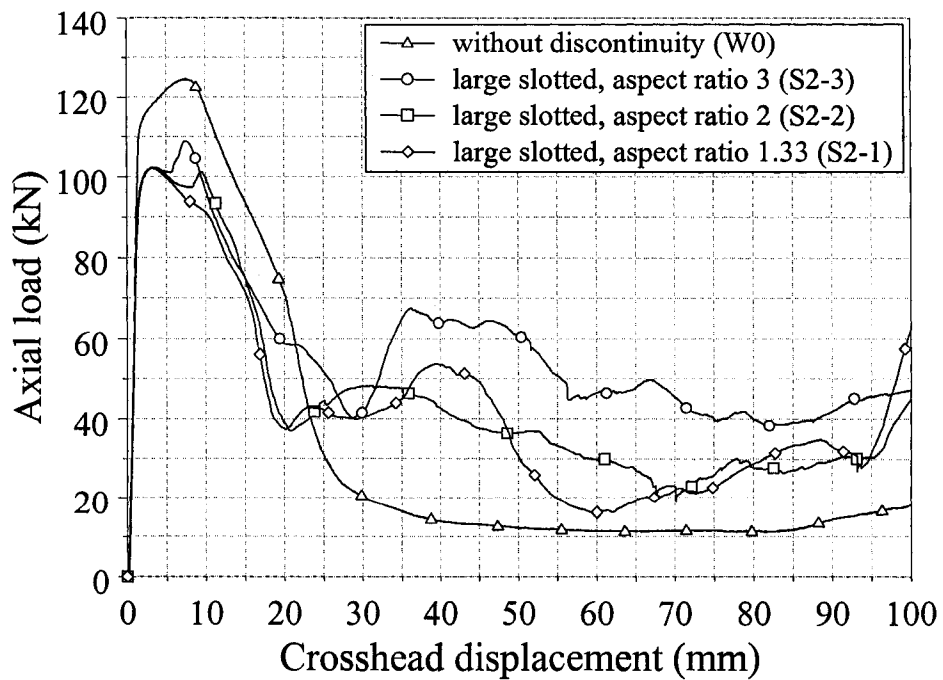


Figure 7.3. Experimental obtained load/displacement profiles for specimens with large slotted discontinuities and specimen without discontinuity.

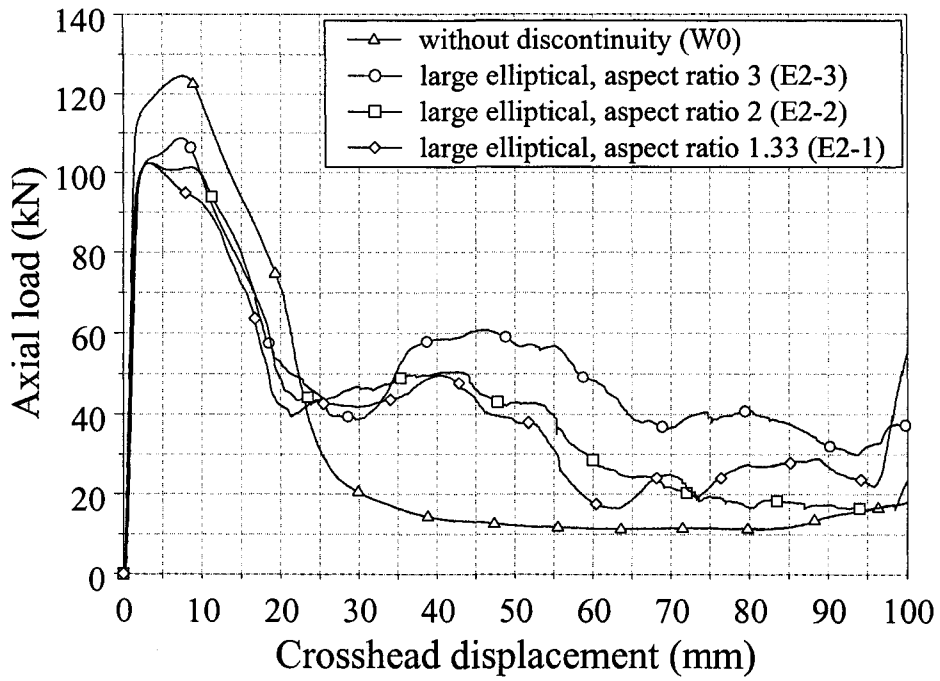


Figure 7.4. Experimental obtained load/displacement profiles for specimens with large elliptical discontinuities and specimen without discontinuity.

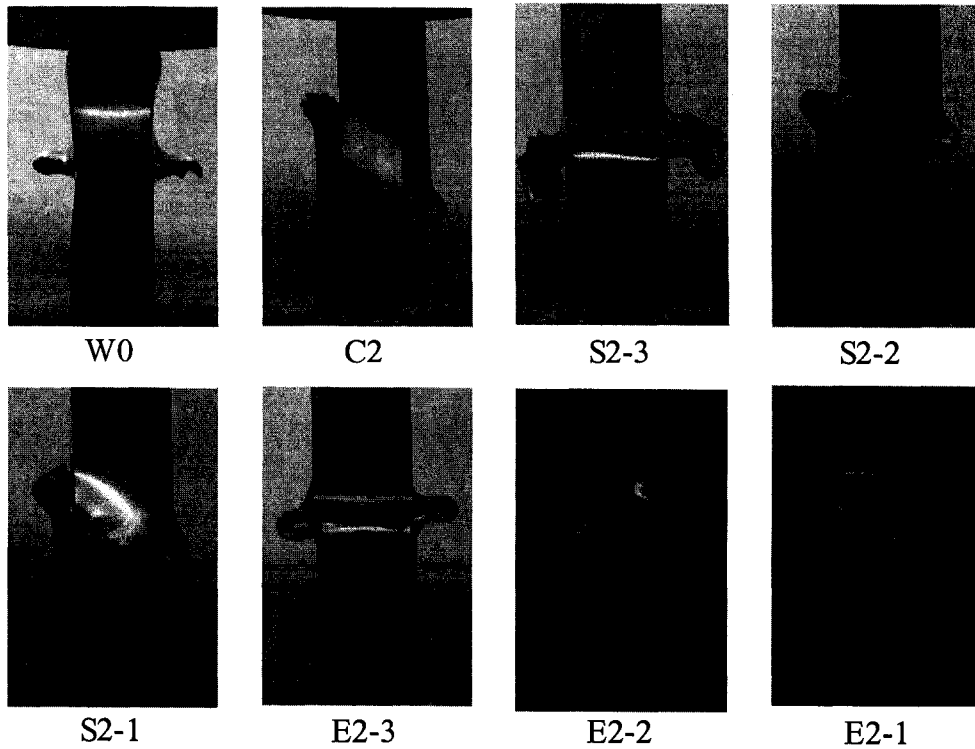


Figure 7.5. Deformation modes observed for specimens in Group 1 and Group 2, W0 in global bending, C2, S2-2, S2-1, E2-2 and E2-1 in SMI, S2-3 and E2-3 in SMII.

7.2.2 Crush Test Results for Specimens in Group 3

Observed load/displacement relationships for specimens in Group 3 are illustrated in Figure 7.6 and Figure 7.7 for medium slotted and elliptical discontinuities respectively with observations from specimen W0 also presented. Photographs illustrating the deformation from representative specimens in Group 3 are presented in Figure 7.8. All specimens in Group 3 collapsed in SMII mode. Specimen C3, with a circular discontinuity, and S3-1, with a slotted discontinuity of aspect ratio 1.33, displayed more cracking along the edge of the sidewalls. The remaining specimens in this group displayed a more stable deformation process with the continuous folding of split sidewalls. Specimen S3-2, which had a slotted discontinuity of aspect ratio 2, experienced the highest energy absorption of 5.85 kJ amongst all specimens. Specimen C3, which has a circular discontinuity, experienced the lowest energy absorption of 4.36 kJ in Group 3. The stability of the crush process and the accompanying energy absorption was observed to be higher for specimens within Group 3 which had larger aspect ratios.

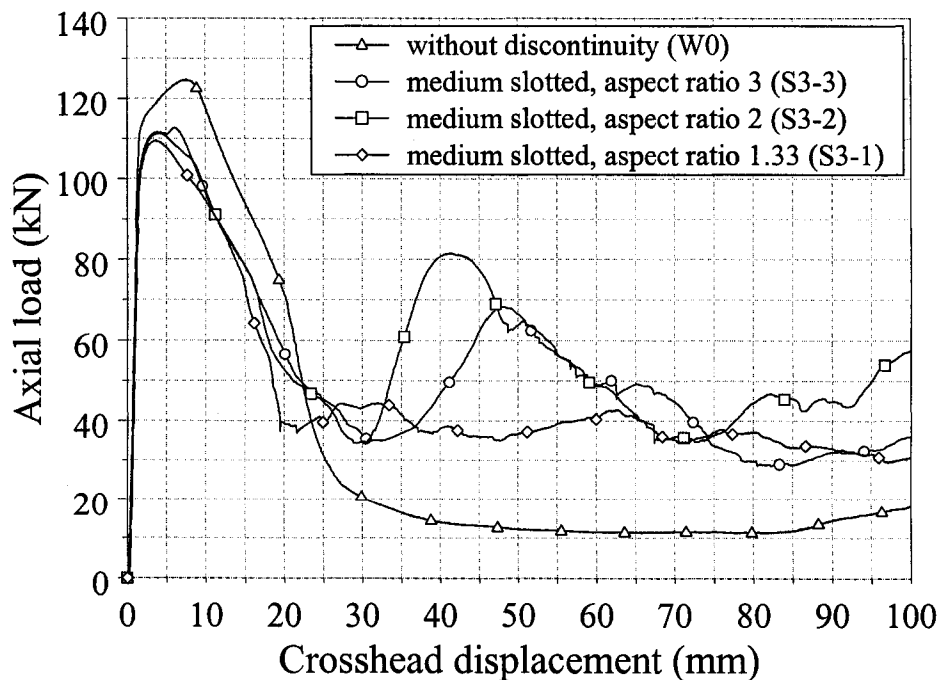


Figure 7.6. Experimental obtained load/displacement profiles for specimens with medium slotted discontinuities and specimen without discontinuity.

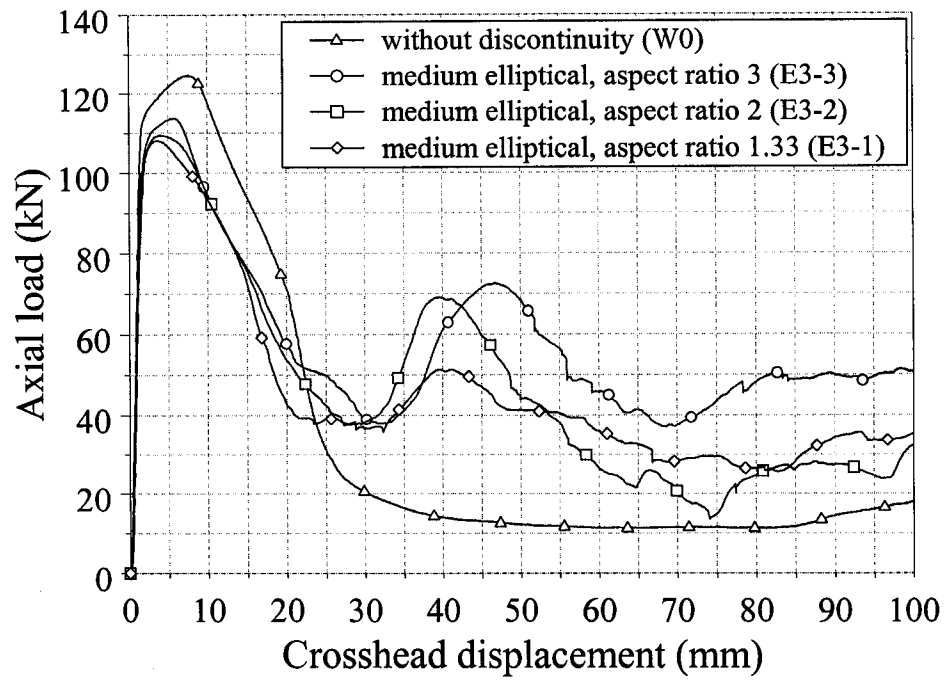


Figure 7.7. Experimental obtained load/displacement profiles for specimens with medium elliptical discontinuities and specimen without discontinuity.

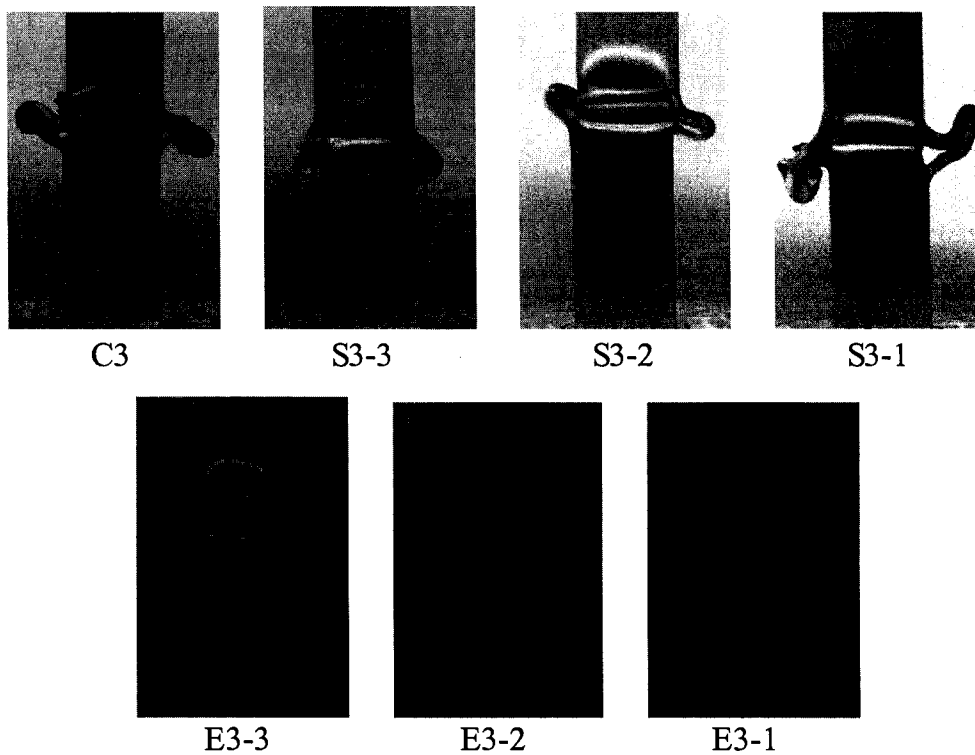


Figure 7.8. Deformation modes of specimens in Group 3. All specimens deformed in SMII mode.

7.2.3 Crush Test Results for Specimens in Group 4

Load/displacement observations for specimens in Group 4 are illustrated in Figure 7.9 and Figure 7.10 for small slotted and elliptical discontinuities respectively with observations from specimen W0 also presented. The crush deformation associated with representative specimens from this group are presented in Figure 7.11. Specimen C4, which had a circular discontinuity, exhibited the largest energy absorption at 5.56 kJ. Specimen E4-3, which had an elliptical discontinuity of aspect ratio 3, exhibited some variations in its deformation behaviour. Two specimens of this geometry deformed in the global bending mode, and the other two specimens deformed in the splitting and cutting mode SMII. It can be seen from Figure 7.9 and 7.10 that specimens with circular, slotted and elliptical discontinuities with small major axis lengths displayed highly similar force/displacement relationships.

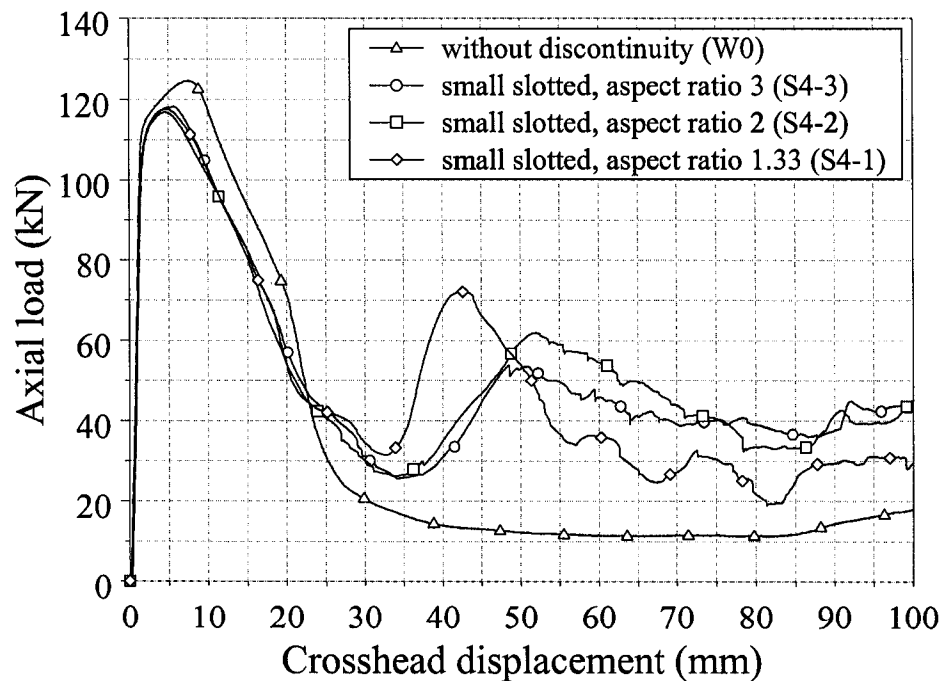


Figure 7.9. Experimental obtained load/displacement profiles for specimens with small slotted discontinuities and specimen without discontinuity.

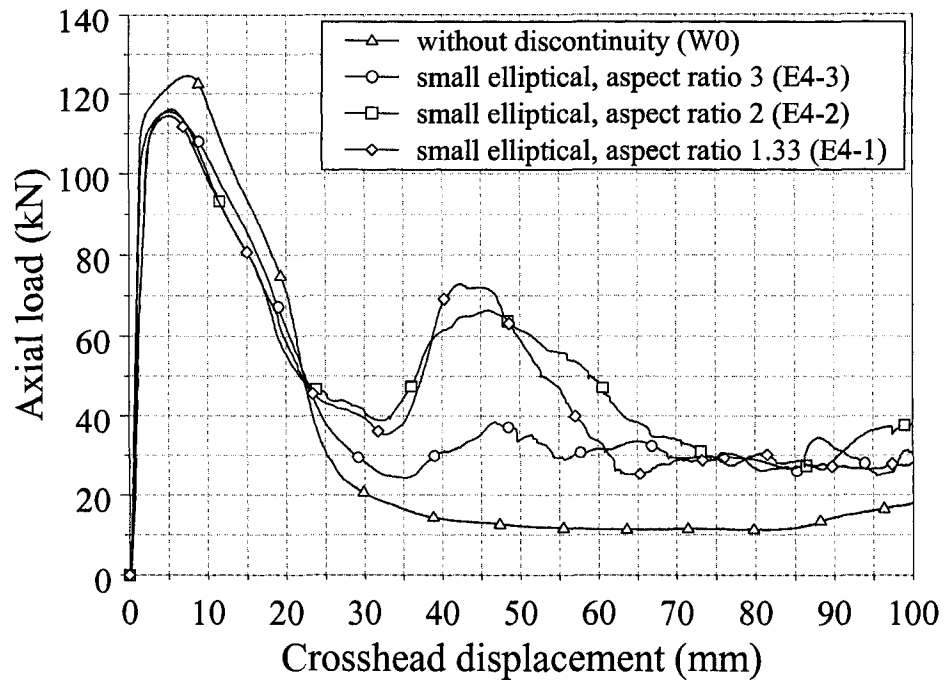


Figure 7.10. Experimental obtained load/displacement profiles for specimens with small elliptical discontinuities and specimen without discontinuity.

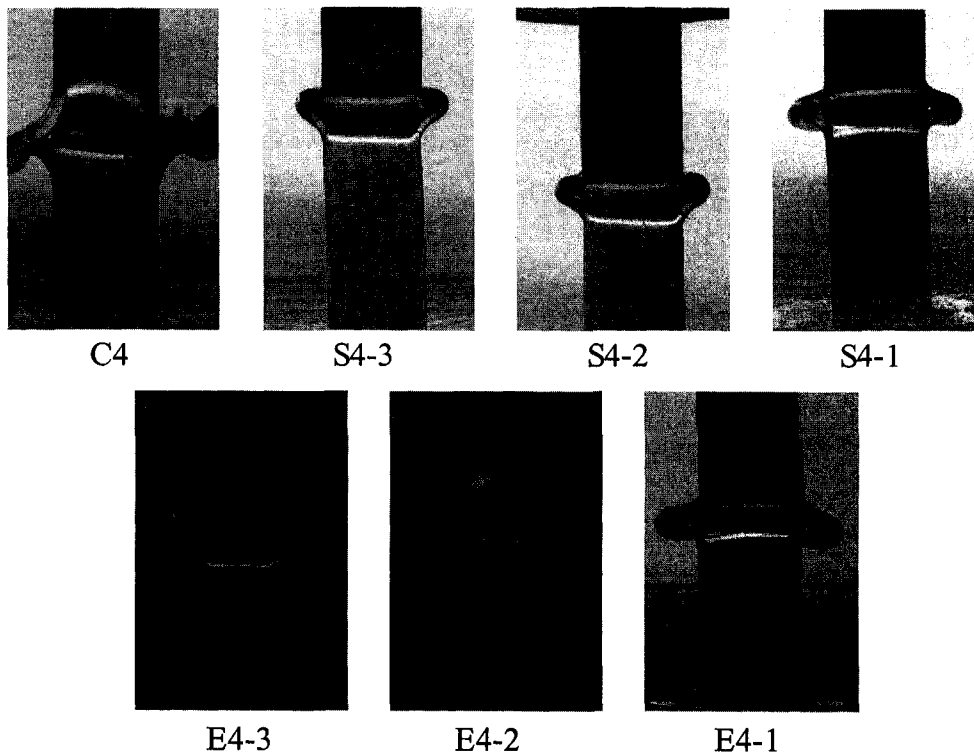


Figure 7.11. Deformation modes of specimens in Group 4. All specimens deformed in SMII mode.

7.2.4 Relationships Between Force/Displacement Profiles and Deformation

A qualitative comparison of the force/displacement profiles and the corresponding deformation modes for a limited number of representative specimens from groups and sub-groups are presented. Slotted and elliptical specimens with a major axis length of 10.72 mm and an aspect ratio of 2 were selected for comparison. In addition to these specimens, extrusions with no discontinuities and a circular through hole with a diameter of 10.72 mm were also compared. The selected specimens for comparison were chosen due to the common major axis length and aspect ratio which are the average of the smallest and largest major axes lengths considered.

7.2.4.1 Specimens without Any Discontinuities (Group 1)

All specimens in this group collapsed in the same global bending mode and had similar load versus displacement relationships. A force/displacement profile from a representative specimen from Group 1 is shown in Figure 7.12 annotated with labels corresponding to the photographs illustrating the deformation process presented in Figure 7.13.

Due to the lower strain hardening and reduced ductility associated with the T6 heat treatment, cracking occurred at the corners and along the edges of the side walls of the tube during the crushing process. As the bending of the specimen progressed, the plastic strain at the edges of the sidewalls in the kinked region of the tube exceeded the failure strain of the material.

Point (a) in Figure 7.12 and the deformation presented in Figure 7.13(a) correspond to the peak buckling load and the initiation of collapse of the specimen. Point (b) in Figure 7.12 (corresponding to the deformation presented in Figure 7.13(b)) illustrates the instant at which cracking was observed to begin at the corner of the tube. As showed in Figure 7.12, the occurrence of cracking coincided with a significant drop of the load bearing capacity of the extrusion at approximately 20 mm crosshead displacement. The load bearing capacity of the specimen continued to decrease until

contact occurred between the top and bottom sides of the extrusion measured at the plastic hinge, which occurred at a crosshead displacement of approximately 50 mm.

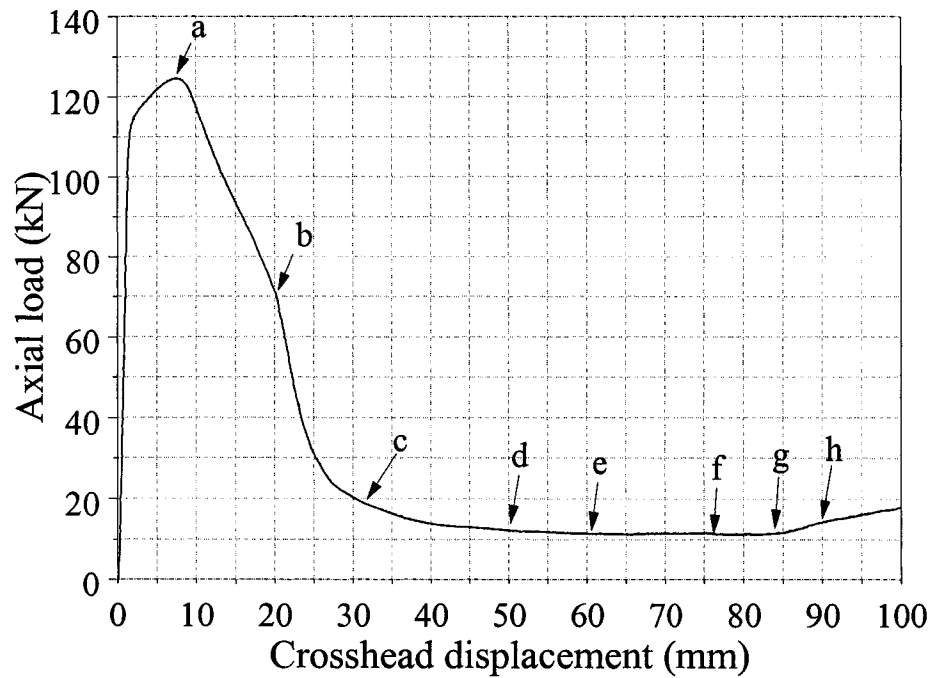


Figure 7.12. Experimentally obtained load versus displacement profile for a specimen without any discontinuity.

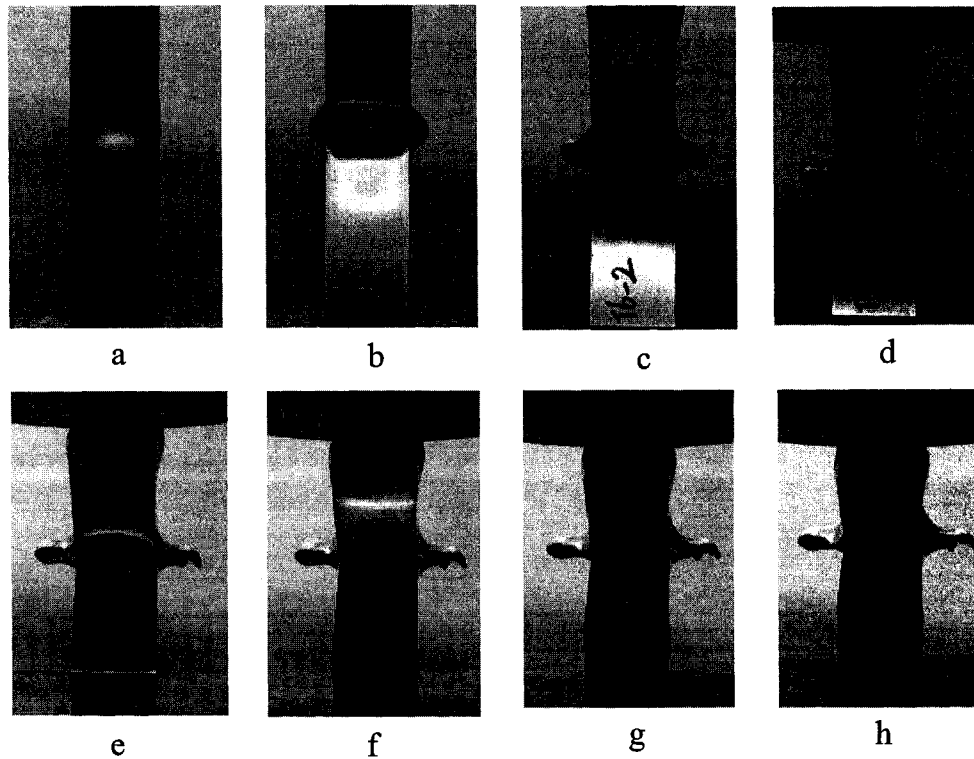


Figure 7.13. Photographs illustrating the crushing process for a specimen without any discontinuity.

7.2.4.2 Specimens in Sub-group C3

Specimens in this sub-group had circular discontinuities with a diameter of 10.72 mm and all deformed in SMII mode. The observed load/displacement profile for a representative specimen from this sub-group is presented in Figure 7.14 with annotations referring to the deformation photographs presented in Figure 7.15. Point (a) in Figure 7.14 (corresponding to the deformation presented in Figure 7.15(a)) marked the peak buckling load, in which significant deformation was visually observed on the perimeter of the discontinuity. As the crushing process continued, the material deformation became larger in the vicinity of the hole. The discontinuities on either side of the specimen collapsed (Figure 7.15(b)) followed by the formation of a fold on both side walls (Figures 7.15(c) and 7.15(d)) which did not contain the discontinuities. Following the formation of the folds, cracking and tearing along the corners of the extrusion initiated (Figure 7.15(d)) and progressed through the specimen in the vicinity of the corners of the tube

(Figures 7.15(e) through 7.15(h)). The load/displacement profile became constant at the approximate instant when cracking initiated at the corners of the extrusions (Figure 7.15(d)).

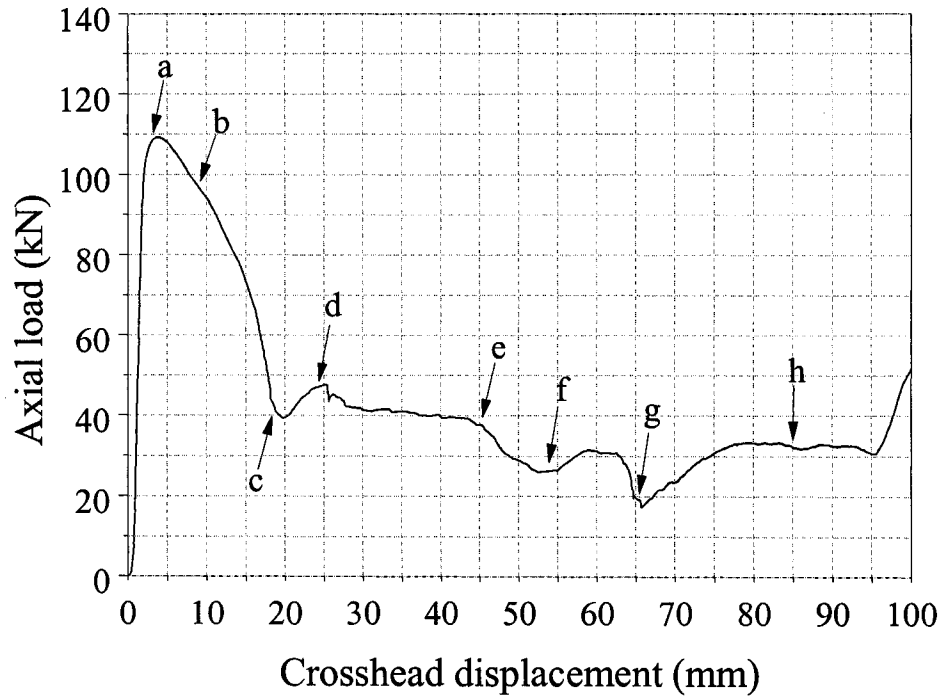


Figure 7.14. Experimentally obtained load versus displacement profile for a representative specimen from sub-group C3.

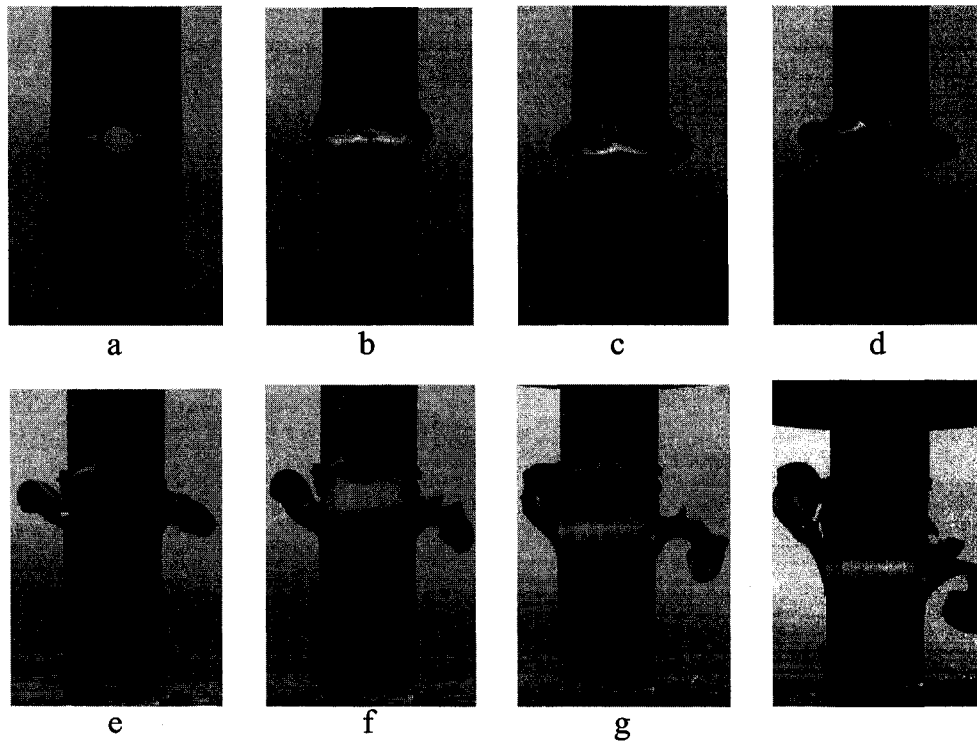


Figure 7.15. Photographs illustrating the crushing process for a representative specimen from sub-group C3.

7.2.4.3 Specimens in Sub-group S3-2

Specimens in this sub-group had slotted discontinuities with a major axis length of 10.72 mm and an aspect ratio of 2. All specimens in this sub-group collapse under SMII mode with a noticeably greater translation of the upper half of the extrusion, relative to the lower portion, than was observed for specimen C3. In addition, a greater amount of sidewall folding and a lower degree of material splitting was observed for specimens in sub-group S3-2 than specimen C3. An annotated load/displacement profile for a representative specimen from sub-group S3-2 and the corresponding photographs illustrating the deformation process are presented in Figure 7.16 and Figure 7.17 respectively. Point (a) in Figure 7.16 (corresponding to the deformation presented in Figure 7.17(a)) marked the peak buckling load of 111.3 kN. Point (e) corresponded to the force and displacement after the formation of a single fold. After point (e) no observable formation of sidewall folding was noted, however, significant material

splitting and cracking was observed which corresponded to a load/displacement profile with no significant oscillations.

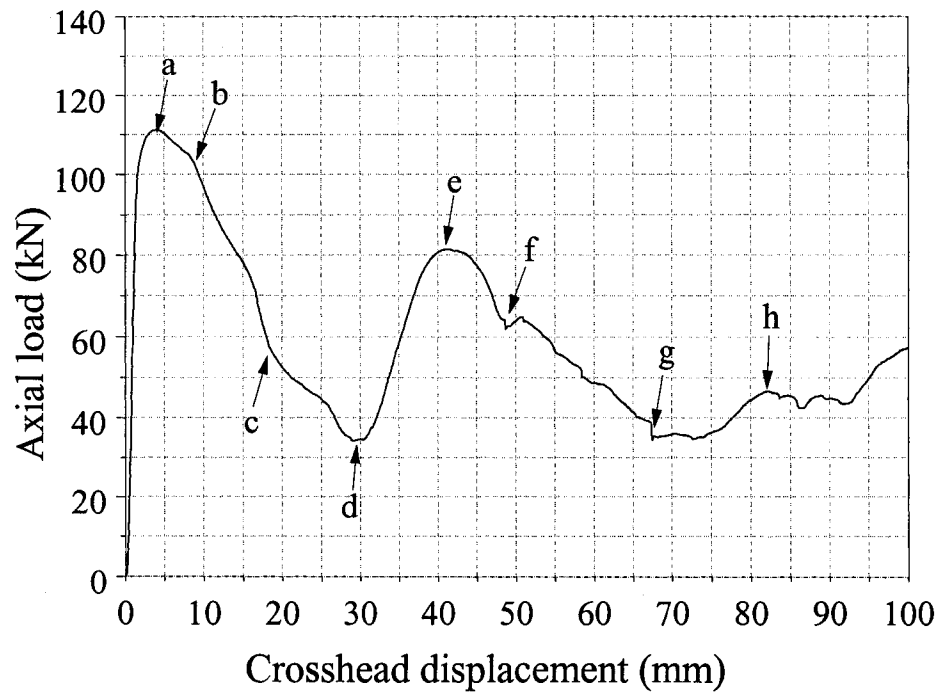


Figure 7.16. Experimentally obtained load versus displacement profile for a representative specimen from sub-group S3-2.

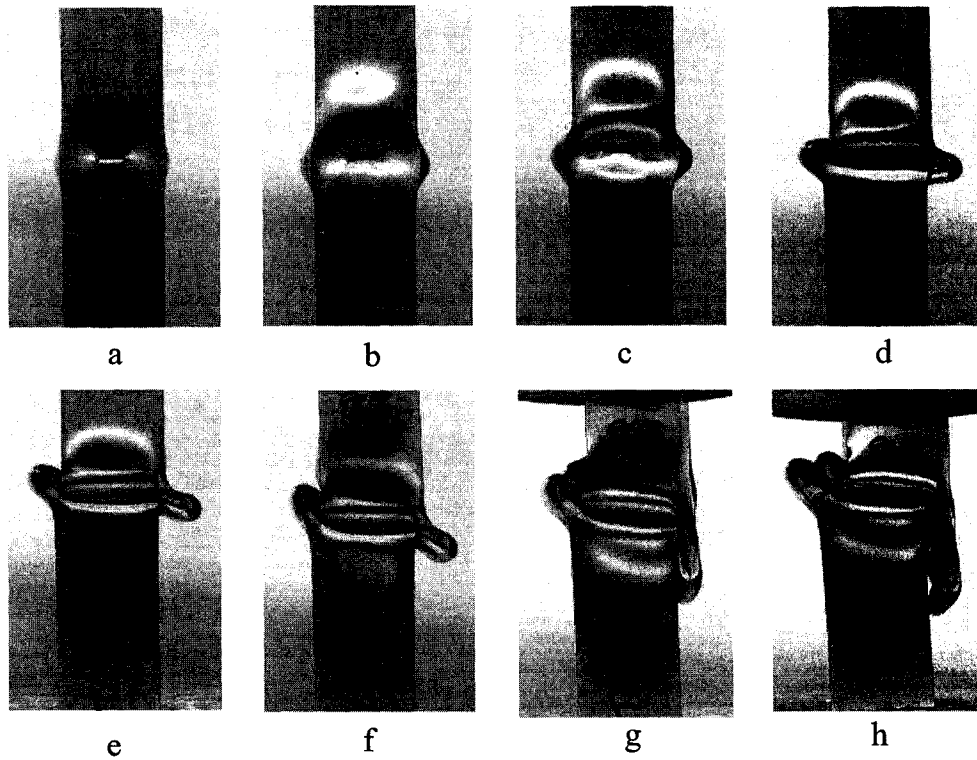


Figure 7.17. Photographs illustrating the crushing process for a representative specimen from sub-group S3-2.

7.2.4.4 Specimens in Sub-group E3-3

Specimens in this sub-group had elliptical discontinuities with a major axis length of 10.72 mm and an aspect ratio of 3.0. The deformation process of specimens from sub-group E3-3 was observed to be very similar to specimens from sub-group S3-2. Annotated load/displacement profiles and corresponding photographs illustrating the crushing process are presented in Figure 7.18 and Figure 7.19 respectively. During the deformation process a single lobe was formed after a crosshead displacement of approximately 48 mm for a representative specimen in sub-group E3-3. For comparison purposes, the formation of a single lobe for a representative specimen in sub-group S3-2, occurred after a crosshead displacement of approximately 42 mm.

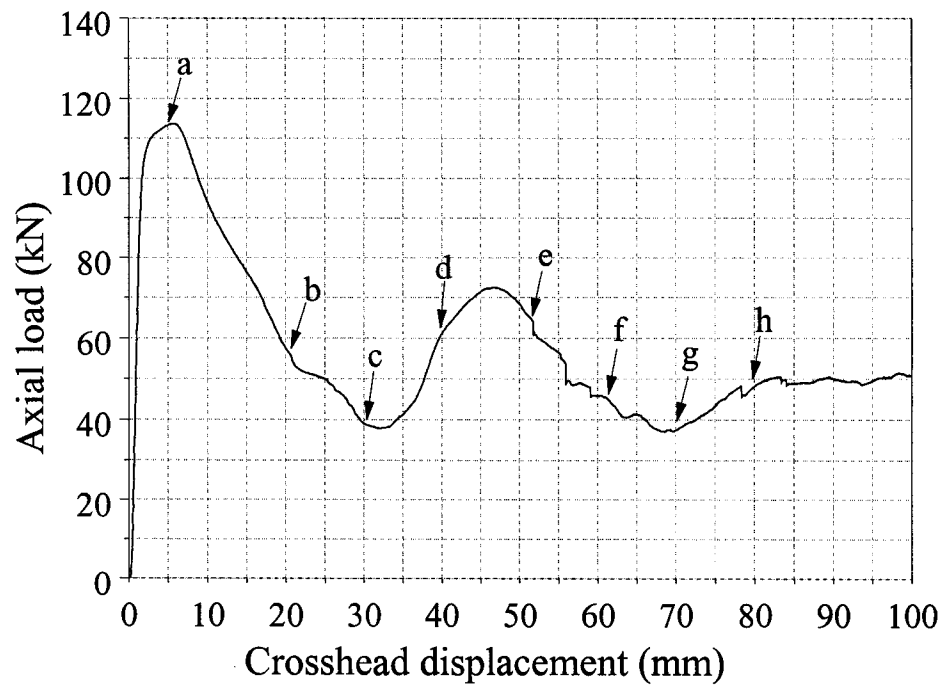


Figure 7.18. Experimentally obtained load versus displacement profile for a representative specimen from sub-group E3-3.

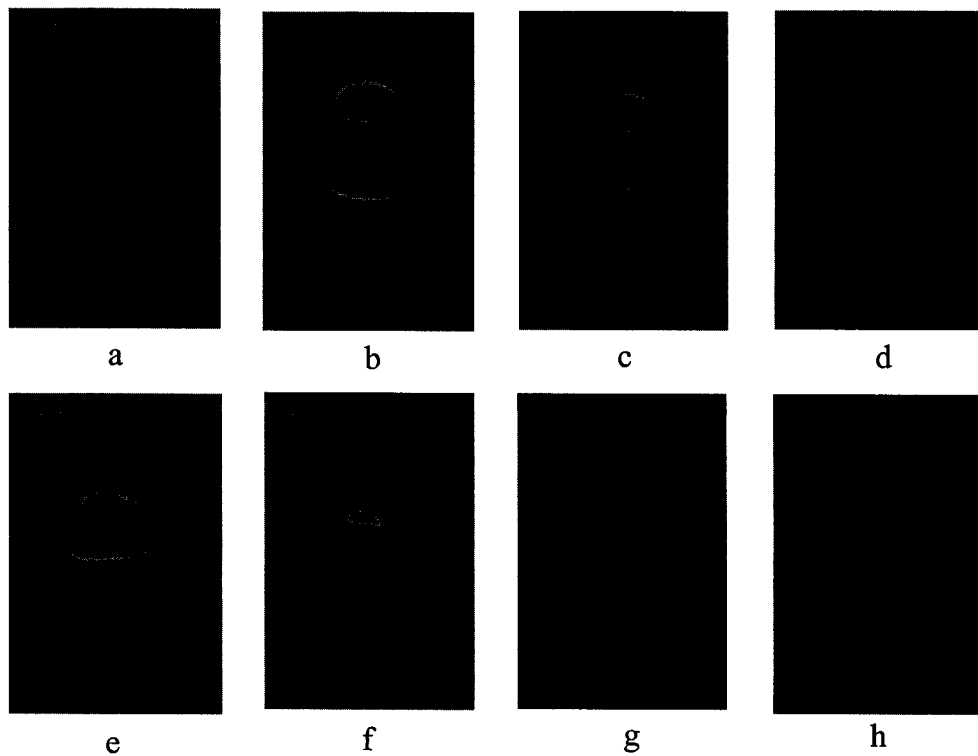


Figure 7.19. Photographs illustrating the crushing process for a representative specimen from sub-group E3-3.

7.2.5 Energy Absorption Performance Comparison Between Specimens

This section compares the energy absorption and crush performance parameters of each sub-group considered. The crush performance parameters are calculated from the experimental load/displacement observations as indicated in equation (5.1) through equation (5.5).

7.2.5.1 Total Energy Absorption and Crush Force Efficiency

The total energy absorbed during the deformation process and the *CFE* for specimens in Group 2, Group 3 and Group 4 are presented in Figure 7.20, Figure 7.21 and Figure 7.22 respectively. For comparison purposes the energy absorbed and the *CFE* are also presented in Figures 7.20 through 7.21 for a representative specimen in Group 1. As expected, both the total energy absorbed and the *CFE* were larger for specimens with geometrical discontinuities than that of specimens which collapsed in the global bending mode. Specimens in sub-group S3-2 had the largest energy absorption of 5.85 kJ amongst all the specimens in this investigation. This magnitude of energy absorption represented an increase of approximately 75% over the specimens in Group 1 which had no discontinuity.

Specimen S2-3 from Group 2 exhibited the highest total energy absorption of 5.73 kJ in this group and the highest *CFE* of 52.1% amongst specimens from all groups as indicated in Figure 7.20. These values represent a 71% increase in total energy absorption and a 96% increase in the *CFE* compared with specimens in Group 1. Specimen E2-3, also within Group 2 possessing an elliptical discontinuity, exhibited the second highest total energy absorption and crush force efficiency. Other specimens in Group 2 with the same major axis length of 14.29 mm illustrated a direct relationship between aspect ratio and both the total energy absorbed and the *CFE*. For example, specimens with slotted discontinuities, with aspect ratios of 2.0 and 3.0 illustrated respective total energy absorption values which were 3% and 33% greater than the energy absorption values observed for specimens with slotted discontinuities with an aspect ratio of 1.33. Specimens with elliptical discontinuities with aspect ratios of 2.0

and 3.0 exhibited increases in the total energy absorbed by 0.7% and 25% respectively compared with specimens with elliptical discontinuities having an aspect ratio of 1.33. Experimental observations illustrated that specimens S2-3 and E2-3 collapsed in SMII mode. All other specimens within Group 2 collapsed in SMI mode.

Specimens in Group 3, independent of discontinuity geometry, with an aspect ratio of 1 and 1.33 illustrated very similar observations for the total energy absorbed and *CFE* as presented in Figure 7.21. Specimen S3-2 exhibited the highest value of total energy absorption and the second largest value of the *CFE* amongst all specimens considered in this research. Although all specimens in Group 3 deformed in SMII mode, specimens with larger aspect ratios formed the first plastic hinge at lower crosshead displacements compared with specimens in this group with aspect ratios near unity. This should be expected as the formation of the first plastic hinge typically forms after the discontinuity has collapsed and specimens with small aspect ratios exhibit larger minor axis dimensions and thus requiring larger crosshead displacements for complete collapse of the discontinuity. Specimens with large aspect ratios typically involve the formation of a greater number of folds, due to the small minor axis length, which results in higher energy absorption, mean crushing force, and the *CFE*. This finding was especially noticed in Group 2 and Group 3 and not significantly evident in Group 4.

Specimens within Group 4 illustrated more consistent values of the total energy absorption and *CFE* compared with observations from specimens within Group 2 and Group 3. The consistency of the total energy absorbed and *CFE* for specimens within Group 4, as presented in Figure 7.22, indicate that these crush performance parameters appear to be somewhat independent of aspect ratio and discontinuity geometry. Two specimens within the sub-group E4-3 illustrated global bending deformation behaviour with total energy absorption and *CFE* values very similar to specimen W0. The presence of a discontinuity with this geometry (small major axis length and large aspect ratio) did not function as an effective triggering mechanism to initiate a SMI or SMII buckling mode.

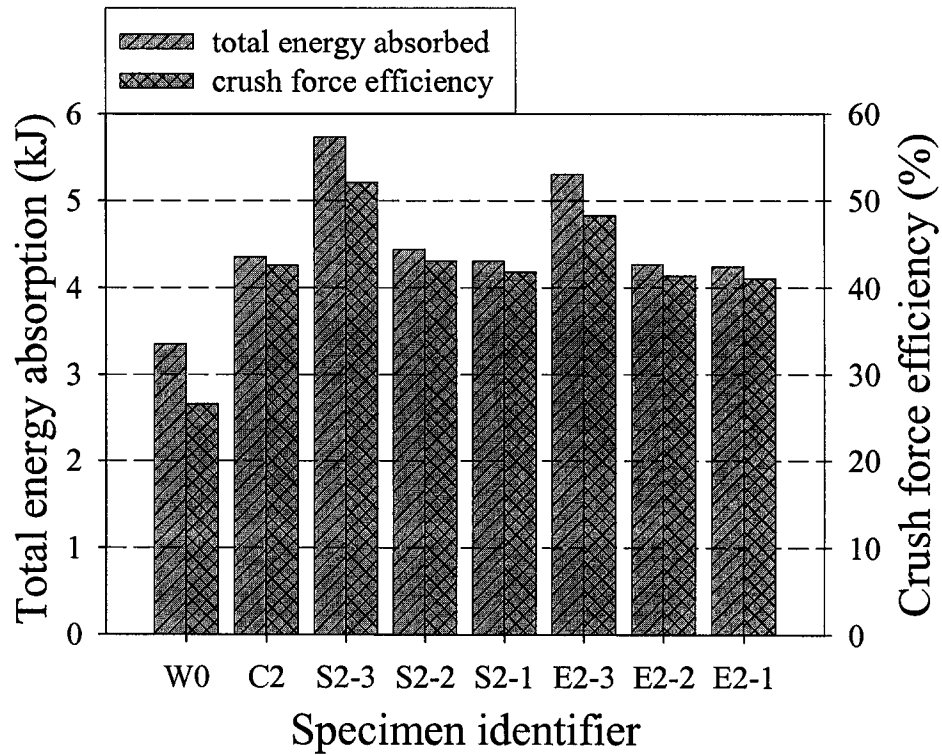


Figure 7.20. Total energy absorption and *CFE* for specimens in Group 2 (observations from specimen in Group 1 are included for comparison).

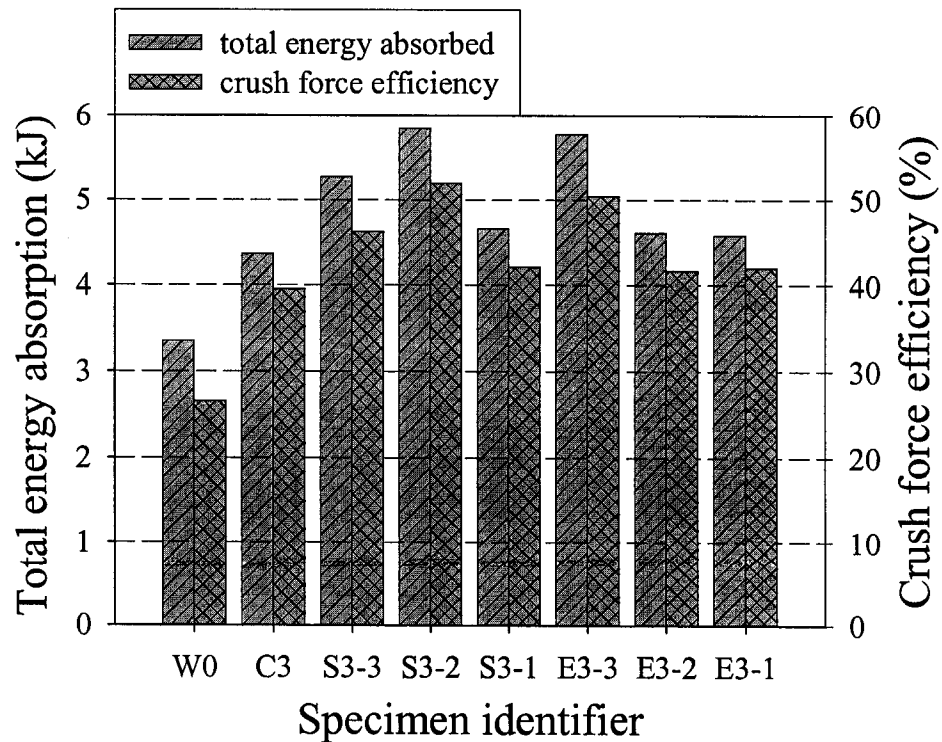


Figure 7.21. Total energy absorption and *CFE* for specimens in Group 3 (observations from specimen in Group 1 are included for comparison).

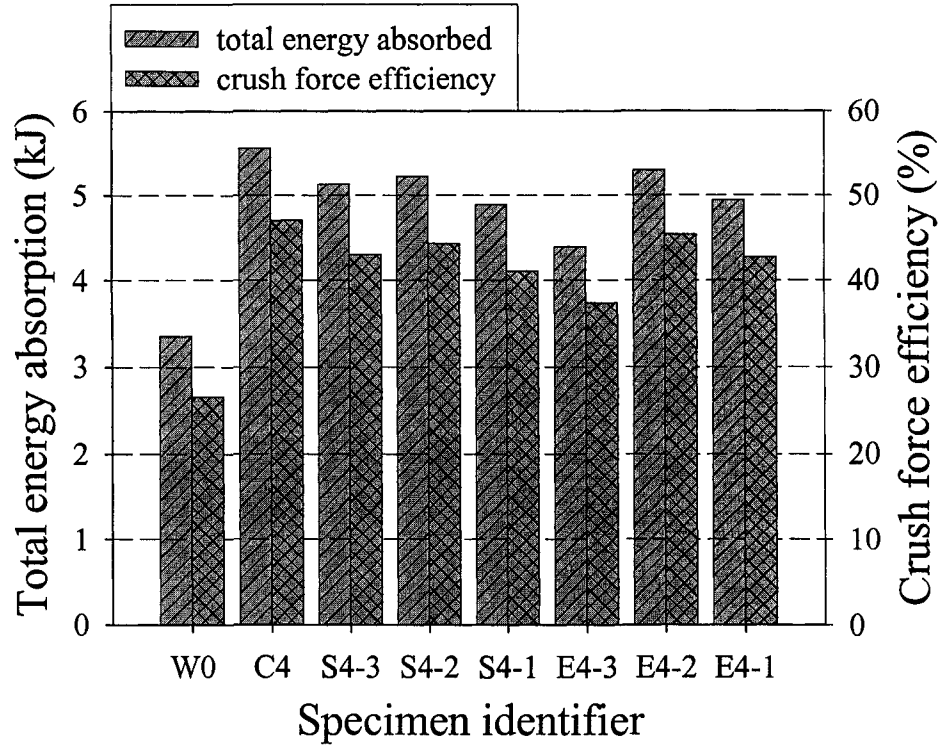


Figure 7.22. Total energy absorption and CFE for specimens in Group 4 (observations from specimen in Group 1 are included for comparison).

7.2.5.2 Peak Crush Load and Mean Crush Load

Figure 7.23, Figure 7.24 and Figure 7.25 present the peak and mean crush loads for Group 2, Group 3 and Group 4 respectively. Results from Group 1 are also presented in these figures from comparison purposes. From Figure 7.23, it can be noted that for specimen W0, which deformed in the global bending deformation mode, the largest peak crush load (124.7 kN) and the smallest mean crush load (33.2 kN) were observed. As expected an indirect relationship between peak crush load and major axis length was observed.

A direct relationship between aspect ratio and both the peak and mean crush loads for specimens with slotted and elliptical discontinuity geometries within Group 2 was somewhat evident. However, only a minor variation in the peak and mean crush loads was observed for specimens with aspect ratios of 1.33 and 2. Specimens with any

geometry of discontinuity with aspect ratios near unity illustrated very similar peak and mean crush loads.

No obvious relationship between geometry of discontinuity and peak and mean crush loads is apparent from the observations presented in Figure 7.24 for specimens in Group 3.

An analysis of the observations for specimens in Group 4, as presented in Figure 7.25, clearly indicate that there is no discernible relationship between the geometry of discontinuity and the peak and mean crush loads.

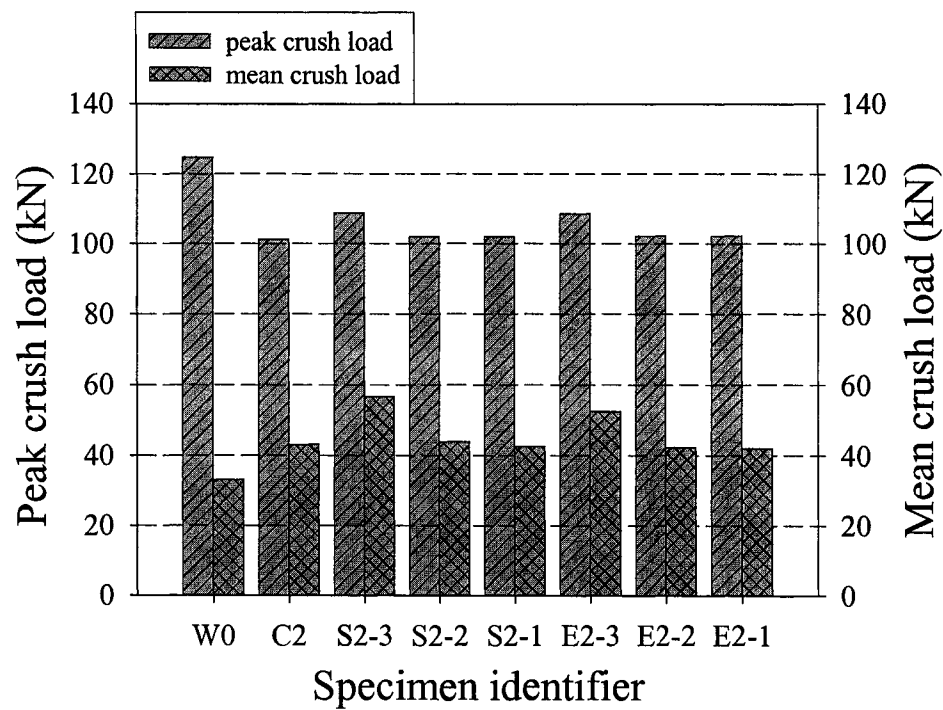


Figure 7.23. Peak and mean crush loads for specimens in Group 2 (observations from specimen in Group 1 are included for comparison).

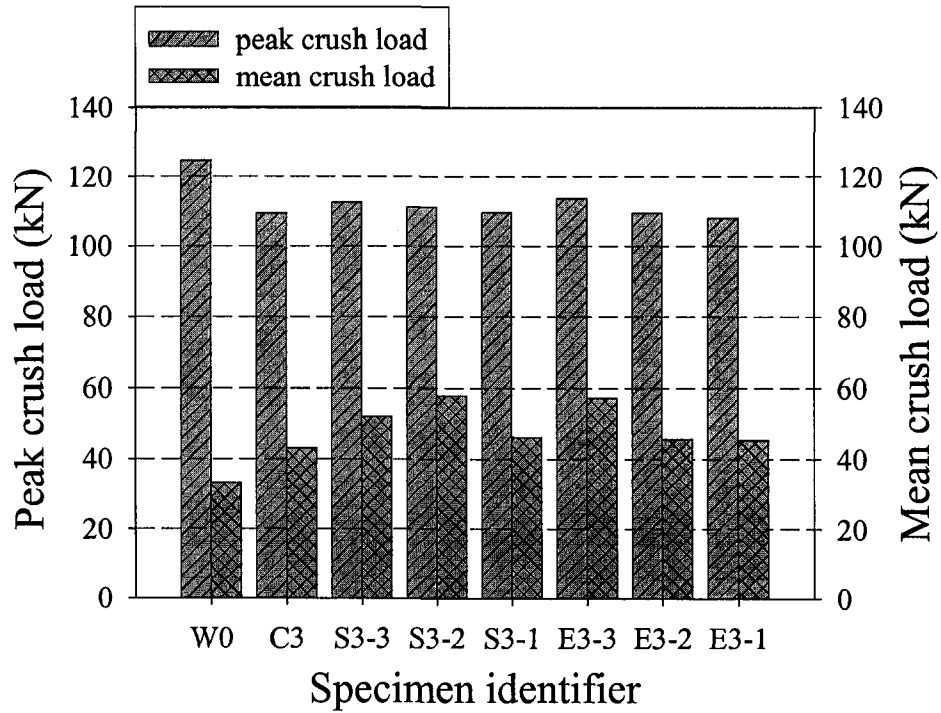


Figure 7.24. Peak and mean crush loads for specimens in Group 3 (observations from specimen in Group 1 are included for comparison).

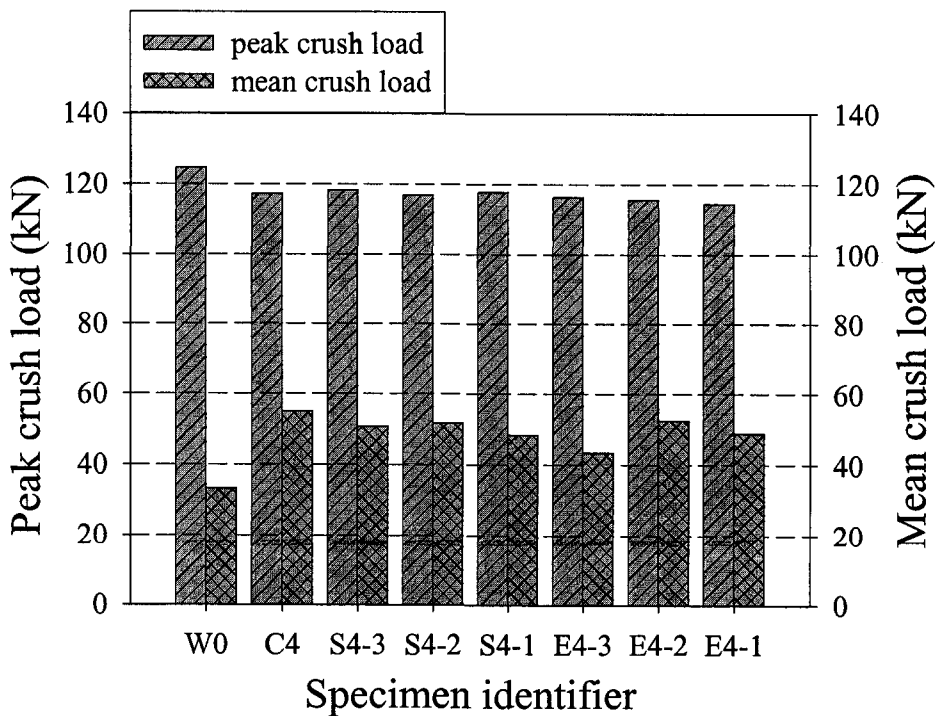


Figure 7.25. Peak and mean crush loads for specimens in Group 4 (observations from specimen in Group 1 are included for comparison).

7.2.5.3 Specific Energy Absorption

Figure 7.26 through Figure 7.28 graphically illustrate and compare the *SEA* for all specimens considered in this investigation. Figure 7.26 clearly indicates that for discontinuities with an aspect ratio less than 2 the *SEA* is generally independent of discontinuity geometry and approximately equal to 18.5 kJ/kg. However, for both slotted and elliptical discontinuity geometries with aspect ratio equal to 3 a significant increase in the *SEA* within this group of specimens was observed. Specimen S2-3 exhibited the largest *SEA* with a magnitude of 24.2 kJ/kg.

A comparison of Figure 7.26 through Figure 7.28 illustrate that for specimens with smaller major axis lengths a decrease in the influence of aspect ratio on the *SEA* is observed. Furthermore, a slight increase in the *SEA* was observed for specimens with small major axis lengths.

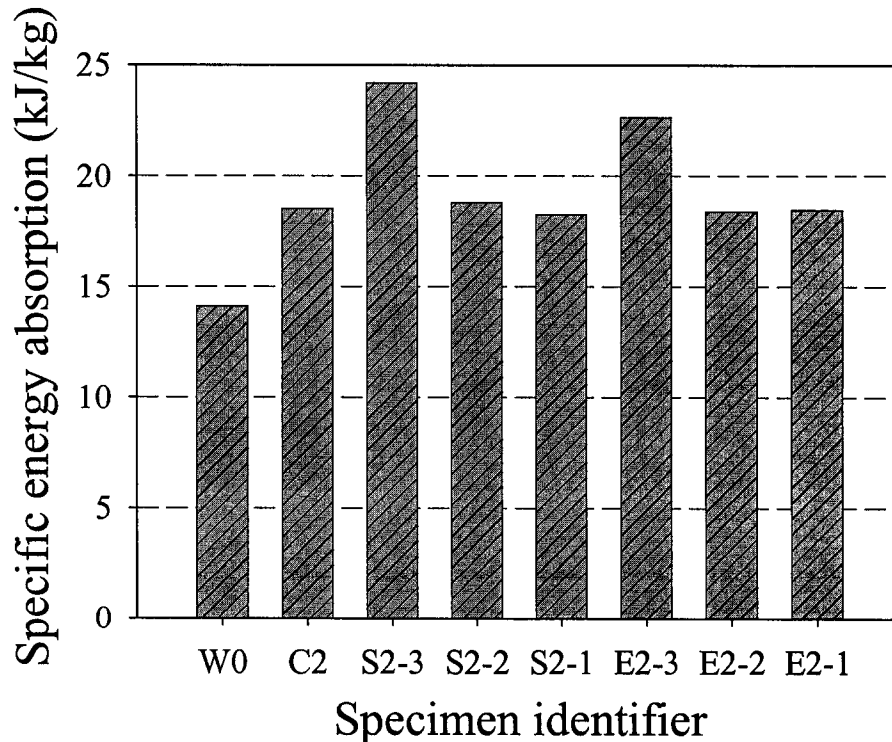


Figure 7.26. Specific energy absorption for specimens in Group 2 (observations from specimen in Group 1 are included for comparison).

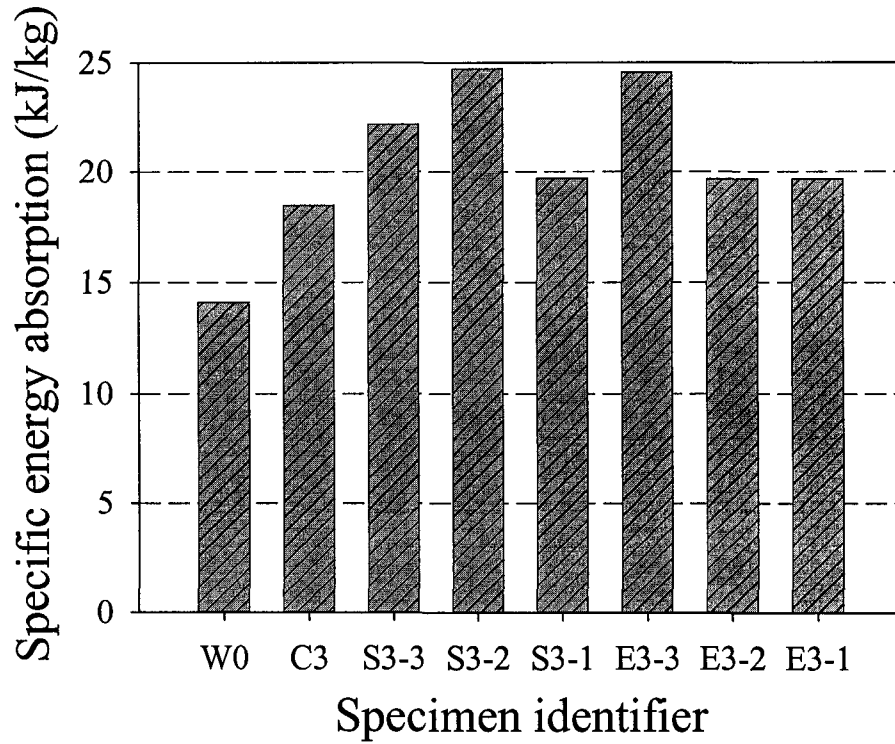


Figure 7.27. Specific energy absorption for specimens in Group 3 (observations from specimen in Group 1 are included for comparison).

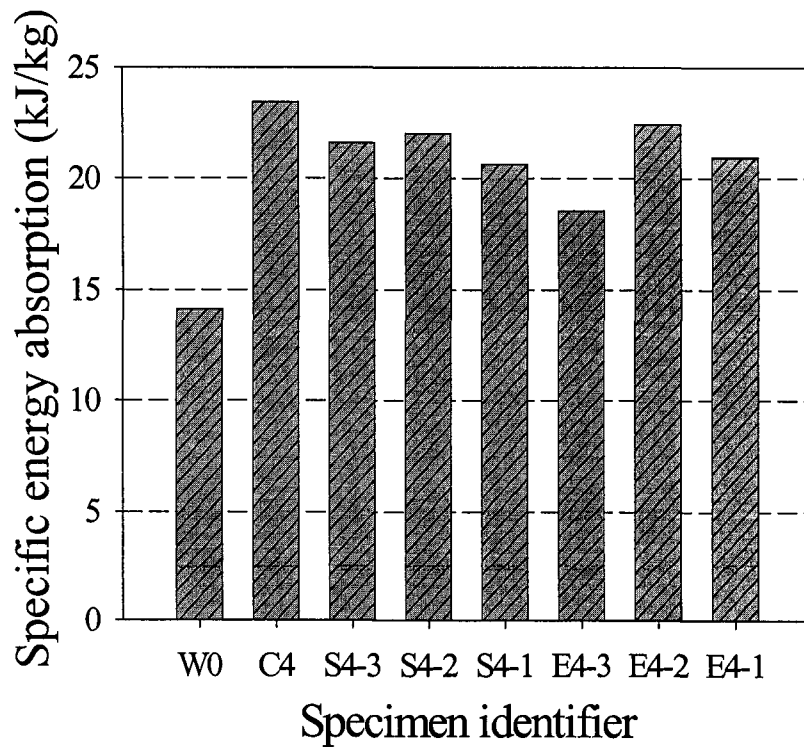


Figure 7.28. Specific energy absorption for specimens in Group 4 (observations from specimen in Group 1 are included for comparison).

7.3 Quasi-Static Axial Compressive Cut Testing Results and Discussion

For each specimen tested, the cutting force and crosshead displacement were recorded. Post-testing data analysis was completed to determine the peak load, mean crush force, *CFE*, total energy absorption, and the *SEA*. Values for each specimen are presented in Table 7.3.

Table 7.3. Experimental testing results.

Group	Specimens	P_{max} (kN)	P_m (kN)	<i>CFE</i>	$E_{absorbed}$ (kJ)	<i>SEA</i> (kJ/kg)
1	SA1	38.71	26.98	0.700	3.77	15.87
	SA2	37.92	30.64	0.810	4.26	17.91
	SA3	36.66	30.44	0.830	4.25	17.89
	SA4	36.54	29.06	0.795	3.97	16.71
	SA5	37.22	29.40	0.790	4.12	17.32
2	SB1	35.84	28.70	0.800	4.02	16.91
	SB2	35.52	28.75	0.810	4.02	16.91
	SB3	34.05	25.21	0.740	3.56	14.96
	SB4	38.48	28.00	0.728	3.91	16.46
	SB5	33.64	27.95	0.831	3.91	16.42
3	LA1	31.94	26.13	0.820	3.67	10.30
	LA2	34.99	28.01	0.800	3.91	10.97
	LA3	34.34	26.69	0.780	3.71	11.28
	LA4	35.19	30.18	0.858	4.23	11.85
	LA5	42.29	30.85	0.729	4.37	12.26
4	LB1	41.14	31.76	0.772	4.49	12.57
	LB2	37.57	28.60	0.761	3.99	11.18
	LB3	35.58	29.20	0.821	4.15	11.62
	LB4 (no lubrication)	41.44	29.36	0.708	4.07	11.42
	LB5 (no lubrication)	37.27	29.67	0.796	4.17	11.69
5	LG1	115.82	21.05	0.182	2.91	8.15
	LG2	115.97	21.23	0.183	2.94	8.25
	LG3	114.80	20.10	0.175	2.79	7.81
6	SG1	125.28	32.34	0.258	3.72	15.65
	SG2	123.81	30.84	0.249	3.39	14.24
	SG3	124.69	31.63	0.254	3.71	15.59

7.3.1 Cutting Test Results for Specimens in group 1

Specimens in group 1 were axially crushed using side A of the cutter. Photographs of the cutting process for a typical specimen (specimen SA1) are shown in Figure 7.29. The observed force versus displacement curves for all specimens in group 1 are presented in Figure 7.30. The points at which photographs were taken of specimen SA1 were marked on the corresponding force versus displacement curve of Figure 7.30. Photographs of the cutting deformation illustrate that the cutter can penetrate through the four corners of the specimens and develop highly localized plastic deformation in the vicinity of the cutting blades. Cutting chips were observed to be formed during the cutting process as shown in Figure 7.31, which also illustrates the localized plastic deformation accompanying the cutting process for specimen SA4 (Figure 7.31(a)). No crack propagation was observed in all testing. As the cutting progressed, petalled side walls bent outward due to the pushing force developed from the interaction between the side walls of the cutter blades and tube material which were oriented at an angle of approximately 45 degrees to each other. The increasing width of the blades at the transitional region to the cutter hub also contributed to the bending force when split side walls came into contact with the hub as illustrated in Figure 7.29(f) and Figure 7.31(c). It is evident from the force versus displacement curves that the cutting test results were similar to each other. Load/displacement profiles for specimens SA2, SA3, SA4, and SA5 were almost coincident. At the initial cutting stage, after half of the blades of the cutter penetrated through the extrusions (at an approximate displacement of 10 mm), the cutting force was approximately 24 kN for all test specimens. This cutting force was maintained constant until a crosshead displacement of approximately 50 mm. After that displacement, the petalled side walls began bending outwards. The bending phenomenon increased the cutting force to approximately 35 kN. As bending of the petalled side walls continued, the cutting force was observed to be somewhat constant at a value of 35 kN. For each specimen, the petalled side walls were bended with different radii. For specimen SA4, one of the four petalled walls was observed to have contact with the hub of the cutter as shown in Figure 7.31 (c), which caused a higher degree of bending within the side walls of the extrusion. This finding was also observed for specimens SA2, SA3,

and SA5. It was observed for all specimens, except SA1, that an increase in force from approximately 24 kN to 35 kN occurred during cutter displacements from 50 mm to 80 mm. Specimen SA1 illustrated an increase in cutting force from 24 kN to 35 kN during cutter displacements of 50 mm to 130 mm. The lower rate of increase in the cutting force for specimen SA1 was attributed to the lack of contact between the side walls of the tube and the cutter hub after the blades split the extrusion, as presented in Figure 7.29(f). It was estimated from the force/displacement relationships that the bending of the side walls of the extrusion increased the cutting force by approximately 40% (from 24 kN to 35 kN). An estimated 25% increase of total energy absorption would be expected from the bending mechanism.

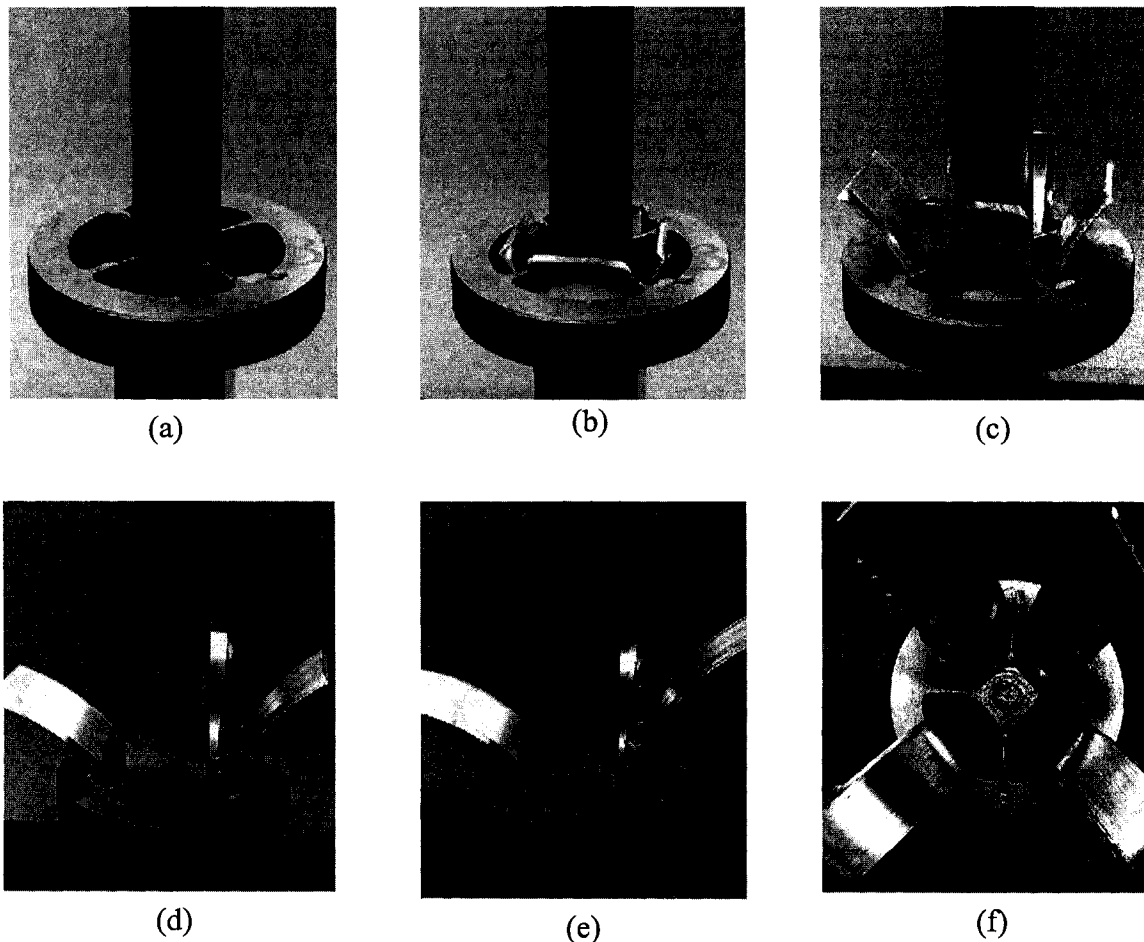


Figure 7.29. Photographs of the cutting process for specimen SA1. (a) Cutting setup using side A of the cutter, (b) splitting of the four corners of the specimen, (c) petalled side wall bending outwards, (d) and (e) progression of cutting, and (f) specimen after testing.

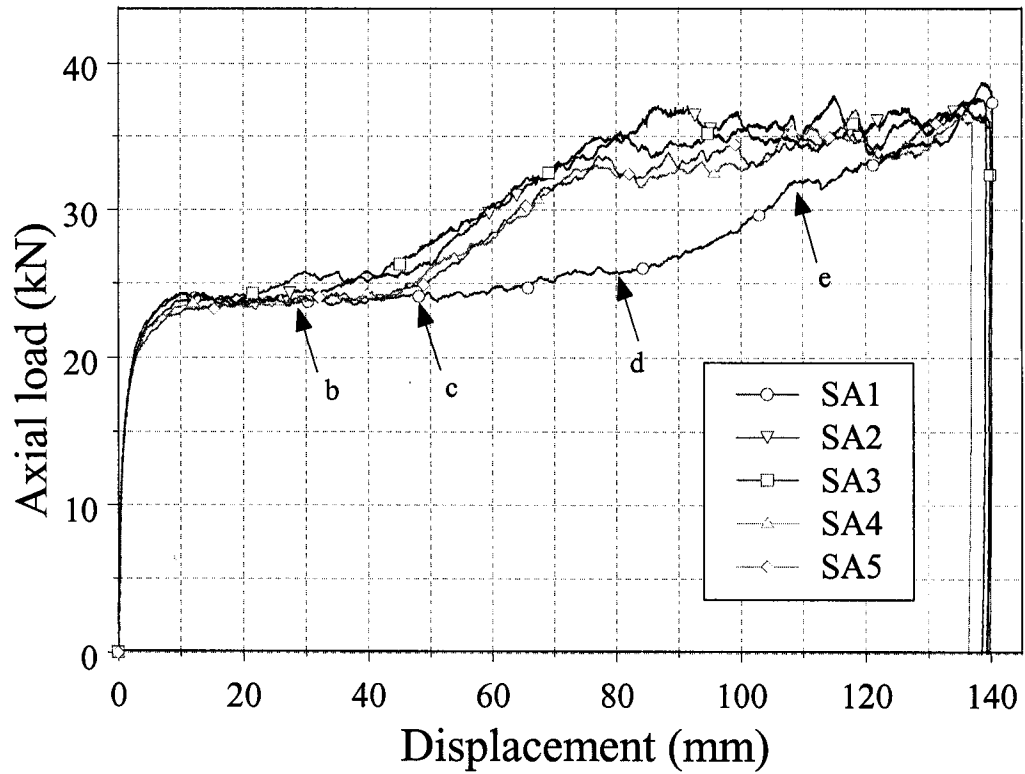


Figure 7.30. Experimentally obtained load versus displacement curves for specimens in group 1; positions b, c, d and e correspond to photographs in Figure 7.29.

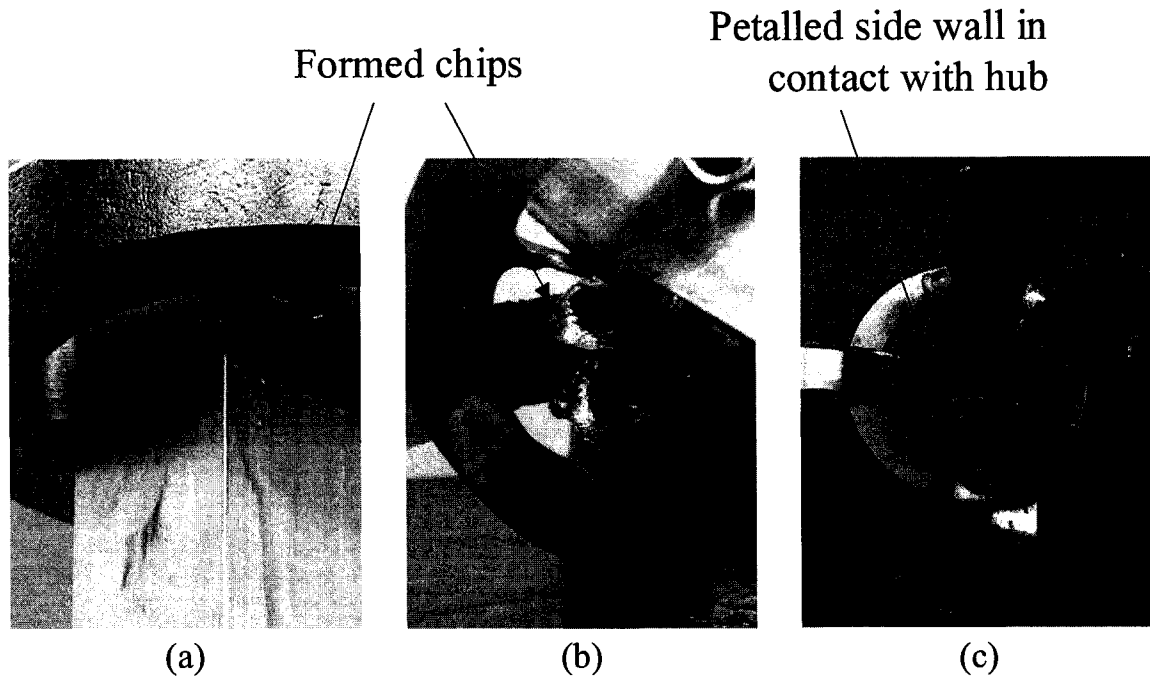


Figure 7.31. Chip formation and petalled side wall bending for specimen SA4. (a) During cutting (side view), (b) after testing (rear view), (c) after testing (front view).

7.3.2 Cutting Test Results For Specimens in Group 2

Specimens in group 2 were cut using side B of the cutter. As listed in Table 4.7, there was a small variation in the width of each blade between cutting edges on side A and side B. The force versus displacement curves for the specimens of group 2 are shown in Figure 7.32. No significant difference in the load/displacement profiles was observed between group 2 and group 1, except that the displacement at which the cutting load began to increase due to side wall petalling and contact between the extrusion side walls and cutter hub occurred at approximately 60 mm for group 2 rather than 50 mm as was observed for group 1. A stable cutting process was observed for all specimens in group 2, similar to group 1. Specimen SB3 was observed to have a relatively lower increase in cutting force through cutter travel due to the lack of contact occurring between the side walls of the extrusion and the cutter hub, similar to specimen SA1 in group 1.

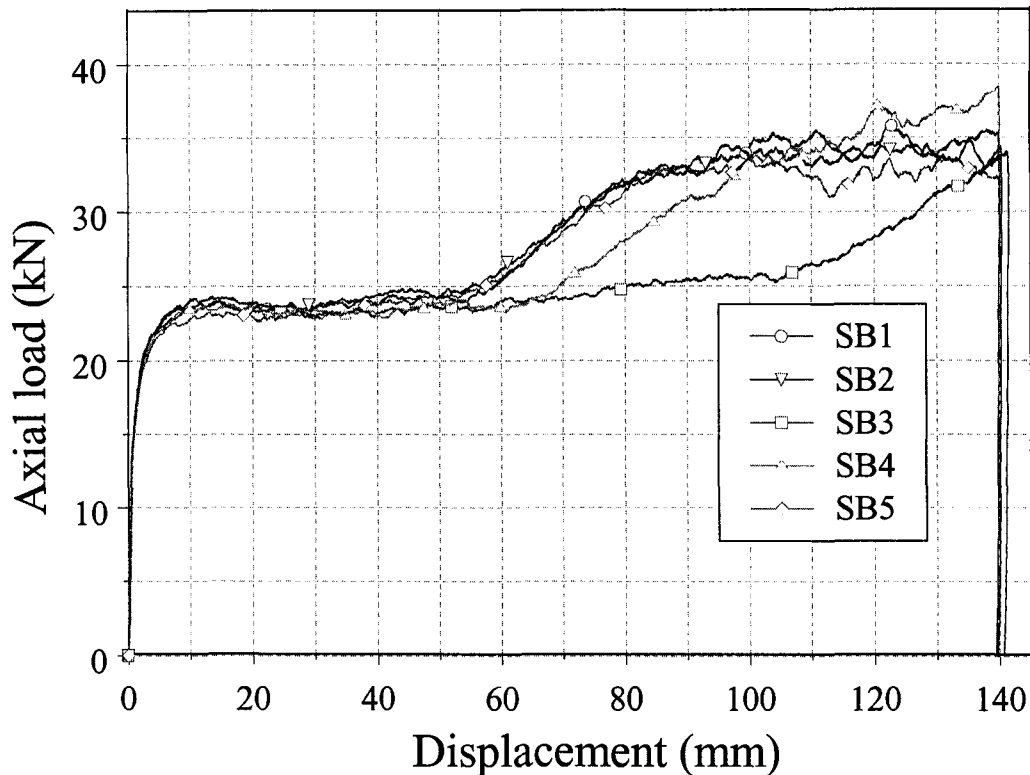


Figure 7.32. Experimentally obtained load versus displacement curves for specimens in group 2.

7.3.3 Cutting Test Results For Specimens Group 3 and Group 4

Specimens in group 3 and group 4 had the same tube length of 300 mm. Side A and side B of the cutter were used to cut specimens in group 3 and group 4 respectively. The force versus displacement curves for the specimens of group 3 and group 4 are shown in Figure 7.33 and Figure 7.34 respectively. The stability of the cutting process and the force/displacement profiles for the 300 mm length specimens in groups 3 and 4 appeared to be very similar to the qualitative and quantitative observations from the 200 mm length specimens in groups 1 and 2. No significant differences in the force/displacement profiles for group 3 and group 4 were observed, except that the specimens in group 3 illustrated a greater variation in the crosshead displacement location

where the cutting force increased due to contact between the extrusion side walls and the hub of the cutter.

Specimens LB4 and LB5 which were cut without the use of lubrication had very similar force/displacement profiles as all other specimens in group 4. This was attributed to the minimal contact area occurring between the sides of the cutting blades and the petalled side walls.

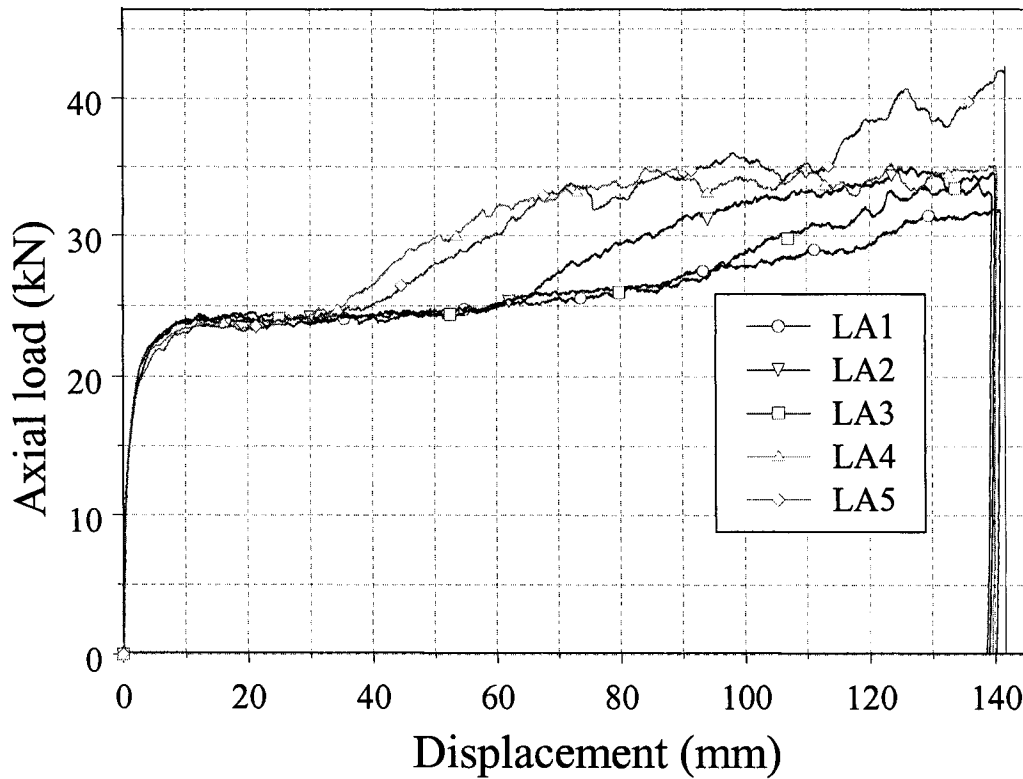


Figure 7.33. Experimentally obtained load versus displacement curves for specimens in group 3.

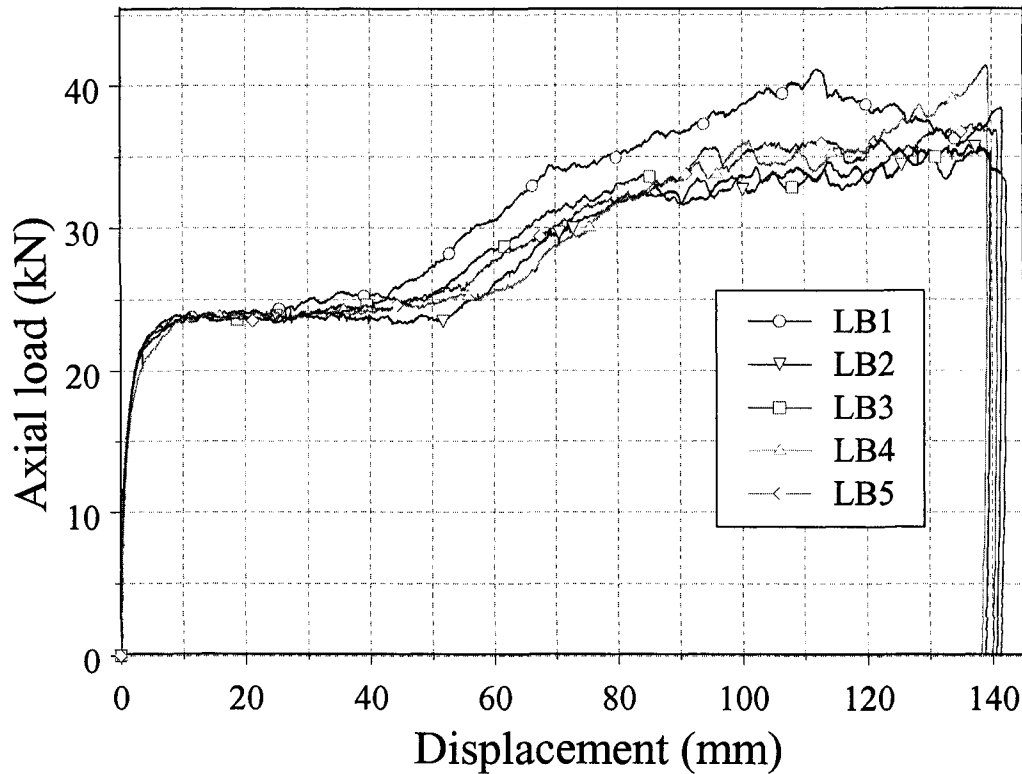


Figure 7.34. Experimentally obtained load versus displacement curves for specimens in group 4.

7.3.4 Crush Test Results For Specimens Group 5 and Group 6

Axial compressive crushing tests without the presence of the cutter were performed for the three specimens in group 5, which had a length of 300 mm, and the three specimens in group 6, which had a length of 200 mm. Specimens in these two groups all collapsed in the global bending mode as expected and had similar load versus displacement curves as shown in Figure 7.35 and Figure 7.36 for group 5 and group 6 respectively. As the bending of the specimen progressed, the plastic strain at the edges of the sidewalls in the kinked region of the tube exceeded the failure strain of the material. Cracking occurred at the corners of the tube within the region of the kink near the mid-span of the absorber. Global bending and cracking caused the force displacement

profiles to have a large negative slope after the peak buckling load. An average peak buckling load of 115.53 kN was observed for specimens in group 5, while an average peak buckling load of 124.59 kN for specimens in group 6. After the development of a mid-span kink, which occurred after approximately 30 mm crosshead displacement, crushing loads with magnitudes of 7 kN and 10 kN for group 5 and group 6 respectively were observed.

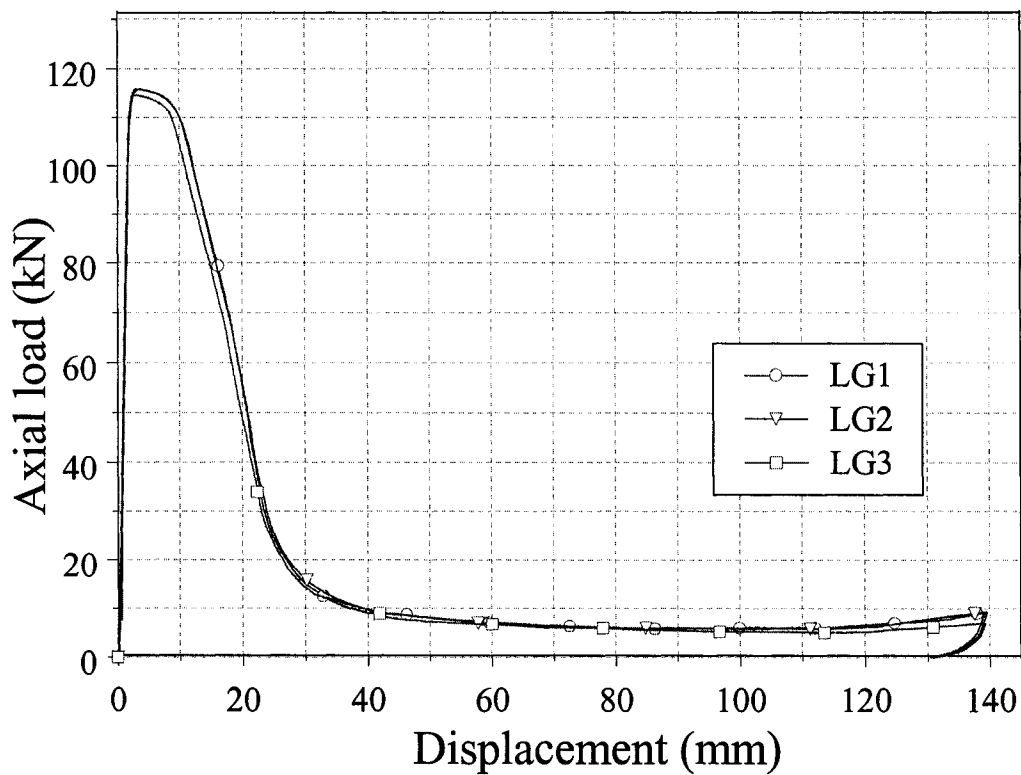


Figure 7.35. Experimentally obtained load versus displacement curves for specimens in group 5.

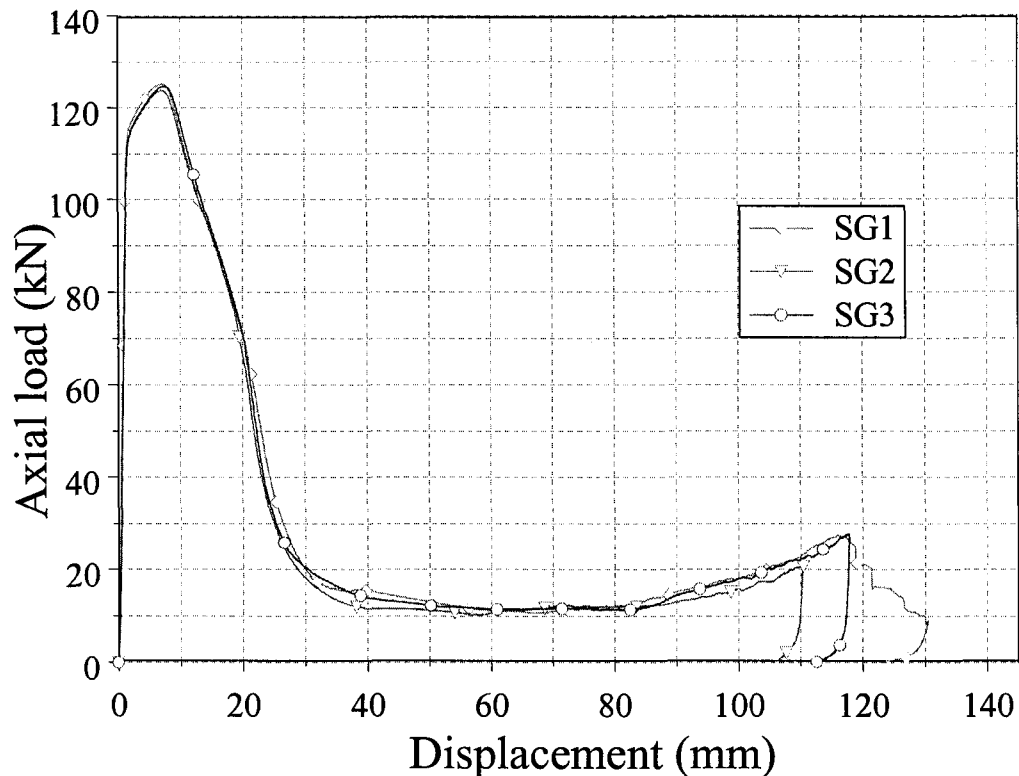


Figure 7.36. Experimentally obtained load versus displacement curves for specimens in group 6.

7.3.5 Comparison of Testing Results amongst All Specimens

Due to the load/displacement similarities observed for all specimens within a specific group, a sample was selected which represented the average load/displacement behaviour for the group. Figure 7.37 illustrates the load/displacement characteristics from the representative sample of each group. From this comparison, it is obvious that the cutting force response of specimens with different lengths and cutting edges are very similar, while it is quite different than that of global buckling deformation. For all specimens which underwent deformation due to splitting, the cutting force was kept at a nearly constant magnitude during the entire deformation process.

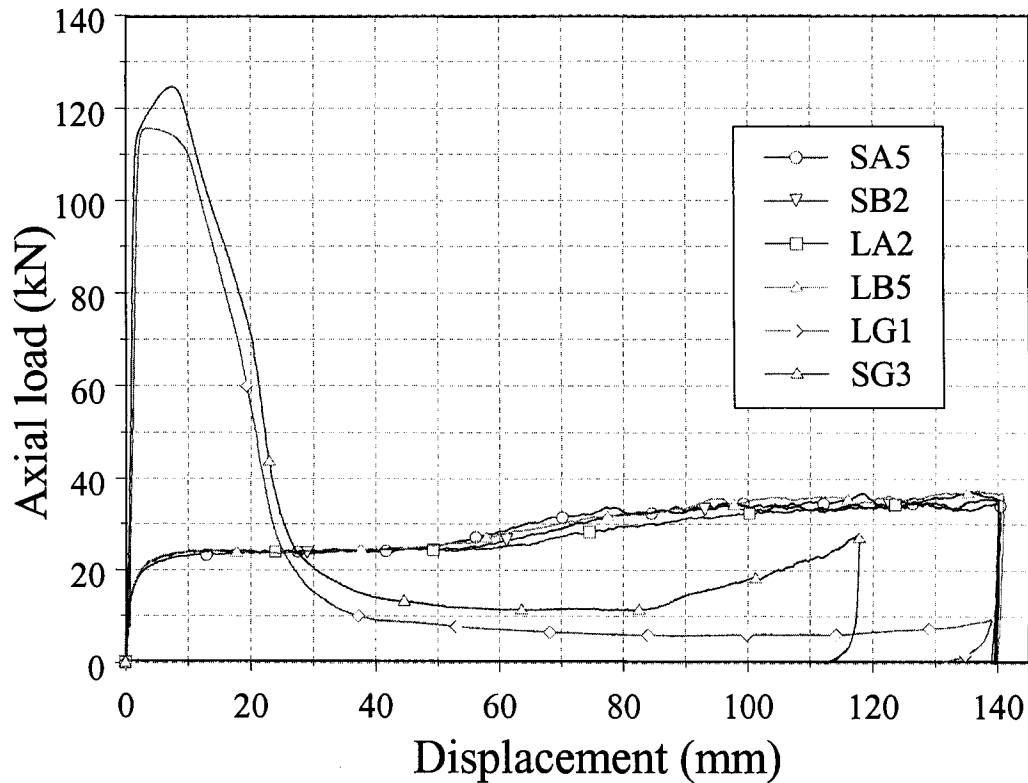


Figure 7.37. Force/displacement profile comparisons for representative specimens from each group.

7.3.6 Crush Performance Parameter Comparison amongst All Specimens

The experimental results in terms of the energy absorption and crush performance parameters for each group of specimens are compared in this section. Crush performance parameters including the peak load, mean crush force, *CFE*, total energy absorption, and the *SEA* were calculated from the experimental data.

7.3.6.1 Peak Load and Mean Crush Force

The peak load and the mean crush force for specimens with 200 mm and 300 mm lengths are presented in Figure 7.38 and Figure 7.39 respectively. Comparisons of the

peak load and mean crush force from representative specimens from each group are presented in Figure 7.40. It is apparent from these figures that there were only minor variations in the peak load and mean crush force from specimens within each group. Furthermore, Figure 7.40 clearly illustrates that the difference between the peak load and mean crush force for specimens which underwent cutting modes of deformation were very small compared to the specimens which experienced global bending deformation. The ranges for peak load and mean crush force for the 200 mm length specimens were 34 kN to 39 kN and 25 kN to 31 kN respectively. The ranges for peak load and mean crush force for the 300 mm length specimens were 32 kN to 42 kN and 26 kN to 32 kN respectively. This comparison also indicates that there is very little variation in the peak load and mean crush force for specimens with varying length.

The small variation in the widths of the cutting blades on side A and side B had no significant influence on the cutting force responses of specimens in different groups. Minor cutting force variations within a group were most likely the result of differences in manual alignment of the cutter to the extrusions prior to the crush test. This minor variation in alignment would result in differences in the location of cutting within an extrusion. Geometrical and material differences between each specimen could also result in force/displacement variations amongst specimens within a group.

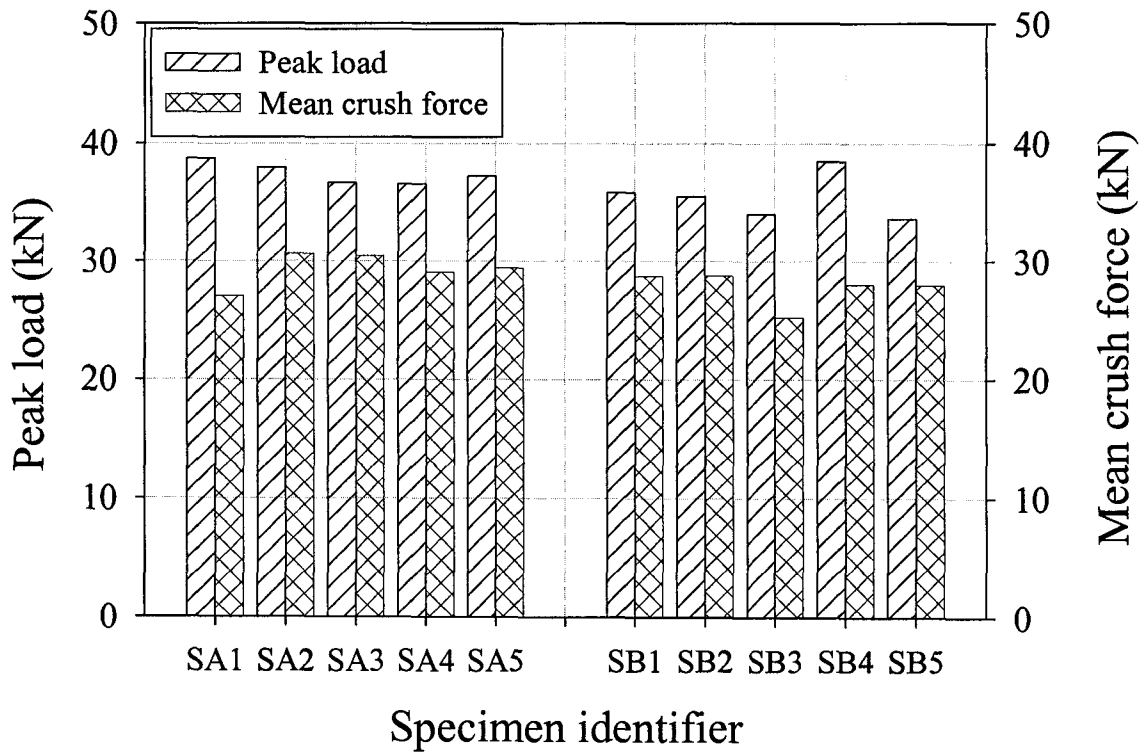


Figure 7.38. Peak load and mean crush force comparison for specimens in groups 1 and 2.

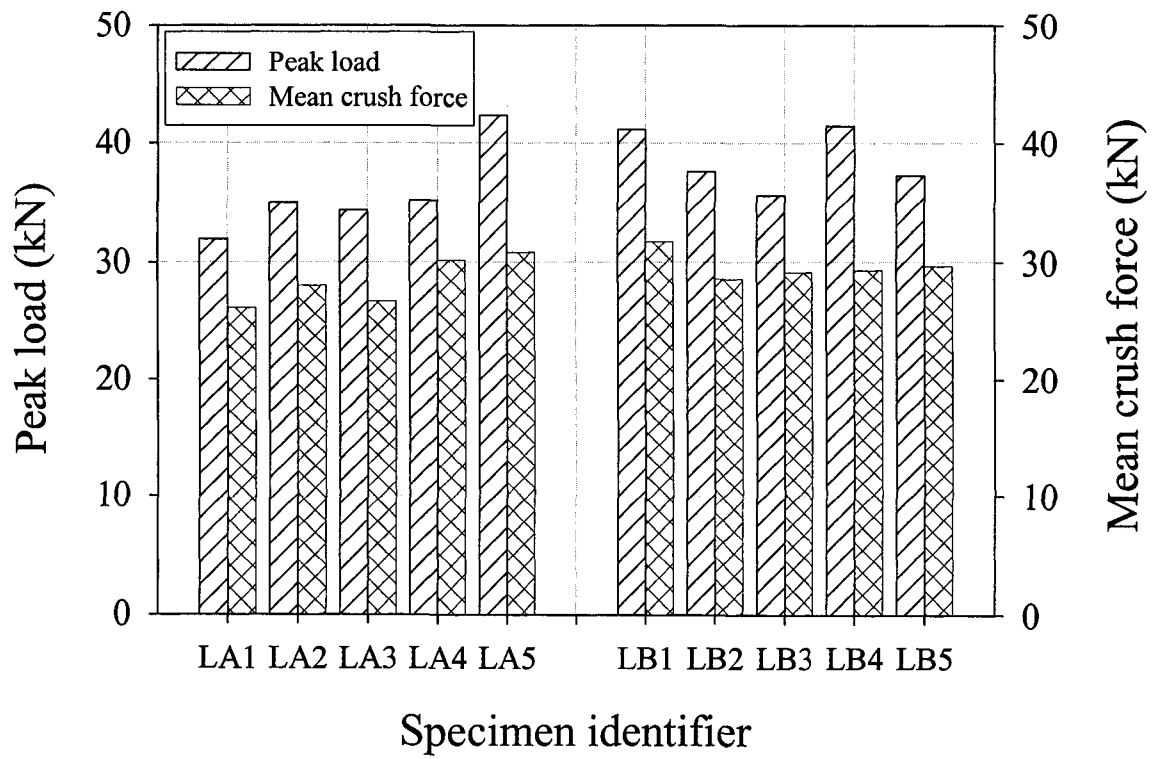


Figure 7.39. Peak load and mean crush force comparison for specimens in groups 3 and 4.

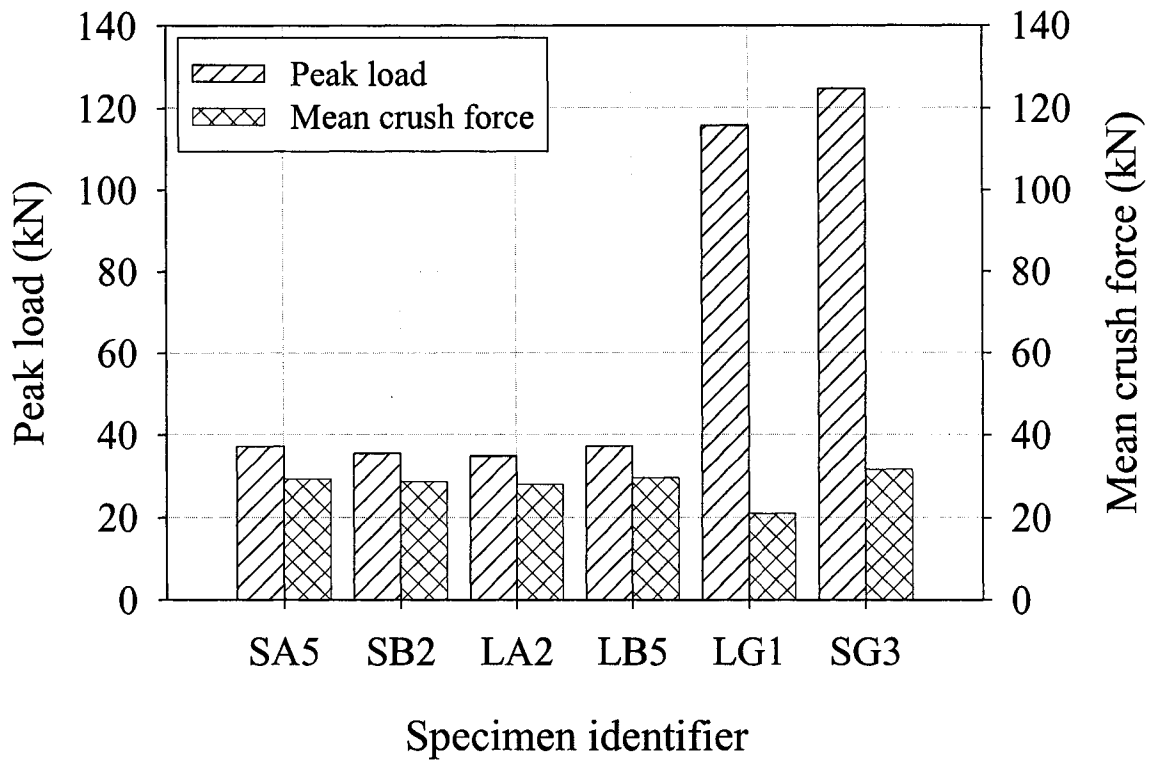


Figure 7.40. Peak load and mean crush force comparison amongst representative specimens from each group.

7.3.6.2 Crush Force Efficiency and Total Energy Absorption

The total energy absorption and *CFE* for specimens with lengths of 200 mm and 300 mm are presented in Figure 7.41 and Figure 7.42 respectively. Figure 7.43 illustrates the *CFE* and total energy absorption comparison between representative specimens selected from each group. For specimens in group 1 and group 2 the average *CFE* was calculated to be 78.5% and 78.2% respectively. For specimens in group 3 and group 4 the average *CFE* was calculated to be 79.7% and 77.1% respectively. These values illustrate a very minor variation in the *CFE* for specimens with different lengths and application of different cutting sides. For extrusions which experienced the global bending mode of deformation the average *CFE* was calculated to be 18.0% and 25.4% for specimens in group 5 and group 6 respectively. It is apparent from this research that a four fold value of the *CFE* has been achieved with the cutting mode of deformation

compared to the global bending mode of deformation for the tubular geometries and material considered in this investigation.

For specimens that underwent global bending the average total energy absorption was calculated to be 3.24 kJ. The average total energy absorption of all specimens which experienced the cutting mode of deformation was calculated to be 4.03 kJ, which is an increase of approximately 24% of the average total energy absorption of specimens which experienced global bending.

A variation of only 2.4% in the average total energy absorption was found for specimens that experienced the cutting mode of deformation with 200 mm and 300 mm lengths. However, a significant reduction of the average total energy absorption, approximately 20%, was calculated for the 300 mm length extrusions compared to the 200 mm length tubular structures under global bending deformation.

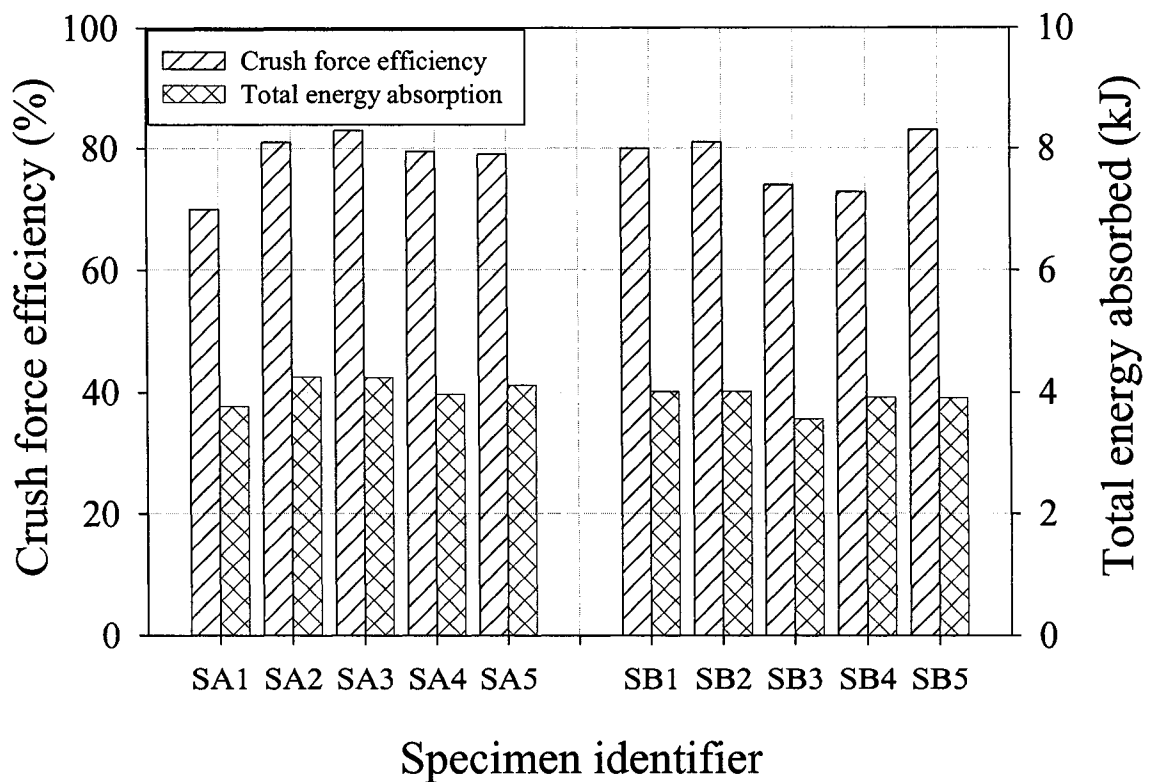


Figure 7.41. Crush force efficiency and total energy absorption comparison for specimens in groups 1 and 2.

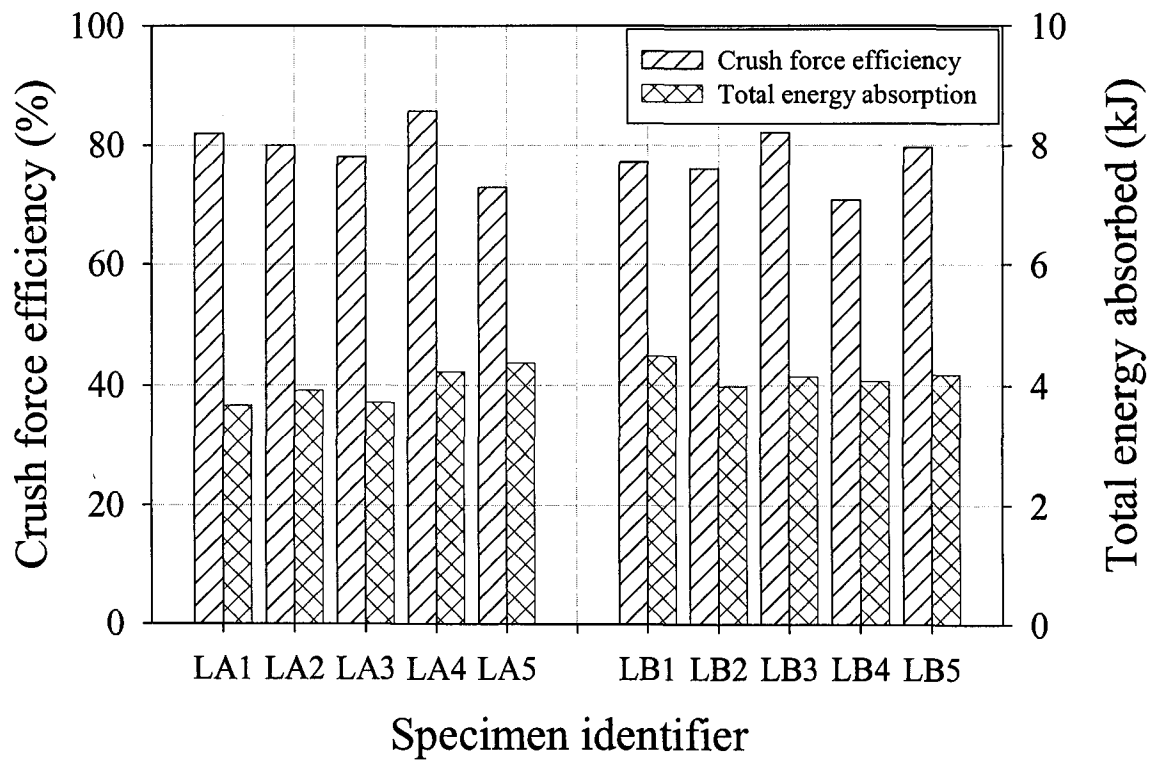


Figure 7.42. Crush force efficiency and total energy absorption comparison for specimens in groups 3 and 4.

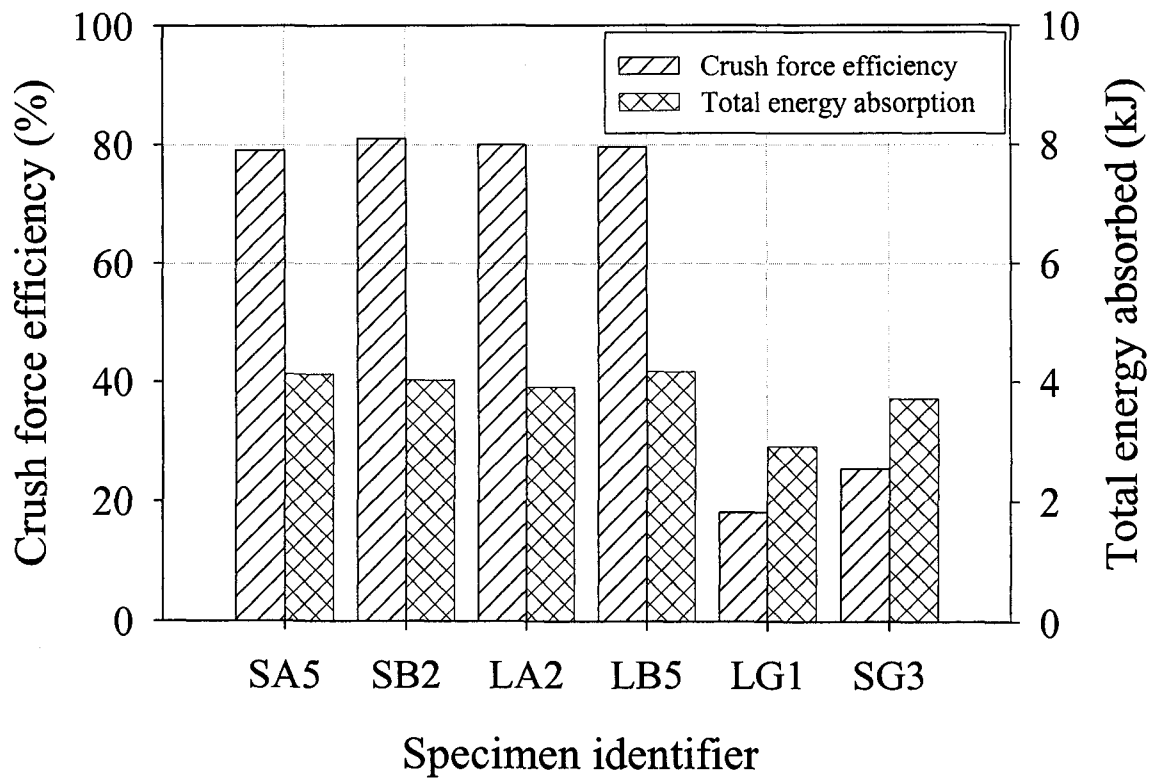


Figure 7.43. Crush force efficiency and total energy absorption comparison amongst representative specimens from each group.

8. CRUSH PERFORMANCE PARAMETERS COMPARISON BETWEEN DIFFERENT ENERGY ABSORBERS

Three energy absorption performances and improvements have been investigated in this research. The first situation was related to aluminum foam filled braided stainless steel tube under tensile loading condition. The second and third energy absorption improvements were both related to AA6061-T6 extrusions under compressive loading conditions. An energy absorption performance comparison between extrusions with a geometrical initiator and extrusions which experienced a cutting deformation have been completed to present the advantage and disadvantage of both improvement methods.

Experimental cutting test performance measures were recalculated based on a displacement up to 100 mm and are presented in Table 8.1. Crush test results for specimens with geometrical discontinuities were obtained based on the same displacement as listed in Table 7.2.

As mentioned in section 7.3.5, the cutting force response of specimens with different lengths and cutting edges are very similar. Based on this observation and the average results listed in Table 8.1, Specimen SA4 is picked to represent cutting deformation and will be used to compare with representative specimens listed in section 7.2.4, which are specimen W0, C3, S3-2, and E3-3. Specimen LG2 which had a tube length of 300 mm as tested in global bending mode has also been compared in this section. Detailed information about representative specimens is presented in Table 8.2.

Force/displacement profiles for the above mentioned specimens are illustrated in Figure 8.1. From Figure 8.1, it can be seen that specimen SA4 had an almost constant force/displacement response during the cutting deformation process, while all other specimens had large response force fluctuation during the deformation process.

Peak crush load and mean crush load comparison are illustrated in Figure 8.2. For cutting deformation mode, peak crush load and mean crush load are almost the same, while for global bending and SMII deformation mode, the differences between these two forces are significant.

Total energy absorption and crush force efficiency comparison are presented in Figure 8.3. Crush force efficiency of specimen SA4 which had cutting deformation has

been improved by a factor of 2.96 compared to specimen W0 which had global bending deformation. Compared to specimens with geometrical initiator, *CFE* of specimen SA4 has been improved by 56%. Total energy absorption of specimen SA4 is almost the same as that of specimen LG2 and 46.6 % of average total energy absorption of specimens S3-2 and E3-3.

Table 8.1. Experimental cutting test results for displacement up to 100 mm.

Group	Specimens	P_{max} (kN)	P_m (kN)	<i>CFE</i>	$E_{absorbed}$ (kJ)
1	SA1	28.84	24.44	0.85	2.44
	SA2	37.1	28.45	0.77	2.85
	SA3	35.52	28.52	0.80	2.85
	SA4	33.29	27.04	0.81	2.70
	SA5	34.49	27.16	0.79	2.72
2	SB1	34.34	26.38	0.77	2.64
	SB2	34.55	26.65	0.77	2.67
	SB3	25.82	23.69	0.92	2.37
	SB4	33.73	24.93	0.74	2.49
	SB5	33.64	26.06	0.77	2.61
3	LA1	27.93	24.62	0.88	2.46
	LA2	32.47	25.80	0.80	2.58
	LA3	28.78	24.72	0.86	2.47
	LA4	34.9	28.61	0.82	2.86
	LA5	36.01	28.02	0.78	2.80
4	LB1	38.74	28.96	0.75	2.90
	LB2	33.64	26.37	0.78	2.64
	LB3	33.76	27.14	0.80	2.71
	LB4 (no lubrication)	35.87	26.49	0.74	2.65
	LB5 (no lubrication)	35.66	27.10	0.76	2.71
Average		33.45	26.56	0.80	2.66
5	LG2	115.97	26.77	0.23	2.68
6	SG1	124.69	33.21	0.27	3.35

Table 8.2. Representative specimens for the performance measures comparison.

Group identifier	$E_{absorbed}$ (kJ)	P_{max} (kN)	P_m Force(kN)	CFE (%)	Deformation mode
W0	3.35	124.7	33.21	26.6	Global bending
C3	4.36	109.4	43.16	39.5	SMII
S3-2	5.85	111.3	57.92	52.0	SMII
E3-3	5.78	113.7	57.27	50.4	SMII
SA4	2.70	33.29	27.04	0.81	cutting
LG2	2.68	115.97	26.77	23.0	Global bending

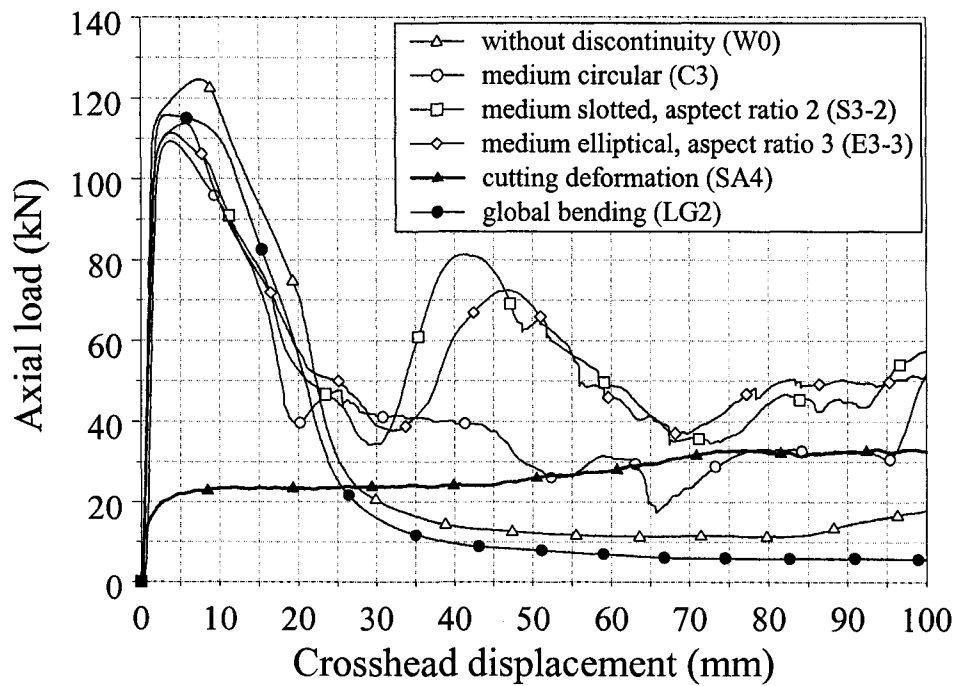


Figure 8.1. Experimentally obtained load/displacement profiles comparison.

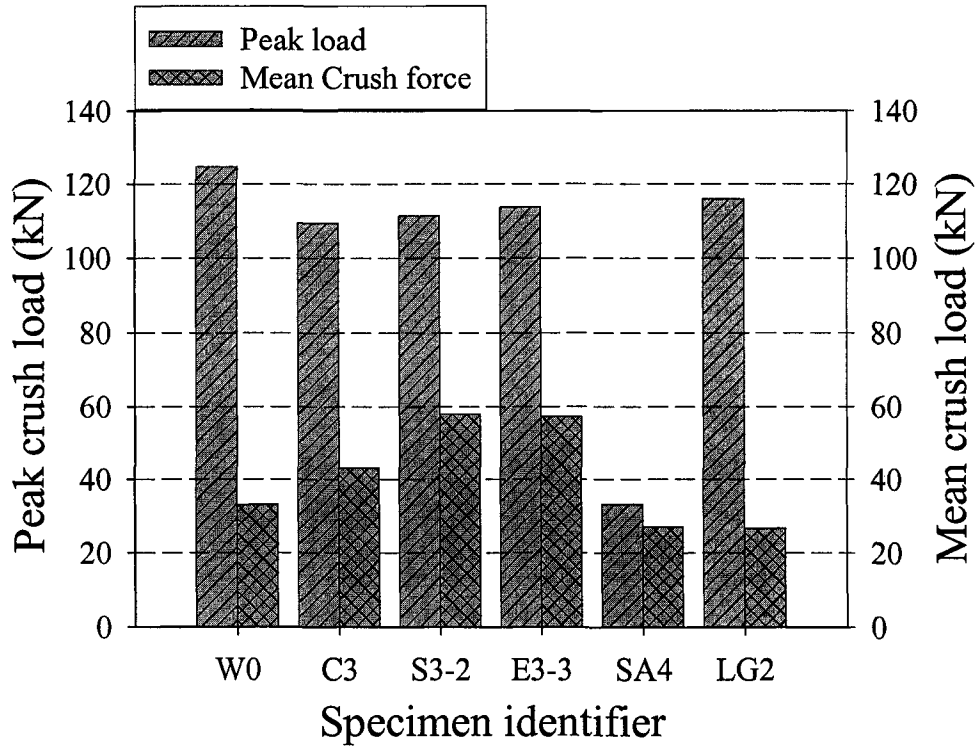


Figure 8.2. Peak crush load and mean crush load comparison.

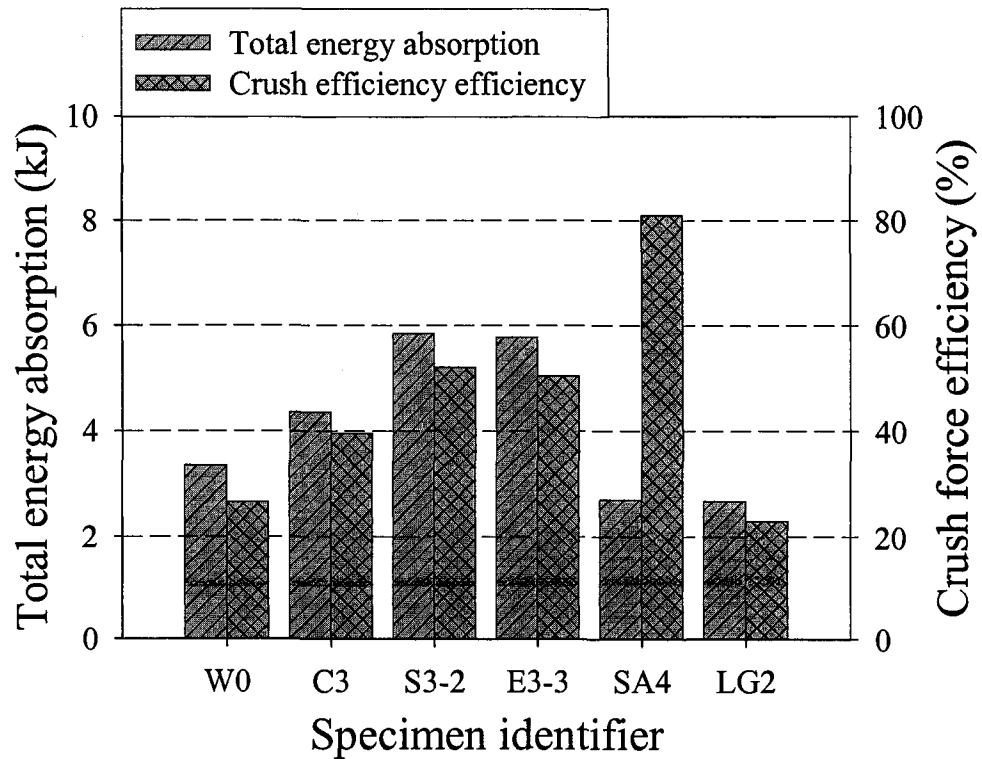


Figure 8.3. Total energy absorption and crush force efficiency comparison.

9. CONCLUSIONS

The theoretical analysis for the energy absorption capacity of aluminum foam filled braided stainless steel tube, the experimental crush testing of AA 6061-T6 extrusions with three different geometrical discontinuities, and the experimental testing of cutting deformation of square cross section aluminum extrusions initiated by a newly designed cutting tool as conducted in this research have provided a significant amount of information regarding the energy absorption abilities of structure members under tensile and compressive loading conditions. The following conclusions can be made based upon the observations and analysis of observed research testing:

9.1 Conclusions for Aluminum Foam Filled Braided Stainless Steel Tube

- 1) The total energy absorption for the tubular structures, with different aluminum foam densities, tested in this investigation, which incorporated tube elongations of approximately 400 mm, ranged from approximately 5.2 kJ to 7.9 kJ.
- 2) It was experimentally observed that significant variations in the force/displacement and energy/displacement behaviour of the foam filled braided tubes occurred in the first and second stages of loading for different aluminum foam densities.
- 3) The experimentally observed response of the braided tube in the third stage of loading illustrated no significant differences for the foam densities considered in this investigation.
- 4) A theoretical model was developed which assumed structural deformation was a result of radial foam crushing and inelastic tensile deformations of the braided tube. Agreement between the predictions of the theoretical model and experimental findings were found to exist with a maximum percentage error of approximately 25%.
- 5) The response of the aluminum foam filled braided tube can be adjusted based upon aluminum foam density and the preload applied to the energy absorbing

structure. This finding allows the structure to be tailored for specific load/displacement requirements.

9.2 Conclusions for Geometrical Imperfections Incorporated Extrusions

- 6) The three different geometrical discontinuities, namely circular, elliptical, and slotted through holes, initiated a splitting and cutting mode of deformation for the square AA6061-T6 extrusions. This mode of deformation resulted in higher values of the *CFE* and the *SEA* while generating a lower value of the maximum crushing force compared to specimens without any geometrical discontinuities. All specimens which did not contain a geometrical discontinuity deformed in a global bending mode.
- 7) Specimen S2-3, which contained a slotted hole discontinuity with a major axis length of 14.29 mm and an aspect ratio of 3, had the highest *CFE* of 0.52. Relative to all specimens without any type of discontinuity, the *CFE* of this specimen increased by 96%.
- 8) Specimen S3-2, which contained a slotted hole discontinuity with a major axis length of 10.72 mm and an aspect ratio of 2, had the highest total energy absorption of 5.85 kJ. Relative to all specimens without any type of discontinuity, the total energy absorption of this specimen increased by 74.6%.
- 9) The influence of aspect ratio was dependent upon major axis length in the crush performance measures of the extrusions. Specimens with major axis lengths of 14.29 mm and 10.72 mm with a large aspect ratio (3) illustrated better total energy absorption and *CFE* measures. However, for specimens with these major axis lengths with aspect ratios less than 2 a notable decrease in the crush performance was observed.
- 10) The aspect ratio and the geometric shape of the discontinuity had no measurable influence on the crush performance parameters for specimens with a major axis length of 7.14 mm.

9.3 Conclusions for Extrusions under Cutting Deformation Mode

- 11) The cutting deformation mode initiated within the extrusions by use of the cutter appeared to be stable and repeatable. A constant force/displacement relationship was observed after a stroke of half the cutter thickness (10 mm) was achieved.
- 12) For the slight variation in blade geometries on side A and side B of the cutter no significant influence on the force/displacement response under axial crushing was observed. In addition, the absence of lubrication fluid had no identifiable influence on the force/displacement behaviour of extrusions subjected to the cutting mode of deformation.
- 13) Tube length appeared to have no significant influence on the force/displacement response of the extrusions which experienced the cutting mode of deformation.
- 14) The average crush force efficiency for extrusions which experienced the cutting mode of deformation was approximately 0.80 independent of tube length. Tube length had a noteworthy influence on the average crush force efficiency for specimens which underwent global bending. In this research programme, the average *CFE* of specimens which experienced a global bending deformation mode was 0.18 and 0.254 for specimens with tube lengths of 200 mm and 300 mm respectively.
- 15) The average energy absorption for extrusions which experienced the cutting mode of deformation was 4.03 kJ. The energy absorption capacity of the 200 mm and 300 mm length specimens, under a cutting deformation mode, was limited due to the stroke restrictions of the compressive testing machine used in this investigation. The average energy absorption for tubular members which experienced global bending was 3.61 kJ and 2.88 kJ for test specimens of length 200 mm and 300 mm respectively.
- 16) For the extrusions which experienced the cutting deformation mode two energy dissipating mechanisms were observed, namely, a cutting deformation mechanism and petalled side wall outward bending mechanism. The bending

energy absorption mechanism appeared to initiate after approximately 50 mm crosshead displacement and accounted for approximately 25% of the total energy absorption.

- 17) Specimen crush force efficiency of cutting deformation mode has been improved by 2.96 times compared to the global bending deformation mode. Compared to the highest *CFE* which can be obtained by incorporating geometrical initiators into specimens as investigated in this research, *CFE* of cutting deformation has been improved by 56%. Total energy absorption of cutting deformation specimen is almost the same as that of specimen LG2 and approximately 46.6 % of average total energy absorption of specimens S3-2 and E3-3 for a displacement of 100 mm.

9.4 Future Work

Future work in this area may include the experimental crush testing of circular tubes with centrally located geometric discontinuities and cutting deformation mode. Furthermore, numerical simulations and theoretical investigations of cutting deformation mode may be helpful in this search.

REFERENCES

- [1]. P.D. Bois, C.C. Chou, B.B. Fileta, T.B. Khalil, A.I. King, H.F. Mahmood, H.J. Mertz, J. Wisnans. Vehicle Crashworthiness and Occupant Protection, Automotive Applications Committee, American Iron and Steel Institute, 2004. Southfield, Michigan.
- [2]. <http://www.worldautosteel.org/>, International Iron and St Institute. Accessed Aug. 2005.
- [3]. <http://www.autoaluminum.org/apps.htm>, Automotive Applications of Aluminum. Accessed Aug. 2005.
- [4]. http://www.hwysafety.org/vehicle_ratings/ce/offset.htm, International Institute of Highway Safety. Accessed Aug. 2005.
- [5]. W. Altenhof, C. Powell, A.M. Harte, R. Gaspar. An experimental investigation into the energy absorption and force/displacement characteristics of aluminum foam filled braided stainless steel tubes under quasi-static tensile loading conditions. *International Journal of Crashworthiness* 2005; 10 (1): 21-31.
- [6]. S.R. Reid. Plastic deformation mechanisms in axially compressed metal tubes used as impact energy absorbers. *International Journal of Mechanical Sciences* 1993; 35 (12): 1035–1052.
- [7]. S.R. Guillow, G. Lu, R.H. Grzebieta. Quasi-static axial compression of thin-walled circular aluminium tubes, *International Journal of Mechanical Sciences* 2001; 43 (9):2103–2123.
- [8]. N. Jones, W. Abramowicz. Static and dynamic axial crushing of circular and square tubes. *Metal Forming and Impact Mechanics*, 1985. Pergamon Press, Oxford, pp. 225-247.
- [9]. W. Abramowicz, N. Jones. Dynamic axial crushing of circular tubes. *International Journal of Impact Engineering* 1984; 2 (3):263–281.
- [10]. W. Abramowicz, N. Jones. Dynamic progressive buckling of circular and square tubes. *International Journal of Impact Engineering* 1986; 4 (4):243–270.
- [11]. M. Langseth and O.S. Hopperstad. Static and dynamic axial crushing of square thin-walled aluminum extrusions. *International Journal of Impact Engineering* 1996; 18 (7-8):949-968.
- [12]. B. Arnold, W. Altenhof. Experimental observations on the crush characteristics of AA6061 T4 and T6 structural square tubes with and without circular discontinuities. *International Journal of Crashworthiness* 2004; 9 (1):73-87.

- [13]. B. Arnold, W. Altenhof. Finite element modeling of the axial crushing of AA6061 T4 and T6 and AA6063 T5 structural square tubes with circular discontinuities. SAE SP-1937 Safety Test Methodology and Structural Crashworthiness, SAE International, 2005. p. 11-26.
- [14]. W. Abramowicz, N. Jones. Transition from initial global bending to progressive buckling of tubes loaded statically and dynamically. *International Journal of Impact Engineering* 1997; 19 (5-6):415-437.
- [15]. F.P.C. Miscow, H.A. Al-Qureshi. Mechanics of static and dynamic inversion processes, *International Journal of Mechanical Science* 1997; 39 (2):147-161.
- [16]. D.K. Leu. The curling characteristics of static inside-out inversion of metal tubes. *International Journal of Machine Tools & Manufacture* 2000; 40 (1):65-80.
- [17]. P.A.R. Rosa, J.M.C. Rodrigues, P.A.F. Martins. External inversion of thin-walled tubes using a die: experimental and theoretical investigation. *International Journal of Machine Tools & Manufacture* 2003; 43 (8):787-796.
- [18]. W.J. Stronge, T.X. Yu, W. Johnson. Long stroke energy dissipation in splitting tubes. *International Journal of Mechanical Sciences* 1983; 25 (9-10):637-47.
- [19]. X. Huang, G. Lu, T.X. Yu. On the axial splitting and curling of circular metal tubes. *International Journal of Mechanical Sciences* 2002; 44 (11):2369-2391.
- [20]. Huang X, Lu G, Yu TX. Energy absorption in splitting square metal tubes. *Thin-Walled Structures* 2002; 40 (2):153-165.
- [21]. G. Lu, L.S. Ong, B. Wang, H.W. Ng. An experimental study on tearing energy in splitting square metal tubes. *International Journal of Mechanical Sciences* 1994; 36 (12):1087-1097.
- [22]. T.X. Yu, D.J. Zhang, Y. Zhang, Q. Zhou. A study of the quasi-static tearing of thin metal sheets. *International Journal of Mechanical Sciences* 1988; 30 (3-4):193-202.
- [23]. H. Fan, B. Wang, G. Lu. On the tearing energy of a ductile thin plate. *International Journal of Mechanical Sciences* 2002; 44 (2):407-421.
- [24]. T.Y. Reddy, S.R. Reid. Axial splitting of circular metal tubes. *International Journal of Mechanical Sciences* 1986; 28 (2):111-31.
- [25]. S.R. Reid, T.Y. Reddy, M.D. Gray. Static and dynamic axial crushing of foam-filled sheet metal tubes. *International Journal of Mechanical Science* 1986; 28 (5):295-322.
- [26]. W. Abramowicz, T. Wierzbicki. Axial crushing of foam-filled columns. *International Journal of Mechanical Science* 1988; 30 (3/4):263-271.

- [27]. T.Y. Reddy, R.J. Wall. Axial compression of foam-filled thin-walled circular tubes. *International Journal of Impact Engineering* 1988; 7 (2):151–166.
- [28]. T.Y. Reddy, S.T.S. Al-Hassani. Axial crushing of wood-filled square metal tubes. *International Journal of Mechanical Science* 1993; 35(3/4):231–246.
- [29]. S.R. Reid. Metal tubes as impact energy absorbers. In: Reid SR, editor. *Metal forming and impact mechanics* 1985. New York, Pergamon Press. pp:249–269.
- [30]. A.G. Hanssen, O.S. Hopperstad, M. Langseth. Design of Aluminium Foam-Filled Crash Boxes with Square and Circular Cross Sections. *International Journal of Crashworthiness* 2001; 6 (2):177-188.
- [31]. A.G. Hanssen, M. Langseth, O.S. Hopperstad. Optimum Design for Energy Absorption of Square Aluminium Columns with Aluminium Foam Filler. *International Journal of Mechanical Sciences* 2001; 43 (1):153-176.
- [32]. A.G. Hanssen, M. Langseth, O.S. Hopperstad. Static Crushing of Square Aluminium Extrusions with Aluminium Foam Filler. *International Journal of Mechanical Sciences* 1999; 41(8):967-993.
- [33]. M. Langseth, O.S. Hopperstad, A.G. Hanssen, Crash Behaviour of Thin-Walled Aluminium Members. *Thin-Walled Structures* 1998; 32 (1-3):127-150.
- [34]. A.M. Harte, N.A. Fleck, M.F. Ashby. Energy absorption of foam-filled circular tubes with braided composite walls. *Eur.J.Mech.A/Solids* 2000; 19 (1): 31-50.
- [35]. B.N. Cox, N. Sridhar, J.B. Davis, X.Y. Gong and F.W. Zok. The energy absorption potential of chain composites. *Acta mater* 2000; 48 (3):755-766.
- [36]. B.N. Cox, J.B. Davis. Knitted composites for energy absorption under tensile loading. *Composites Part A* 2001; 32 (1):91-105.
- [37]. T. Wierzbicki, W. Abramowicz. On the crushing mechanics of thin-walled structures. *Journal of Applied Mechanics* 1983; 50: 727–739.
- [38]. W. Abramowicz, T. Wierzbicki. Axial crushing of multicorner sheet metal columns. *Journal of Applied Mechanics* 1989; 56: 113–120.
- [39]. H.S. Kim. New extruded multi-cell aluminum profile for maximum crash energy absorption and weight efficiency. *Thin-Walled Structures* 2002; 40 (4):311–327.
- [40]. B.P. DiPaolo, P.J.M. Monteiro, R. Gronsky, Quasi-static axial crush response of a thin-wall, stainless steel box component, *International Journal of Solids and Structures* 2004; 41 (14):3707–3733.

- [41]. T.M. Link, J.S. Grimm. Drop Tower Crash Testing of Advanced High Strength Steel Tubes. www.autosteel.org/pdfs/gdis_2005_link.pdf. Accessed Aug. 2005,
- [42]. M. Langseth, A. Hanssen. Lecture Notes on Crashworthiness of Aluminum Structures, Department of Structural Engineering, Norwegian University of Science & Technology, 2002.
- [43]. L. Abah, A. Limam, M. Dejeammes. Effects of cutouts on static and dynamic behaviour of square aluminium extrusions. In: Jones, N., Talaslidis, D.G., Brebbia, C.A., Manolis, G.D. (Eds.), Structures Under Shock and Impact V—SUSI 98. Computational Mechanics Publications, 1998. Southampton, UK, pp. 133–142.
- [44]. N.K. Gupta, S.K. Gupta. Effect of annealing, size and cut-outs on axial collapse behaviour of circular tubes. *International Journal of Mechanical Sciences* 1993; 35 (7):597–613.
- [45]. N.S. Marshall, G.N. Nurick. The effect of induced imperfections on the formation of the first lobe of symmetric progressive buckling of thin-walled square tubes. In: Jones, N., Talaslidis, D.G., Brebbia, C.A., Manolis, G.D. (Eds.), Structures Under Shock and Impact V—SUSI 98. Computational Mechanics Publications, 1998. Southampton UK, pp. 155–168.
- [46]. C.A. Krauss, D.H. Laananen. A parametric study of crush initiators for a thin-walled tube. *International Journal of Vehicle Design* 1994; 15(3/4/5):385-401.
- [47]. S. Lee, C. Hahn, M. Rhee, J. Oh. Effect of triggering on the energy absorption capacity of axially compressed aluminum tubes, *Materials and Design* 1999; 20 (1):31-40.
- [48]. B.I. Bjorneklett, O.R. Myhr. Material Design and Thermally Induced Triggers in Crash Management. SAE 2003-01-2794.
- [49]. G. Chen, X.M. Chen, M.F. Shi, W. Li, T. Tyan. Experimental and Numerical Studies of Crash Trigger Sensitivity in Frontal Impact. SAE Paper, 2005-01-0355.
- [50]. S. Santosa, T. Wierzbicki, A.G. Hanssen, M. Langseth. Experimental and numerical studies of foam- filled sections. *International Journal of Impact Engineering* 2000; 24(5): 509-534.
- [51]. C.L. Magee, P.H. Thornton. Design Consideration in Energy Absorption by Structural Collapse. SAE Paper No. 780434, Feb. 1978.
- [52]. H. F. Mahmood, A. Paluszny. Axial Collapse of Thin Wall Cylindrical Column. Fifth International Conference on Vehicular Structural Mechanics, Detroit, 1984, SAE Paper No. 840727.

- [53]. H.F. Mahmood, A. Paluszny. Design of Thin Wall Columns for Crash Energy Management - Their Strength and Mode of Collapse. SAE Fourth International Conference on Vehicle Structural Mechanics, Nov. 1981, Paper No.811302.
- [54]. H. F. Mahmood, A. Paluszny. Stability of Plate Type Box Columns Under Crush Loading. Computational Methods in Ground Transportation Vehicles, AMD-Vol. 50, pp. 17-33, 1982 Winter Annual Meeting of ASME, Phoenix.
- [55]. J. Hallquist. LS-Dyna keyword user's manual, Livermore Software Technology Corporation, 2001. Livermore, CA.
- [56]. T.B. Khalil, C.M. Ni, H.F. Mahmood, A.I. King(eds). Crashworthiness and Occupant Protection in Transportation Systems, ASME, AMD-Vol. 126/BED-Vol. 19, 1991.
- [57]. J.D. Reid, K.H. Yang(eds). Crashworthiness and Occupant Protection in Transportation System, ASME, AMD-Vol. 169/BED-Vol. 25, 1993.
- [58]. M. Langseth, O. Hopperstad, T. Berstad. Crashworthiness of aluminum extrusions: validation of numerical simulation, effect of mass ratio and impact velocity, International Journal of Impact Engineering 1999; 22 (9-10):829-854.
- [59]. T. Berstad, O. Hopperstad, M. Langseth. Elasto-viscoplastic constitutive models in the explicit finite element code LS-DYNA3D, Second International LS-DYNA3D Conference, 1994. Paper Number 2ILSD3D113.
- [60]. K. Yamazaki, J. Han. Maximization of the crushing energy absorption of tubes, Structural Optimization 1998; 16 (1):37-46.
- [61]. J. Han, K. Yamazaki. A study on maximization of dynamic crushing energy absorption of square tubes with and without stiffener. Japan Society of Mechanical Engineering 2000; 43 (2):138-145.
- [62]. P.A. Schweitzer. Metallic Materials – Physical, Mechanical, and Corrosion Properties. Marcel Dekker Inc. 2003:131-138.
- [63]. Annual Book of ASTM Standards. ASTM International, Section 3, Vol. 3.01, Standard E8M, 2002. p. 60-81.
- [64]. N. Jones, Structural Impact, Cambridge, Cambridge University Press, 1989.
- [65]. Machinery's hand book, Industrial Press Inc., 2000, 26th edition.

APPENDIX A

Experimental Testing Results of Tensile Testing of Empty Braided Stainless Steel Tubes and Tensile Tests of Aluminum Foam Filled Braided Tubes

A.1. Tensile Testing of Empty Braided Stainless Steel Tubes

Figure A.1 illustrates the experimentally observed force versus crosshead displacement relationship for both the 185 mm and 330 mm length empty braided stainless steel tubes. A comparison of the force/displacement response of the two different length tubes indicated that in the first 15 mm of crosshead displacement the force/displacement responses were similar. Although different force/displacement relationships in the first 15 mm of crosshead displacement may have been expected, it is hypothesized that the collection of wires to form the braided tube, which deviates from a solid tubular structure, and the kinematic behaviour of the tows during elongation (scissoring) of the braided tubes outweighed the role of tube length on the influence of structure stiffness.

After the first 15 mm of crosshead displacement, the force/displacement relationships for the braided tubes with different lengths vary significantly. The deformation phenomena satisfied the inverse relationship between structure length and stiffness; the longer braided tube illustrated a lower load capacity than the shorter tube for a given crosshead displacement beyond 15 mm.

For the braided tube with length of 185 mm failure was observed to occur at a load of approximately 51.9 kN. Failure, which is defined as the point when the tube can no longer support any increase in applied load, did not occur catastrophically, rather a progressive failure of the individual strands of the tows was observed. Ultimate failure of the tube, which is defined as the point when the tube can not longer support any applied load, occurred after an additional crosshead displacement of approximately 28 mm. The experimentally observed load at failure for the shorter tube agreed well with a calculated failure force of 46 kN based on the tensile strength of the AISI 304 stainless steel material and the tube geometry. The total elongation of the 185 mm braided tube was observed to be approximately 55%.

The braided tube of length 330 mm did not experience ultimate failure for the crosshead displacements considered in this research. A failure load for the 330 mm length tube was observed to be 52.4 kN; similar to the braided tube of length 185 mm. The failure load for the 330 mm tube was reached at approximately 124 mm of crosshead displacement after which the load carry capacity of the tube decreased.

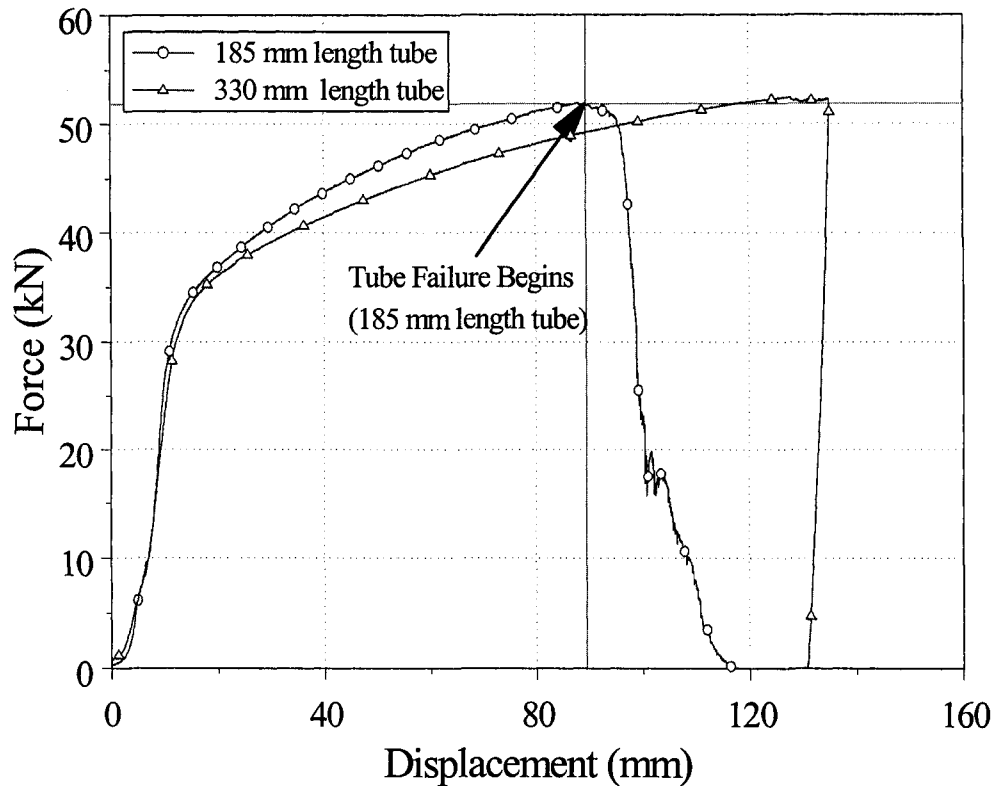


Figure A.1. Force versus displacement characteristics for the empty braided tubes of 185 mm and 330 mm lengths.

A.2. Tensile Tests of Aluminum Foam Filled Braided Tubes

Load versus displacement results for the tensile testing of the aluminum foam filled braided tubes are presented in Figure A.2 through Figure A.5 for aluminum foam densities considered in this research. As previously indicated in the testing procedure, the tensile tests were completed in three stages of loading due to the stroke limitation of the testing machine. For each specimen, plots of force versus displacement for all three loading stages were juxtaposed to illustrate the structural response of the tube for

crosshead displacements up to approximately 400 mm. In addition, energy versus displacement curves were also plotted with the corresponding load versus displacement curve for each specimen. The energy absorbed by the tube was equated to the work done by the crosshead, which was obtained through integration of the force/displacement relationship, as indicated in equation (A.1).

$$(A.1)$$

$E = \int F_z \cdot dz$ At the beginning of the second and third stages of loading, it was assumed that the energy absorbed by the tube included the energy absorbed in the previous loading stage.

From examination of Figure A.2 through Figure A.5, it can be observed that during the first stage of loading the tensile force fluctuated about a constant value. In this stage, the structure deformation was due to crushing and fracture of the aluminum foam core. The scissoring of the tube tows pulverized the foam edges and a small number of protruding portions of the aluminum foam core which were trapped between the tows. Local tensile fracture within the foam core caused the loading profile to have an oscillatory response. During the first stage of loading, load/displacement results were found to be dependent upon foam core density.

An examination of the mechanical behaviour of the aluminum foam core has been completed and the stress/strain response for foam densities ranging from 200 kg/m³ to 400 kg/m³ is illustrated in Figure A.6. Compressive testing was completed on a 100 kN servo hydraulic compression testing machine on foam cubes with dimensions of 66 mm by 66 mm by 66 mm. The nominal speed of the actuator was 2.5 mm/min. Observations from the experimental tests, as shown in Figure A.6, illustrated that the plateau stress of the foam is strongly dependent upon the foam density. The majority of foam crushing (for engineering strains ranging from 1% to 60%) occurred at the constant plateau stress. Results from the first stage of loading in Figure A.2 through Figure A.5 and the dependence of plateau stress of foam density, as presented in Figure A.6, clearly illustrate and verify that a direct relationship between foam density and tensile load in the first stage of loading exists.

In the second stage of loading, the deformation was a combination of radial crushing of the inner foam core and axial deformation of the braided tube. As the crosshead displacement occurred, the angle between the braided tube tows decreased and eventually reached a lockup condition. After tow lockup occurred the radial displacements of the braided tube decreased significantly, and hence the foam core no longer experienced crushing in the radial direction. The majority of deformation, following lockup, occurred within the braided tube in the axial direction.

Further tensile loading, subsequent to the second stage, resulted in plastic deformation of the braided tube with little or no observed deformation occurring within the foam core. The load/displacement relationship in the third stage of loading was very comparable to the load/displacement behaviour of an unfilled braided tube. This finding indicates that the mechanical behaviour of the foam filled braided tube is independent of foam core density during the third stage of loading.

The energy absorbed in each stage of loading for the four tensile specimens is summarized in table A.1. Foam core density is responsible for energy absorption in the first and second stages of loading with a dependence of tube mechanical behaviour also occurring in the second stage. A tailored application of these devices for energy absorption is possible with the selection of the appropriate foam density according to specified force/displacement requirements.

Table A.1. Energy absorption of the foam filled braided tubes.

Specimen #	$E_{stage 1}$ (kJ)	$E_{stage 2}$ (kJ)	$E_{stage 3}$ (kJ)	E_{total} (kJ)
1	0.279	0.673	4.221	5.172
2	0.340	1.510	3.908	5.759
3	0.428	1.888	4.135	6.451
4	0.666	2.137	5.130	7.933

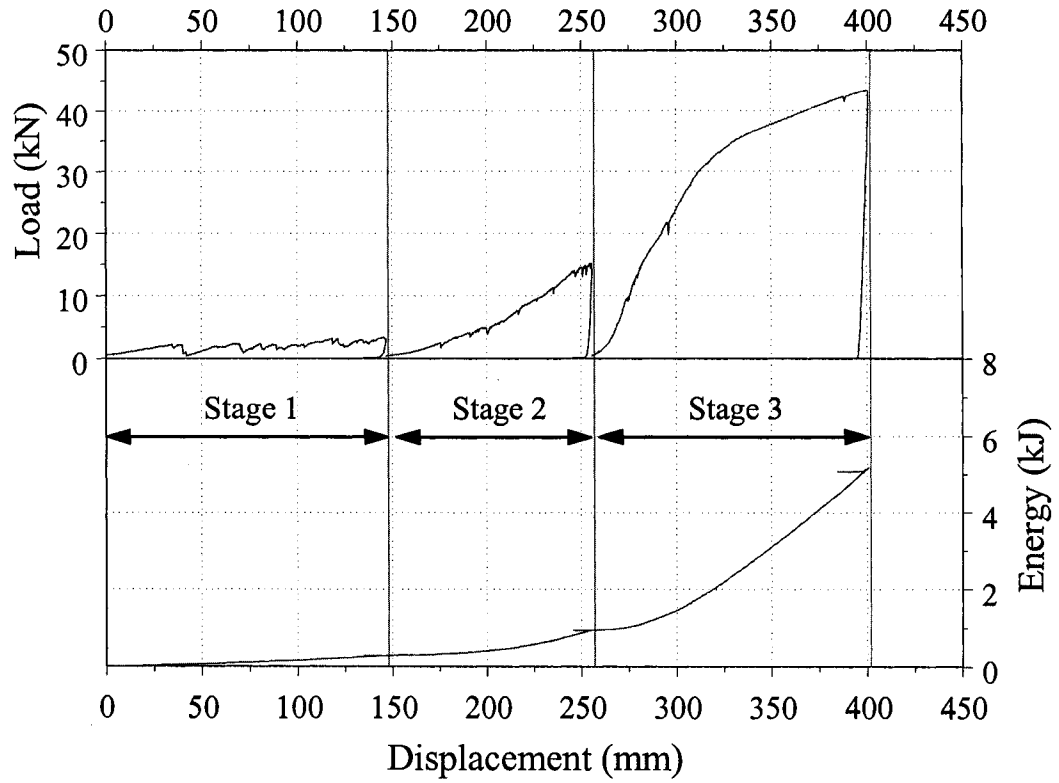


Figure A.2. Force/displacement and energy/displacement curves of the foam filled braided tube for specimen 1 with $\rho_f = 248.2 \text{ kg/m}^3$.

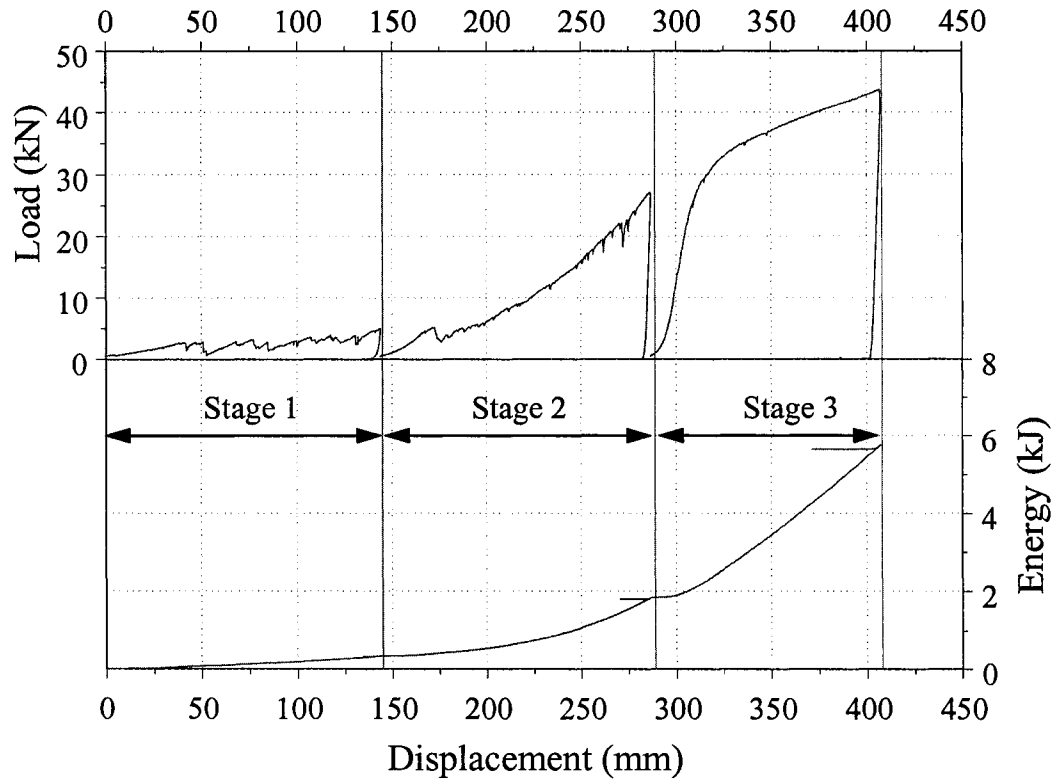


Figure A.3. Force/displacement and energy/displacement curves of the foam filled braided tube for specimen 3 with $\rho_f = 288.2 \text{ kg/m}^3$.

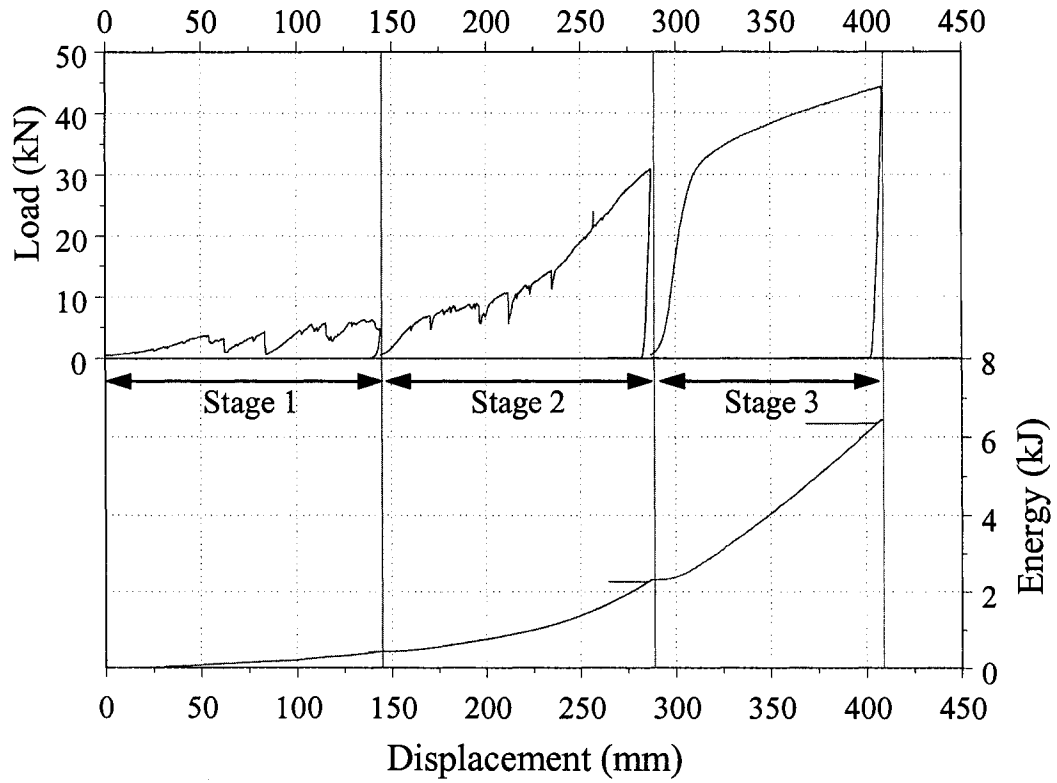


Figure A.4. Force/displacement and energy/displacement curves of the foam filled braided tube for specimen 4 with $\rho_f = 298.2 \text{ kg/m}^3$.

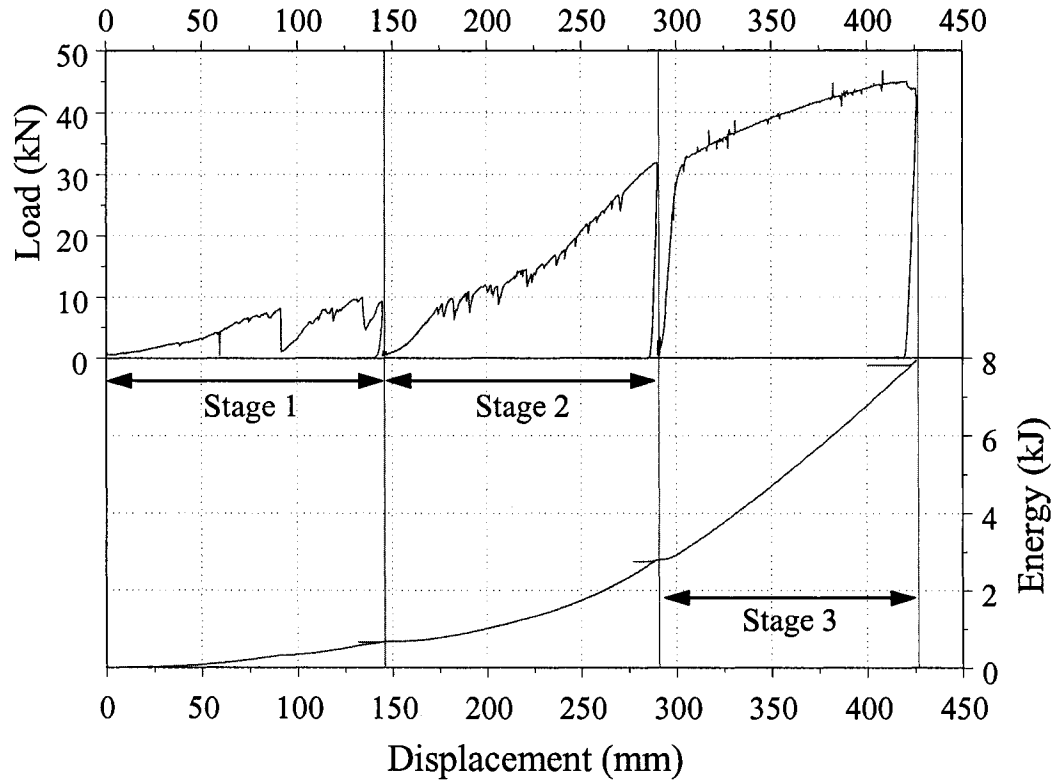


Figure A.5. Force/displacement and energy/displacement curves of the foam filled braided tube for specimen 5 with $\rho_f = 373.4 \text{ kg/m}^3$.

APPENDIX B

Copyright Permission

B.1 Copyright Permission from Elsevier

Dear Mr. Cheng,

We hereby grant you permission to reproduce the material detailed below in your thesis at no charge subject to the following conditions:

1. If any part of the material to be used (for example, figures) has appeared in our publication with credit or acknowledgement to another source, permission must also be sought from that source. If such permission is not obtained then that material may not be included in your publication/copies.

2. Suitable acknowledgment to the source must be made, either as a footnote or in a reference list at the end of your publication, as follows:

"Reprinted from Publication title, Vol number, Author(s), Title of article, Pages No., Copyright (Year), with permission from Elsevier".

3. Reproduction of this material is confined to the purpose for which permission is hereby given.

4. This permission is granted for non-exclusive world English rights only. For other languages please reapply separately for each one required. Permission excludes use in an electronic form. Should you have a specific electronic project in mind please reapply for permission.

5. This includes permission for the National Library of Canada to supply single copies, on demand, of the complete thesis. Should your thesis be published commercially, please reapply for permission.

Yours sincerely,
<<...OLE_Obj...>>
Natalie David
Rights Assistant

From: Cheng Q [mailto:cheng1t@uwindsor.ca <mailto:cheng1t@uwindsor.ca>]
Sent: 11 October 2005 19:33
To: permissions@elsevier.com

Subject: copyright permission request

Dear Mrs. Gainford,

I have been writing my thesis for my Master of Applied Science degree in Mechanical Engineering at the University of Windsor, Ontario, Canada. Within the Literature Review chapter of my thesis I would like to use the following attached figures published by your company to illustrate research and/or experimental testing done by other researchers in my research area. I am requesting your permission to use these figures in my literature review part. My thesis would be printed in 5 copies. Two copies would be deposited in the University of Windsor Library. One copy would be deposited in the Mechanical Engineering Department. The other two copies would be given to individuals. Would you please respond to this as soon as possible?

Thank you very much!

Best regards,

Qingwu Cheng

Figures:

- (1) Figure 1, Figure 2, and Figure 3 from: Reid, S.R., Plastic deformation mechanisms in axially compressed metal tubes used as impact energy absorbers. *International Journal of Mechanical Sciences* 1993; 35 (12): 1035-1052.
- (2) Figure 1 and Figure 2 from: S.R. Guillow, G. Lua, R.H. Grzebieta, Quasi-static axial compression of thin-walled circular aluminium tubes, *International Journal of Mechanical Sciences* 2001; 43 (9):2103-2123.
- (3) Figure 1 from: M. Langseth and O.S. Hopperstad. Static and dynamic axial crushing of square thin-walled aluminum extrusions. *International Journal of Impact Engineering* 1996; 18 (7-8):949-968.
- (4) Figure 1 from: Daw-Kwei Leu, The curling characteristics of static inside-out inversion of metal tubes. *International Journal of Machine Tools & Manufacture* 2000; 40 (1):65-80.
- (5) Figure 2 and Figure 3 from: F.P.C. Miscow, H.A. Al-Qureshi, Mechanics of static and dynamic inversion processes, *Int. J. Mech. Sci.* 1997; 39 (2):147-161.
- (6) Figure 1, Figure 3, Figure 4, Figure 5, and Figure 6 from: X. Huang, G. Lu, T.X. Yub, On the axial splitting and curling of circular metal tubes. *International Journal of Mechanical Sciences* 2002; 44 (11):2369-2391.

- (7) Figure 2 and Figure 3 from: Huang X, Lu G, Yu TX. Energy absorption in splitting square metal tubes. *Thin-Walled Structures* 2002; 40 (2):153-165.
- (8) Figure 3 and Figure 7 from: Anne-Marie Harte, Norman A. Fleck, Michael, F. Ashby. Energy absorption of foam-filled circular tubes with braided composite walls. *Eur.J.Mech.A/Solids* 2000; 19 (1): 31-50.
- (9) Figure 1 and Figure 6 from: B.N.Cox, N. Sridhar, J.B. Davis, X! .- Y. Gong and F.W. Zok. The energy absorption potential of chain composites. *Acta mater* 2000; 48 (3):755-766.
- (10) Figure 7, Figure 8 and Figure 9 from: Heung-Soo Kim. New extruded multi-cell aluminum profile for maximum crash energy absorption and weight efficiency. *Thin-Walled Structures* 2002; 40 (4):311-327.
- (11) Figure 1 and Figure 2 from: B.P. DiPaolo, P.J.M. Monteiro, R. Gronsky, Quasi-static axial crush response of a thin-wall, stainless steel box component, *International Journal of Solids and Structures* 2004; 41(14):3707-3733.
- (12) Figure 8 and Figure 18 from: W. Abramowicz and N. Jones. Transition from initial global bending to progressive buckling of tubes loaded statically and dynamically. *International Journal of Impact Engineering* 1997; 19 (5-6):415-437.
- (13) Figure 2 from: M. Langseth, O. Hopperstad, and T. Berstad. Crashworthiness of aluminum extrusions: validation of numerical simulation, effect of mass ratio and impact velocity, *International Journal of Impact Engineering* 1999; 22 (9-10):829-854.

B.2 Copyright Permission from Woodhead Publishing

Dear Qingwu Cheng

Thank you for your email.

We are happy for you to use the figures listed below as long as we are acknowledged in the book, as the source.

If this is going to cause any problems please let me know before you proceed.

Yours
Julie Pleasance
Rights/Permissions Department

Woodhead Publishing Limited
Abington Hall, Abington
Cambridge, CB1 6AH, UK.

Tel: +44(0)1223 891358 Ext. 39
Fax: +44(0)1223 893694
Email: juliep@woodhead-publishing.com
Website: www.woodheadpublishing.com

Registered office, as above, No. 2395953
VAT Reg. No. GB 538-2109-53

Original Message processed by Tobit InfoCenter
Subject: Fw-2: Seeking copyright permission (12-Oct-2005 18:41)
From: martinw@woodhead-publishing.com
To: juliep@woodhead-publishing.com

Original Message processed by Tobit InfoCenter
Subject: Fw: Seeking copyright permission (11-Oct-2005 15:40)
From: ben@woodhead-publishing.com
To: martinw@woodhead-publishing.com

Original Message processed by Tobit InfoCenter
Subject: Seeking copyright permission (11-Oct-2005 15:36)
From: cheng1t@uwindsor.ca
To: custserv@woodhead-publishing.com

Dear Sir or Madam,

I have been writing my thesis for my Master of Applied Science degree in Mechanical Engineering at the University of Windsor. Within the Literature Review chapter of my thesis I would like to use the following attached figures published by your company to illustrate research and/or experimental testing done by other researches in my research area. I am requesting your permission to reprint these figures in my literature review part. Would you please respond to this as soon as possible?

Thank you very much!

Best regards,

Qingwu Cheng

Figures:

(1). Figure 5, Figure7, Figure! 8.2, Figure 13.2, Figure 14.2, and Figure 16 from: Arnold B, Altenhof W. Experimental observation on the crush characteristics of AA6061 T4 and T6 structural square tubes with and without circular discontinuities. IJCrash 2004, Vol.9, No. 1 pp.73-87.

(2) Figure 5 from: Altenhof W, Powell C, Harte AM, Gaspar R. An experimental investigation into theenergy absorption and force/displacement characteristics of aluminum foam filled braided stainless stell tubes under quasi-static tensile loading conditions. IJCrash 2005, Vol. 10, No. 1, pp. 21-31.

(3) Two Figures (please see attached Word file) from: Hassen, A.G., O.S. Hopperstad and M. Langseth. Design! of Aluminium Foam-Filled Crash Boxes with Square and Circular Cross Section. IJCrash 2001, 6(2), pp. 177-188.

B.3 Copyright Permission from SAE

Dear Mr. Chen:

Permission to include the figures (noted below) in a thesis for your Master of Applied Science degree in Mechanical Engineering at the University of Windsor, Ontario, Canada, is hereby granted, and we request that the following credit statement appear directly below each figure:

"Reprinted with permission from SAE paper number _____ * (c) 200_** Society of Automotive Engineers, Inc."

(*please insert the appropriate paper number and **year of publication)

I understand that you will produce 5 printed copies of your thesis for distribution to the university library, your supervisor and for yourself.

Thank you for contacting SAE for this permission.

Sincerely,
Terri Kelly
SAE Publishing

From: Cheng Q [mailto:cheng1t@uwindsor.ca]
Sent: Tuesday, October 11, 2005 12:49 PM
To: copyright
Subject: copyright permission request

Dear Sir or Madam,

I have been writing my thesis for my Master of Applied Science degree in Mechanical Engineering at the University of Windsor, Ontario, Canada. Within the Literature Review chapter of my thesis I would like to use the following figures published by SAE to illustrate research and/or experimental testing done by other researches in my research area. I am requesting your permission to use these figures in my literature review part. Would you please respond to this as soon as possible?

Thank you very much!

Best regards,

Qingwu Cheng

Figures:

- (1) Figure 5, Figure 6, and Figure 7 from: Borge Iver Bjorneklett, Ole Runar Myhr. Material Design and Thermally Induced Triggers in Crash Management. SAE 2003-01-2794.
- (2) Figure 3, Figure 4, Figure 5, and Figure 10 from: Guofei Chen, Xiao Ming Chen and Ming F. Shi, Wayne Li and Tau Tyan. Experimental and Numerical Studies of Crash Trigger Sensitivity in Frontal Impact. SAE Paper, 2005-01-0355.
- (3) Figure 3, Figure 18, and Figure 20 from: Arnold B, Altenhof W. Finite element modeling of the axial crushing of AA6061 T4 and T6 and AA6063 T5 structural square tubes with circular discontinuities. SAE SP?1937 Safety Test Methodology and Structural Crashworthiness, SAE International, 2005-01-0703.

B.4 Copyright Permission from IIHS

Dear Qingwu Cheng,

Thank you for your email. The Institute is pleased to give you permission to use the image you downloaded from our website in your thesis. We requested that you list the Institute as the source of the image.

Stephen Oesch

From: Cheng Q [mailto:cheng1t@uwindsor.ca]
Sent: Friday, October 07, 2005 2:55 PM
To: Steve Oesch
Subject: request for copyright permission

Dear Mr. Oesch,

I have been writing my thesis for my Master of Applied Science degree in Mechanical Engineering at the University of Windsor. Within the Literature Review chapter of my thesis I would like to use the attached image downloaded from your website (<http://www.hwysafety.org/ratings/rating.aspx?id=5>) to illustrate research and/or experimental testing done by other researchers/organizations in my research area. I am requesting your permission to use this image in my literature review part to show the effect of good structural design on improving vehicle crashworthiness. Would you please respond to this as soon as possible?

Thank you very much!

Best regards,

Qingwu Cheng

VITA AUCTORIS

Qingwu Cheng was born in 1970 in Wuhan, China. He graduated from the University of Science and Technology, Beijing where he obtained a B.A.Sc. in Mechanical Engineering in 1991. He is currently a candidate for the M.A.Sc. degree in Mechanical Engineering at the University of Windsor and hopes to graduate in Fall 2005.